Production and Characterisation of Alumina-Copper Interpenetrating Composites

Herstellung und Charakterisierung von Aluminiumoxid-Kupfer interpenetrierenden Verbundwerkstoffen

Zur Erlangung des akademischen Grades Doktor-Ingenieur (Dr.-Ing.)
genehmigte Dissertation von **Jami Susan Winzer**, M.Sc. aus Sydney, Australien
September 2011 — Darmstadt — D 17

TECHNISCHE UNIVERSITÄT DARMSTADT

Material- und Geowissenschaften
Nichtmetallisch-Anorganische Werkstoffe

édition scientifique
VVB LAUFERSWEILER VERLAG

1. Auflage 2011

1st Edition 2011

Printed in Germany

édition scientifique
VVB LAUFERSWEILER VERLAG

STAUFENBERGRING 15, D-35396 GIESSEN
Tel: 0641-5599888 Fax: 0641-5599890
email: redaktion@doktorverlag.de

www.doktorverlag.de

Production and Characterisation of Alumina-Copper Interpenetrating Composites

Herstellung und Charakterisierung von Aluminiumoxid-Kupfer interpenetrierenden Verbundwerkstoffen

Zur Erlangung des akademischen Grades Doktor-Ingenieur (Dr.-Ing.)
genehmigte Dissertation von Jami Susan Winzer, M.Sc. aus Sydney, Australien
September 2011 — Darmstadt — D 17

TECHNISCHE UNIVERSITÄT DARMSTADT

Material- und Geowissenschaften
Nichtmetallisch-Anorganische Werkstoffe

Production and Characterisation of Alumina-Copper Interpenetrating Composites
Herstellung und Charakterisierung von Aluminiumoxid-Kupfer interpenetrierenden Verbundwerkstoffen

Genehmigte Dissertation von Jami Susan Winzer, M.Sc. aus Sydney, Australien

1. Gutachten: Prof. Jürgen Rödel
2. Gutachten: Prof. Clemens Müller

Tag der Einreichung: 2nd September 2011
Tag der Prüfung: 29th September 2011

Darmstadt — D 17

Acknowledgements

I wish to thank Prof. Jürgen Rödel who supported my work within his research group. He allowed much freedom in the direction of my work and enabled me to visit conferences, summer schools and other research institutes around the globe. He showed considerable flexibility and understanding with my need to balance the demands of being a mother with completing my thesis. His intensive supervision at the start and transition to a more distanced approach at the end taught me to work independently. I am grateful that I was able to complete my PhD in his group.

Ludwig Weiler was my direct supervisor and offered much support up until his retirement. I profited greatly from his wide experience in industry, the production of ceramics and composites and various characterisation techniques.

Emil Aulbach, Herbert Hebermehl, Michael Heyser and Michael Weber always managed to find great solutions for whatever technical problems I had. Thanks to Gundel Fliß for the many computer solutions and helping me set up a home office. Thanks to Roswita Geier and Gila Völzke for always managing to find a quick solution to any administrative issues.

I had a lot of help from my student assistants Peter Bleith, Yining Zhang and Hans Wardenga, both in sample preparation and characterisation. Without them I would not have achieved as much as I did.

Thanks to Kyle Webber and Klaus Seifert for correcting drafts of this thesis. Klaus read a number of sections multiple times, and that in a very short time while I was approaching the deadline. He also helped a lot with my defense presentation and spurred me on to get finished on time. I benefited greatly from his extensive IT knowledge over the years that we worked together, and even after he had finished his PhD. His friendship is greatly appreciated.

The whole NAW group was a pleasure to be a part of, and I particularly enjoyed the times we spend together with activities outside of work: barbecues, parties, bowling, rowing and skiing, just to mention a few.

Rod Martin at MERL in Hitchin, UK, kindly enabled wear testing to be conducted and assisted in the interpretation of the results obtained. Jeanne Pouquet taught me how to use the wear testing equipment and helped make my stay in Hitchin a pleasant one.

Prof. Jan Dusza at IMR-SAS in Kosice, Slovakia, facilitated the measurements of hardness, bending strength and fractograpic analysis. Alexandra Kovalcikova not only showed me how to use the experimental equipment, she also showed great hospitality and took me on many outings. The whole group was very welcoming and included me to many social events. In particular, I wish to thank Kveta and Tina Markus for kindly inviting me into their home and sharing many a culinary delight. They took me on numerous excursions around their fascinating country, ensuring there was never a dull moment during my stay.

Prof. Mark Hoffman from UNSW in Sydney, Australia kindly put me in contact with Prof. Rödel. Without this I would have missed out on the great experiences of the last five years. He encouraged the the publication of the wear results, provided helpful insights into wear mechanisms and gave constructive criticism of early drafts of the wear paper. On his visits to Darmstadt we also had helpful discussions about my experimental work.

Many thanks to Victor Salit and Prof. Dietmar Gross for the FEM modelling of Young's modulus based on X-Ray CT measurements. Victor also offered many insights into how he conducted the numerical modelling, as well as into various theoretical models.

My family was a huge support to me during this time, particularly in the last six months. My mother-in-law, Judith Winzer, took great care of my son Jonathan on the many weekends when I needed to write. During the week Jonathan was in good hands with Fatima Sarwar. After David's birth my sister Danica Walsh, was there for eight weeks to help out with the boys and managing the household while I made the last corrections to this thesis and prepared for my exam. I am very grateful for her help. Thanks to my parents and grandparents for the support and encouragement. My husband Andreas always encouraged me to keep at it, do my best and get my thesis finished.

Last but certainly not least: thanks be to God, creator of all things, without whom no-one would exist and nothing could be known.

Jami Winzer

Darmstadt, August 2011

Contents

1 Introduction **6**

2 Literature Review **8**

2.1 Production of ceramic-metal composites 8

2.1.1 The porous ceramic preform 8

2.1.2 Metal infiltration 13

2.1.3 Ceramic-metal interface wetting 15

2.1.4 Residual stress, cavitation and microcracking 17

2.2 Properties of ceramic-metal composites 19

2.2.1 Young's modulus 19

2.2.2 Fracture toughness 21

2.2.3 Thermal expansion and conductivity 28

2.2.4 Friction and wear 33

3 Production **35**

3.1 Selection and characterisation of materials 35

3.2 Porous alumina preforms 38

3.3 Copper infiltration 41

3.4 Processing issues and optimisation 43

3.5 Sample nomenclature 46

4 Characterisation **47**

4.1 Microstructure and composition 47

4.1.1 Porous alumina preforms 47

4.1.2 Composites 48

4.2 Mechanical properties 50

4.2.1 Young's modulus 50

4.2.2 Hardness 51

4.2.3 Bending strength and fractography 51

4.2.4 Fracture toughness 52

4.3 Thermal properties 56

4.3.1 Thermal expansion 56

4.3.2 Thermal conductivity 56

4.4 Wear behaviour 58

5 Results **59**
5.1 Microstructure and composition 59
5.1.1 Porous alumina preforms 59
5.1.2 Composites 61
5.2 Mechanical properties 63
5.2.1 Young's modulus 63
5.2.2 Hardness 64
5.2.3 Bending strength and fractography 65
5.2.4 Fracture toughness 70
5.2.5 Crack opening displacement 76
5.3 Thermal properties 78
5.3.1 Thermal expansion behaviour 78
5.3.2 Thermal conductivity 85
5.4 Wear behaviour 87

6 Discussion **95**
6.1 Microstructure and composition 95
6.1.1 Porous alumina preforms 95
6.1.2 Composites 96
6.2 Mechanical properties 97
6.2.1 Young's modulus 97
6.2.2 Hardness 100
6.2.3 Fractography and bending strength 101
6.2.4 Fracture toughness 105
6.2.5 Crack opening displacement 108
6.3 Thermal properties 113
6.3.1 Thermal expansion behaviour 113
6.3.2 Thermal conductivity 120
6.4 Wear behaviour 121

7 Conclusions **124**

Bibliography **135**

Curriculum Vitae **136**

1 Introduction

Ceramic-metal composites are an exciting field of research, enabling a combination of properties not possible in monolithic metals or ceramics. Alumina-copper composites enable the high thermal and electrical conductivity and the high toughness of copper to be combined with the high stiffness, hardness and wear resistance of alumina [1]. This combination of properties possible makes alumina-copper composites particularly interesting for wear applications. Examples include automobile brakes and the cylinder bores and bearings of internal combustion engines. Currently, grey cast iron (GCI) is the only car brake material in widespread use, with other alternatives such as Silicon Carbide (SiC) fibre reinforced SiC prohibitively expensive. The disadvantages of GCI include low hardness and high density. Alumina would provide a higher wear resistance due to the higher hardness. Copper would provide the toughness necessary to prevent sudden catastrophic failure typical to monolithic ceramics, with the high thermal conductivity drawing frictional heat away from the wear surface to prevent thermal shock and severe wear. Alumina-copper composite brake disks could potentially have a longer lifetime and also be lighter than GCI, an important feature for reducing fuel consumption.

There are three broad types of ceramic-metal composites. Metal Matrix Composites (MMC) have a continuous metal network, Ceramic Matrix Composites (CMC) have a continuous ceramic network and in InterPenetrating Network (IPN) composites, both components are continuous. Although more difficult to produce, the advantages of IPN composites include a higher Young's modulus, hardness and load bearing capacity than MMCs, as well as a higher thermal conductivity and higher fracture toughness than CMCs. During production, large residual stresses build up in the composite due to the difference in thermal expansion coefficient of the two phases [2, 3]. Scientifically this is an interesting aspect of ceramic-metal composites, since it significantly affects the mechanical properties and thermal expansion behaviour. Until now relatively few studies have been published on alumina-copper IPN composites [3–7]. This work contributes towards filling this gap in the literature.

A similar system which has already received some attention is alumina-aluminium composites. One drawback is the relatively low melting point of aluminium (660 °C) limiting the possible temperatures of application. Since copper has a higher melting point (1083 °C), alumina-copper composites have the potential for applications in a wider temperature range. Copper also has a higher thermal conductivity than aluminium

(401 W/mK compared with 236 W/mK at 0 °C [8]). This would allow heat generated at a wear surface to be more rapidly dispersed, thus reducing the likelihood of thermal shock.

The aim of this project was to produce and characterise copper-alumina interpenetrating composites, in particular, the effect of microstructure on the properties. The range of copper content was 15 to 55 % and the range in copper ligament diameter 1 to 30 μm. The composite was produced by first making porous alumina preforms with a range of porosities and pore sizes, then infiltrating with copper. The effects of copper ligament diameter and copper content on the mechanical and thermal properties as well as wear behaviour were investigated. Since the wear behaviour is strongly influenced not only by the mechanical but also the thermal properties, it was important to investigate both of these areas. Although wear testing is usually conducted much closer to the application stage, initial trials were conducted in order to determine the most promising composition and microstructure combination.

2 Literature Review

2.1 Production of ceramic-metal composites

There are three types of ceramic-metal composites. Metal Matrix Composites (MMC) have a continuous metal network, typically with $V_{metal} > V_{ceramic}$. Ceramic Matrix Composites (CMC) have a continuous ceramic network, usually with $V_{ceramic} > V_{metal}$, although there are exceptions. In interpenetrating network(IPN) composites both components are continuous. The only limitation on composition is that there is enough of each phase for both to percolate. Depending on the form, for the minority phase this is around 20 to 30 %, less for fibres and more for particles. The advantages of an IPN include a higher Young's modulus, hardness and load bearing capacity than MMCs, as well as a higher thermal conductivity and higher fracture toughness than CMCs. In the naming of such composites, either the matrix phase for MMCs and CMCs or the majority phase in IPN is mentioned first.

2.1.1 The porous ceramic preform

To produce an IPN ceramic-metal composite, the first step is to produce a macroporous ceramic preform. Macroporous is defined by IUPAC recommendations as exhibiting a pore width/diameter > 50 nm [9]. There is a variety of methods for producing open porous ceramics described in the literature, ranging from patents in 1963 [10] to current reviews [11, 12], allowing the tailoring of the microstructure. The porosity and pore sizes reported vary between 20 and 97 % and 400 nm to 4 mm, respectively [11]. The different methods available have been summarized in figure 2.1. These methods can be grouped into four categories: i) partially sintered, ii) sacrificial template, iii) replica and iv) foaming and setting. The ranges of porosities and grain sizes reported for each category are shown in figure 2.1. Each of the four categories are described briefly below and shown schematically in figure 2. For this project, ceramics with pore sizes from 1 to 30 μm and open porosities of 20 to 60 % are required. For this reason the first two categories will be considered in more detail later. A recent review by Studart et al. [11] provides a comprehensive summary of these methods. Many references for each particular method are also included in this review.

i) Partially sintered: Partial sintering involves either dry pressing or slip casting and drying and then firing. Porosities up to 40 % are achievable [15]. The pores are

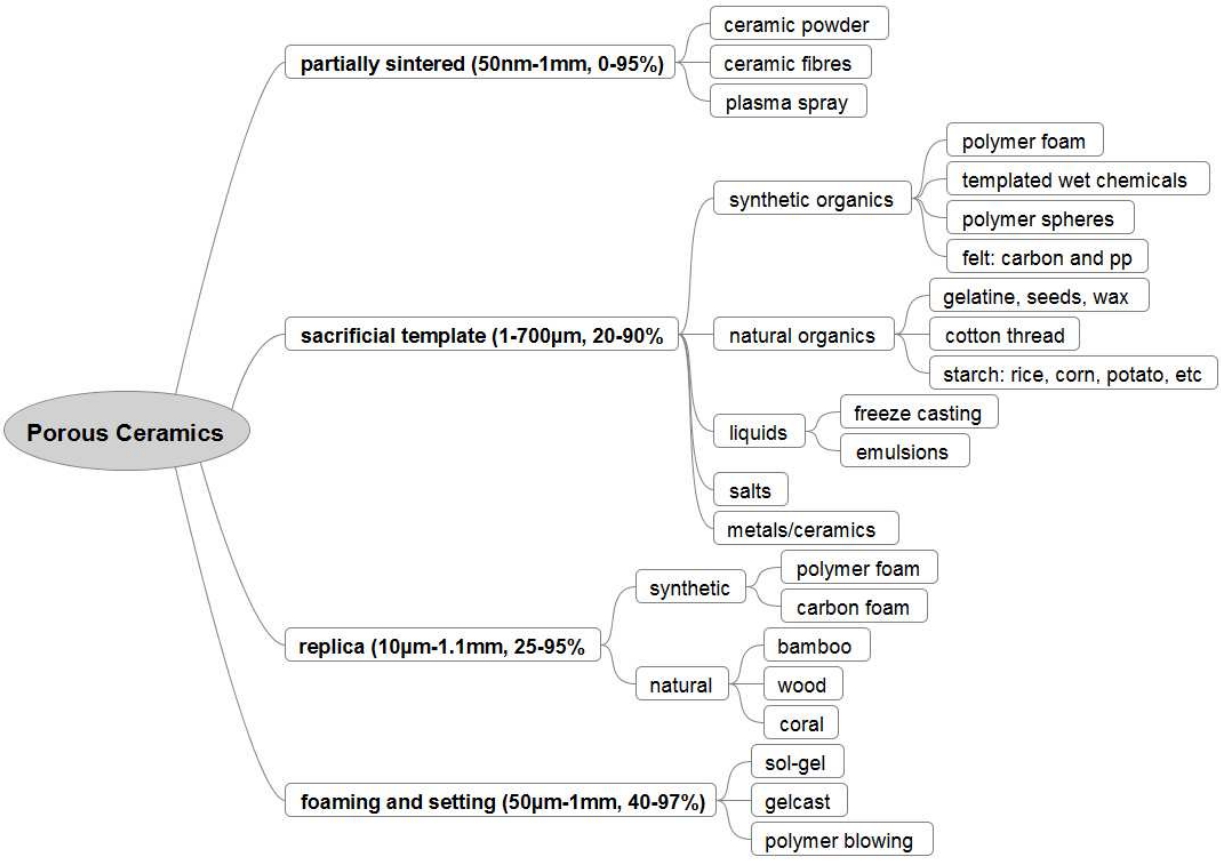

Figure 2.1: Overview of methods for producing porous ceramics [11, 13, 14].

homogeneously distributed within the microstructure [16]. Plasma spraying involves the spraying of molten or heat-softened material onto a surface to provide a coating. Ceramic powder is injected into a plasma flame, where it is rapidly heated and accelerated to a high velocity. The hot powder impacts on the substrate surface and rapidly cools forming a coating. A porosity of 15 % was reported by Travitsky et al. [7]

ii) Sacrificial template: The sacrificial material is added to the ceramic precursor (powder or slurry) then dried. The sacrificial material is then removed, either by pyrolisation, melting, evaporation or leeching. Finally the ceramic is sintered. This results in a porous ceramic body with a negative replica of the original sacrificial template. A wide variety of templates including network structures, pyrolysable particles, liquids, salts, metals and ceramics have been reported [11]. This wide range available provides flexibility in the ranges of achievable porosity and pore size, with 20 to 90 vol.% and 1 μm to 1 mm, respectively, being reported in the literature [11].

iii) Replica: The replica template material has a solid network structure, for example foam or wood. The template is infiltrated with a ceramic slip. Excess slurry is removed leaving a ceramic coating on the template, which is then dried. Upon heating, the template is pyrolysed and the ceramic coating sintered. This results in a 25 to 95 vol% porous ceramic body with pore sizes ranging from 10 to 130 μm for wood and 100 μm to

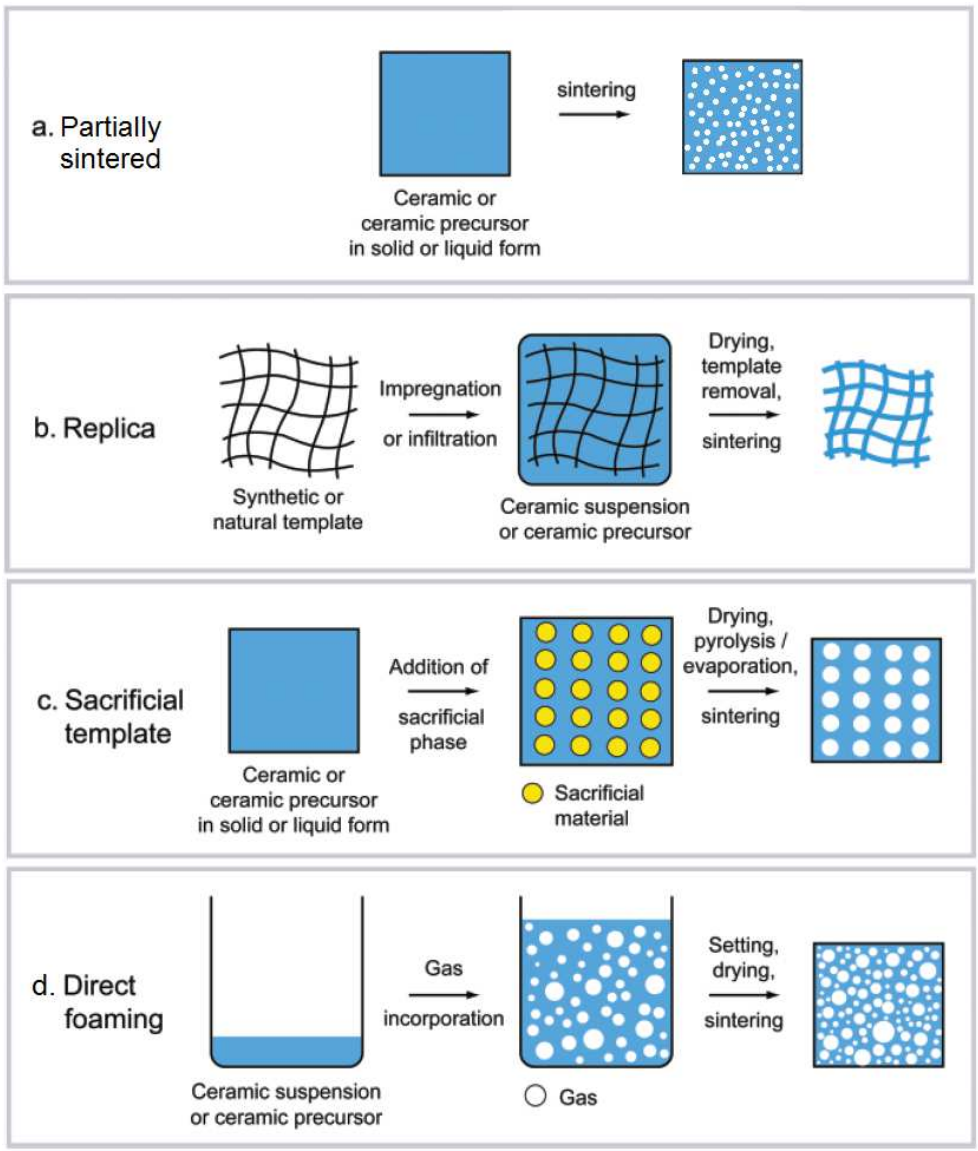

Figure 2.2: Processing routes for the production of porous ceramics [11].

1.1 mm for polymer foam [11]. The microstructure is a positive replica of the template, but with hollow struts. With a polymer foam replica, the triangular strut profile causes stress concentration at the corners and has been found to cause strut cracking and therefore lower strength [17, 18]. Wood has a radial structure and can contain knots and other irregularities [19].

iv) Foaming and setting: In this process gas is incorporated into a ceramic slip to form bubbles. A surfactant is used to stabilise the resulting ceramic foam. The foam is allowed to set and dry before sintering. There are numerous methods of incorporating the gas and stabilizing the ceramic foam, as described in reviews by Studart et al. [11] and Saggio-Woyanski et al. [13]. The resulting porosity can be either closed or open, depending on the stability of the foam. The achievable pore sizes are 50 μm to 1 mm.

Table 2.1: Largest pore space and entrance diameter of monomodal sphere packing relative to sphere size [21].

	loosest packing	most dense packing
entrance diameter	0.414	0.155
largest pore space	0.732	0.414

Partial sintering

Partial sintering of a pressed ceramic powder or dried ceramic slip results in a homogeneous pore distribution and pore size [16]. A ceramic slip can be cast, which results in a homogeneous density in the cast part. Using a compacted ceramic powder allows higher porosities to be achieved, but one is limited to a simple shape and it is more difficult to achieve homogeneity in the packing of the powder. When the powder is pressed, it has been observed that the shape of alumina grains are irregular and deviate from a spherical shape [20]. For a monomodal ceramic powder, the largest pore space and entrance diameter (smallest pore space) can be calculated as a function of grain size and packing density [21]. The factors for the highest and lowest packing densities are given in table 2.1. To obtain an entrance diameter of 1 μm, a ceramic powder with a grain size between 2.4 and 6.5 μm is required, depending on the packing density. For example, to achieve the target channel size of 1 μm, Skirl et al. used a ceramic powder with an average grain size of 5 μm [22].

Polymer foam and felt

The polymer foam (sacrificial template) method was developed by Lange et al. [14]. Schwarzwalder and Somers patented a similar method earlier in 1963 [10]. However, this replica method included a step of excess slurry removal resulting in high porosities from 50 to 95 %. In the method by Lange et al., polymer foam is infiltrated with a ceramic slip using pressure filtration, dried, and then pyrolysed to give a porous ceramic with a negative replica of the foam. The ceramic green body is then fully sintered. In this method the porosity of the ceramic body was limited by the density of the polymer foam: 2.5 % for low density foam and 15 % for high density foam. In order to achieve higher densities, the foam can be compression moulded before slurry infiltration [23–25]. The foam is typically compressed in one direction to give the desired porosity, typically to an eighth or tenth of the original thickness. An anisotropic structure is thus formed.

The structure of the porous ceramic formed in this method (figure 2.3) has a notable disadvantage [26]; the corners of the triangular pore channel cross section act as stress concentration points. During the stages of drying and sintering the ceramic shrinks. This

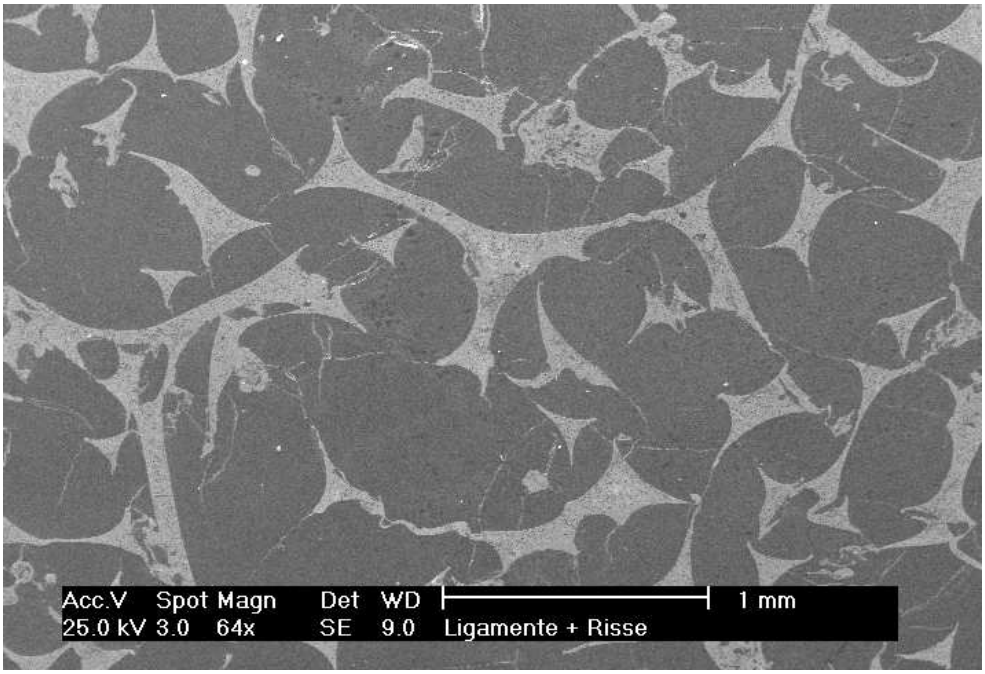

Figure 2.3: Electron microscope image of a polymer foam based alumina-copper composite. Copper-filled cracks in the ceramic phase can be seen [26].

leads to microcracking of the ceramic, typically at the stress concentration points, which in turn causes a decrease in the strength and elastic modulus of the composite.

It would thus be desirable to have a pore structure with rounded, rather than triangular, ligaments. One possibility proposed by Lange et al. was to use felt as the sacrificial preform [14]. However, no results were given, since the paper had concentrated on polymer foam. No other literature has been found mentioning felt. The rounded fibres in felt may potentially overcome the limitations of polymer foams. A novel variation on this method incorporates pyrolysis of the polymer foam to form carbon foam before slip infiltration [27]. However, this energy intensive step adds to the overall cost of the porous ceramic without any obvious benefits.

Pore forming agents

The use of so-called pore forming agents (PFA) as a sacrificial preform is well established [11]. In this method, pyrolysable particles are mixed into the ceramic slip, which is then dried and fired to burn out the particles and sinter the ceramic. The porosity and pore size of the resulting ceramic can be controlled by the amount of particles added to the slip and the size of the particles, respectively. Porosities ranging from 20 to 80 % can be achieved. Other pore forming agents mentioned in the comprehensive review by Studart et al. include polymer beads (PVC, PS, PVB, PMMA), cellulose, gelatine, seeds, starch powders, oil emulsions, salts, metal powder and carbon fibres and flakes [11]. Salts and

metal powder are removed by washing or leeching of the preform. This method can be combined with partial sintering to achieve a combination of macropores and micropores. Depending on the shape and distribution of the particles, at least 15 to 30 % PFA is required to achieve open porosity. Below this amount the porosity may be all or partly closed.

The main disadvantage of this process is that the 'windows' connecting the pores are much smaller than the pores themselves. This bottleneck leads to a lower permeability than what would be expected for the given pore size, which in turn requires higher pressures for metal infiltration. Care must be taken to ensure the PFA particles stay homogeneously distributed in the ceramic slip during casting and drying in order to ensure a homogeneous pore structure. Starch absorbs water leading to swelling of the particles and a larger-than-expected pore size. This also reduces the bottleneck effect, since the soft, swollen particles do not remain perfectly spherical, but rather compress together at points of contact resulting in larger pore windows. Mattern also reported clumps of alumina powder within the pores [28]. It is claimed to be due to the shrinkage of the starch particles during drying and pyrolisation. This was not observed with PMMA spheres, apparently since they neither wet the alumina slurry, nor do they shrink during the drying stage.

2.1.2 Metal infiltration

Due to the poor wettability of liquid copper on alumina (discussed further in section 2.1.3), pressure is required to infiltrate copper into the porous alumina preform. Widespread methods used include squeeze casting [14] and gas pressure infiltration [29]. Garcia-Cordovilla has written an extensive review on the subject [30].

a) Squeeze casting: The squeeze-cast method applied to porous ceramic preforms is described by Lange et al. [14]. Firstly, the porous ceramic preform and stainless steel die are preheated. The ceramic preform is then placed in the die. Molten metal in a separate crucible (100 to 150 K above the melting point) is poured over the ceramic. A hydraulic plunger then forces the molten metal into the pore channels of the ceramic preform at pressures around 100 to 200 MPa. The advantages of squeeze casting are that infiltration is carried out quickly, ceramic-metal reactions are thereby minimized, and a fine-grained microstructure without shrinkage voids can be achieved. The process is commonly used with alloys of aluminium, tin, zinc and silver. More recently, this method has also been applied to copper [31]. A disadvantage of this method is that some porous ceramics are not strong enough to withstand the high pressure applied, resulting in a crushed ceramic.

The ceramic preform must therefore be either strong or have a high permeability.

b) Gas pressure infiltration: Gas pressure infiltration of porous ceramics was first developed by Travitzky and Claussen [29]. The preform to be infiltrated is mechanically fixed to the bottom of an alumina crucible. The crucible is filled with pieces of plate metal and placed in a gas pressure furnace. The furnace is then heated above the melting point of the metal under vacuum to prevent oxidation of the metal. Pressure is applied by argon gas between 0.5 and 10 MPa forcing the metal into the pore channels of the ceramic preform. The system is then cooled below the melting point, continuing the application of pressure until the metal has solidified. This method requires that the infiltrated ceramic be cut out of the solid metal filled crucible. Knechtel et al. applied this method to infiltration of copper into porous alumina [1]. The temperature and pressure of infiltration were 1350 °C and 15 MPa, respectively. Even at this pressure, pores of 0.08 μm could not be infiltrated. Prielipp et al. improved the process by securing the ceramic preform from above and incorporating a lift to raise and lower the crucible [32]. After infiltration the system is cooled to just above the melting point. While maintaining the high pressure, the crucible is lowered until the infiltrated ceramic is no longer in the molten metal. The system is further cooled until well below the melting point and the pressure then removed. In this way the infiltrated preform does not need to be cut out of the crucible. This method is quite slow in comparison to squeeze casting: one day compared to a few minutes [14].

c) Pressureless infiltration: If the wetting angle of the molten metal on the ceramic is below 90° the infiltration can be carried out without applied pressure, typically under vacuum. Methods for altering the wetting angle of copper in order to enable pressureless infiltration are discussed in section 2.1.3. One major advantage of pressureless infiltration is that it is less expensive than the above two methods.

Alternative methods

A limited number of materials that exhibit spinodal decomposition can be used to created a composite in situ [15]. Commercial examples of this method include DIMOXTM and PRIMEXTM to produce alumina-aluminium composites. An alternative to molten metal infiltration is to fill the porous ceramic with metal via chemical vapour deposition (CVD) [15].

2.1.3 Ceramic-metal interface wetting

The wettability of a liquid on a solid substrate can be described by Young's equation [33]

$$\cos\theta = \frac{\gamma_{sv} - \gamma_{sl}}{\gamma_{lv}} \tag{2.1}$$

where γ_{lv}, γ_{sv}, and γ_{sl} represent the interface energies of liquid/vapour, solid/vapour and solid/liquid, respectively, and θ is the contact angle between the liquid drop and the solid substrate, as depicted in figure 2.4. If the contact angle is less that 90° the liquid is 'wetting', if greater than 90° it is 'non-wetting'. From equation 2.1 it is clear that a reduction in θ will result from increase in γ_{lv} or γ_{sl}, or a decrease in γ_{sv}.

Wetting can be classified as physical or chemical, depending on the nature of the bonding at the interface [34]. Physical wetting is due to reversible physical forces across the interface, such as Van der Waals forces or electrostatic attraction. In this case Young's equation can be used. The interface energy, γ, can, however, be influenced by adsorption of vapour at the solid-vapour interface [33] as described by equation 2.2:

$$\frac{d\gamma}{d\ln a} = -\Gamma RT \tag{2.2}$$

where a is the activity of the gas, which for an ideal gas can be replaced with pressure, Γ is specific adsorption, R is the universal gas constant and T is temperature.

Chemical wetting refers to chemical bonding across the interface. A reaction layer may form where both phases are in contact with the reaction layer rather than each other [35]. Young's equation is thus inadequate and must be modified. Aksay et al [36] proposed that the specific free energy of the reaction, Δg, be added to the solid-liquid interface energy, such that a negative Δg (required for spontaneous reaction) results in the lowering of γ_{sl}:

$$\gamma_{sl} = \gamma_{sl}^{o} + \Delta g \tag{2.3}$$

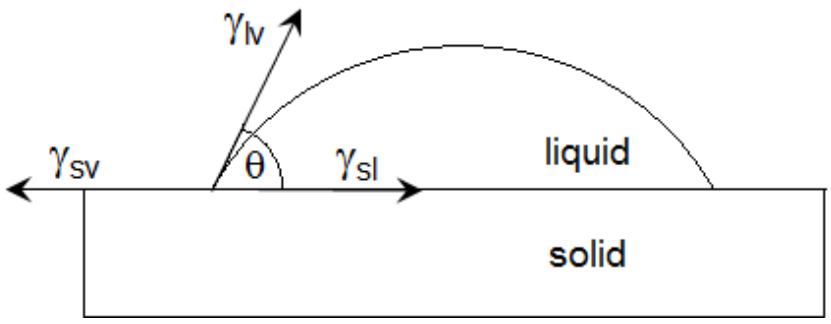

Figure 2.4: Schematic illustration of wetting.

where γ_{sl}^{o} is the initial or pure interfacial tension. It has been found that the equilibrium contact angle has the same value as the contact angle between the pure liquid metal and the reaction product layer, showing that the liquid metal wets the reaction product rather than the ceramic substrate [37].

The aforementioned equations all describe wetting and adhesion on a simple, flat surface. In order to consider curved surfaces such as pores or pore channels, pressure must be taken into account. The Laplace equation [33] shows that for a capillary with radius r_c, where the liquid forms a meniscus of radius R, the difference in pressure between a liquid and the surroundings, Δp, is expressed as:

$$\Delta p = \frac{2\gamma_{lv}}{R} = \frac{2\gamma_{lv}\cos\theta}{r_k} \tag{2.4}$$

The sign and effect of Δp depends on the contact angle. For $\theta < 90°$, Δp is positive and drives the liquid into the capillary. For $\theta > 90°$, Δp is negative and represents the minimum pressure required to force the liquid into the capillary. This effect is of particular interest in the production of ceramic-metal composites. The pressure required to infiltrate a non-wetting metal into a porous ceramic can be calculated. In wetting systems the metal should spontaneously infiltrate the porous ceramic without any required external pressure.

Wetting of liquid metals on oxide ceramics

In most cases, liquid metals do not wet oxide ceramic surfaces [38]. This is thought to be due to differences in bonding type across the interface, from ionocovalent bonding in the ceramic to unsaturated bonding in the metal. There are two types of metal-oxide ceramic interactions: reactive and nonreactive. Examples of elements forming a reactive system with alumina include Ni, Si, Fe and Al [39]. Nonreactive elements include Pb, Sb, Sn, In, Ga, Ag, Au and Cu. If the metal reacts with alumina to form a metal oxide then it is reactive, else nonreactive [36]. Wetting of a pure metal on an oxide ceramic is in general enhanced by alloying with a metal with a high affinity for oxygen, e.g. Ti, or with oxygen via metal oxide or oxide atmosphere.

Wetting of copper on alumina

Copper is non-wetting on alumina. Reported values of the contact angle of copper on alumina vary between 124° [40] and 170° [39]. The pressure required to infiltrate pure copper into an alumina preform is approximately 10 to 15 MPa [1, 4]. This causes the production of alumina-copper composites to be rather time-intensive and thereby expensive. By increasing the wettability of this system, it may be possible

to achieve pressureless infiltration, thereby simplifying production and increasing the financial viability of the composite material [41]. Two popular methods for improving the wettability of copper on oxygen are outlined in the following paragraphs.

i) Oxygen: A copper-oxygen alloy is formed by either mixing CuO into the copper or using an oxygen-containing gas atmosphere. Varying the oxygen partial pressure between 10^{-15} and 10^{-6} leads only to a decrease in the contact angle to around 110°. At oxygen partial pressures from 10^{-6} to 10^{-3} there is a marked decrease in contact angle to approximately 70°. Meier [42] explored the effect alloying copper with oxygen. Up to 2.5 wt.% oxygen, the contact angle decreased to 25 %. In the miscibility gap from 2.5 to 7.5 wt.% the wetting angle remained approximately constant, with a further decrease to 12 ±4° up to 11 wt.% oxygen. At the CuO-alumina interface, the formation of Cu_2O or $CuAlO_2$ has been observed [43]. The work of adhesion was found to increase with increasing weight percent oxygen [42]. A thin (1-4 μm), discontinuous layer of $CuAlO_2$ has been measured to increase the interface strength [43], whereas a thicker (10-100 μm) layer causes a decrease in interface strength [44] due to the crack growing along the brittle $CuAlO_2$ layer.

ii) Titanium: The wettability of copper on alumina can be enhanced by alloying with titanium, which is a typical reactive wetting system [45]. Kritsalis [46] observed that the contact angle decreased to 26° as the amount of Ti was increased up to 10 mol%. Above this amount there was little change. The Cu-Ti alloy reduces the alumina surface to form a wettable reaction product TiO. Unlike the CuO-alumina system, it takes many hours for the equilibrium contact angle to be achieved since the reaction is controlled by segregation of Ti to the interface [38] and diffusion [34]. Although the equilibrium contact angle is low, spontaneuos infiltration of Cu-Ti into porous alumina has not been observed [35]. No data was found on the interface strength of Cu-Ti on alumina.

2.1.4 Residual stress, cavitation and microcracking

Regardless of how a ceramic-metal composite is produced, it is conducted at high temperatures. The metal and ceramic components generally have differing coefficients of thermal expansion, α, with $\alpha_{metal} > \alpha_{ceramic}$. When the composite is cooled to room temperature, this mismatch in α causes hydrostatic tensile stresses to form in the metal and compressive stresses to form in the ceramic [47]. This is known as residual stress. Due to its hydrostatic nature, the tensile stress in the metal component can reach levels up to 20 times the yield stress without necessarily yielding [48]. The magnitude of the residual stresses can be measured via neutron diffraction [49–51]. There is a large scatter in the residual stresses of the metal phase due to microstructural parameters: the most

narrow and sharpest areas have the highest stresses which can only be relieved by plastic flow [22].

Skirl [52] explored the effect of metal content and metal ligament diameter on the measured residual stresses in the metal and ceramic phases via neutron diffraction. When the metal content was decreased, the average compressive stress in the alumina decreased and the average tensile stress in the aluminium increased. However, if the microstresses within the aluminium were taken as stress variations, it was found that the maximum value of stress was the same for all metal contents. Assuming pure elastic strain, the residual stress for a particular metal content should be independent of the metal ligament diameter. However, Skirl found the residual stress to increase significantly with decreasing metal ligament diameter, which indicates plastic strain within the metal phase. The flow stress and thus the maximum stress achievable is increased by the increased mechanical constraint of smaller metal ligaments, which hinders yielding. For a particular ligament diameter, the maximum stress is independent of metal content. This supports that idea that the yield stress depends on the amount of constraint.

The residual stress can only be relieved by plastic flow. In composites with a strong interface, like alumina-aluminium, cavitation, that is, the formation of pores within the metal, may occur. In composites with a weak interface, like alumina-copper, the metal may delaminate from the ceramic to form microcracks [32, 48]. In TEM investigations of alumina-aluminium and alumina-copper, Prielipp et al. [32] found no microcracking at the phase boundaries of alumina-aluminium, microcracking at 50 % of interfaces for a coarser structured alumina-copper (partially sintered alumina with a grain size of 4 μm) and no microcracking in a finer structured alumina-copper (partially sintered alumina with a grain size of 1.2 μm). This observation is contrary to the observation that residual stress increases with decreasing ligament diameter, since a higher amount of residual stress would be expected to lead to a higher amount of microcracking in a composite with a weak interface. In alumina-Ni_3Al microcracking was observed in up to 50% of the interfaces, concluded to be due to the weak interface [53]. Residual stress and microcracking can have a significant effect on the elastic modulus, fracture behaviour [1, 32] and the thermal expansion behaviour [2, 22, 51, 53] of a composite. This will be described in more detail in section 2.2

2.2 Properties of ceramic-metal composites

2.2.1 Young's modulus

The Young's modulus, E, of metal-ceramic composites generally lies between that of the two components. Many models have been developed to describe the variation in E as a function of composition, depending on the composite structure, the range of composition, the ratio of the elastic moduli and the interface strength between the two components. Here, a brief description of two models is given. More exhaustive reviews include [54–56].

Rule of Mixtures (RoM): The rule of mixtures has upper and lower bounds for predicting the elastic properties of composite materials. The upper boundary, developed by Voigt [57], assumes constant strain across the composite. For example, in a lamellar structure, this would represent the loading of the composite parallel to the boundaries between layers with the same strain in each layer (figure 2.5 a)). The lower boundary, developed by Reuss [58], assumes constant stress throughout the composite. In a lamellar structure, the load is applied perpendicular to the boundary between layers, with the same stress in each layer. The equations for the Voigt (U) and Reuss (L) boundaries of E are:

$$E_U = f_1 E_1 + f_2 E_2 \tag{2.5}$$

$$E_L = \frac{E_1 E_2}{f_1 E_2 + f_2 E_1} \tag{2.6}$$

with f_1 and f_2 representing the volume fraction of phases 1 and 2, respectively.

These bounds represent the widest possible variation elastic modulus according to the principles of minimum potential and complementary energy. Neither of these bounds alone predict actual values for the elastic modulus, nor does this model take into account the structure of the composite.

Hashin-Shtrikman Bounds (HS) [60]: This model considers isolated spherical inclusions surrounded in a layer of a second phase (figure 2.5 b)). The upper and lower bounds were derived using the variational principle: an energy-based approach to find the extreme situations corresponding to minimum potential and complimentary energies. Firstly, the bounds for the bulk modulus, K_{HS}, and the shear modulus, G_{HS}, are calculated using the following equations:

$$K_{HS} = K_1 + \frac{1 - f_1}{\frac{1}{K_2 - K_1} + \frac{3f_1}{3K_1 + 4G_1}} \tag{2.7}$$

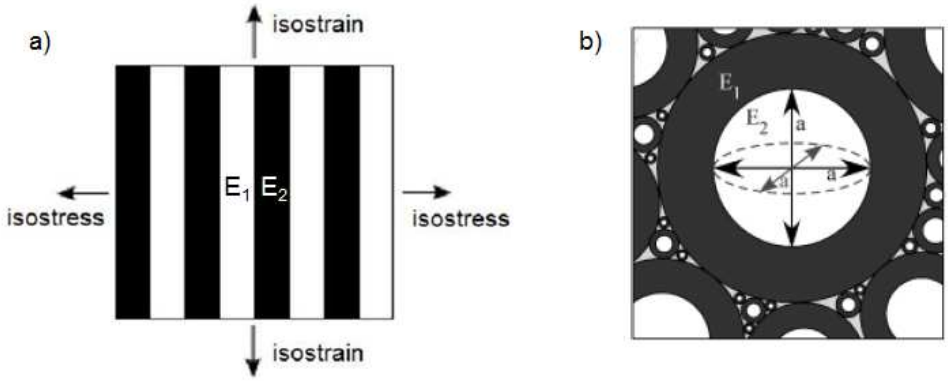

Figure 2.5: Schematic phase geometries for a) the rule of mixtures [59] and b) the Hashin-Shtrikman model (image adapted from [54]).

$$G_{HS} = G_1 + \frac{1 - f_1}{\frac{1}{G_2 - G_1} + \frac{6(K_1 + 2G_1)f_1}{5G_1(3K_1 + 4G_1)}} \tag{2.8}$$

where K and G are the bulk and shear modulus, with subscripts 1 and 2 representing the two different phases. The upper bound is when phase 1 (the matrix) is the stiffer phase. The lower bound is when phase 2 (the inclusion), is the stiffer phase. Both moduli of one material must be greater than both moduli of the other material; otherwise these bounds fail. The upper and lowers bounds for the composite elastic modulus are then calculated with equation 2.9 using the upper and lower bounds of K_{HS} and G_{HS}:

$$E_{HS} = \frac{9K_{HS}G_{HS}}{3K_{HS} + G_{HS}} \tag{2.9}$$

These bounds are the widest possible for an isotropic composite, if no structural information is known. That is, when only the properties and volume fractions of the two phases are considered. These bounds are an exact solution for a composite consisting of a matrix with spherical particles embedded in it [60]. For the Young's modulus of a metal-ceramic composite, the upper bound would correspond to a ceramic matrix composite and the lower bound to a metal matrix composite.

Young's modulus of ceramic-metal composites in the literature

No literature was found on the variation of elastic modulus with metal content for alumina-copper composites. Moon et al. [54] investigated the variation in elastic modulus in alumina-aluminium composites with metal content ranging from 5 to 97 vol.% using the resonance frequency method. The experimental data lay within the HS bounds over the entire composition range. In the alumina rich range, the experimental results fit the lower boundary quite well, even though the lower boundary

would correspond to an MMC. For alumina poor composites, E was between the two bounds.

In order to achieve the wide range of metal contents, a few different phase morphologies were used by Moon et al. [54]. This had only a very limited influence on the measured composite modulus in comparison to the composition. Mattern [28] also found the variation in elastic modulus with metal content for this system to be independent of the phase morphology.

The interface of alumina-aluminium is relatively strong compared to the copper-alumina interface. One system with a weak interface (like alumina-copper) is alumina-Ni_3Al. Skirl et al. [53] found the values of elastic modulus with varying Ni_3Al content to be below that even of the lower rule of mixtures. This was attributed to microcracking between the Ni_3Al and alumina. Since both models assume a strong interface, they cannot account for the effect of a weak interface or microstructural imperfections.

2.2.2 Fracture toughness

Fundamentals of fracture mechanics

The following section provides a brief overview of the fracture mechanics concepts relevant to crack propagation in interpenetrating network composites. A more comprehensive explanation of mechanics theory can be found in references [56, 61–63].

There are three types of loading that can be applied to a crack within a material. Mode I is tensile stress applied perpendicular to the crack plane. Mode II is shear stress applied in the direction of crack growth. Mode III is torsion stress applied parallel to the crack front. In the following, only mode I will be considered, as this is what leads to failure in most brittle materials [61].

For mode I loading in the plane of a long through crack ($\theta = 0$) in an infinite plate, the following expression for the applied stress intensity factor, K_{IA}, in terms of crack length, c, and applied stress, σ, has been derived [61]:

$$K_{IA} = Y(c)\sigma\sqrt{c} \tag{2.10}$$

where $Y(c)$ is a crack length dependent shape factor describing the geometry of the crack and the mode of load applied. The shape factors for numerous experimental configurations has been analytically derived and can be found in a number of publications [56, 61, 64].

Early considerations of fracture mechanics were only applicable to materials displaying linear elastic behaviour where Hooke's law, $E = \frac{\sigma}{\varepsilon}$, is obeyed (Linear Elastic Fracture

Mechanics, or LEFM). Most materials exhibit some degree of plasticity near the crack tip, known as the plastic zone. If the plastic zone is much smaller than the thickness of the sample, the linear elastic fracture mechanics approach is still valid. For large amounts of plasticity, LEFM is inadequate and another model accounting for plasticity must be used.

Crack growth occurs when the applied stress intensity factor, K_{IA}, has reached a critical value K_{I0}. This describes the stress intensity factor required to initiate crack growth in the absence any toughening mechanisms at the crack tip, that is, the crack tip toughness.

Crack initiation and growth can also be considered in terms of the energy release rate, G. A crack can only form and grow if this causes the total energy of the system to stay constant or decrease, that is, that the energy available for crack growth is larger than the energy required to create two new surfaces [65, 66]. The resistance to crack growth, R_o, is defined as work required to create two new surfaces $R_o = 2w_f$. Crack growth proceeds when G has reached a critical value:

$$G = R_o = 2w_f \tag{2.11}$$

This is analogous to K_{IO}, the crack tip toughness, described above. Equation 2.12 gives the relationship between G (or R) and K for linear elastic behaviour:

$$G = \frac{K^2}{E'} \tag{2.12}$$

where $E' = E$ for plane stress and $E' = E/(1-\nu^2)$ for plane strain.

R-curve behaviour

Materials in which two smooth surfaces are formed upon crack propagation have a constant crack resistance, that is, $R = R_o$, $K_R = K_{I0}$ (provided there is no process zone ahead of the crack tip such as phase transformation or ferroelasticity). If there are toughening mechanisms present during crack propagation, such as crack branching or bridging, the crack resistance increases with increase in crack length (Δc) according the following equations:

$$\begin{aligned} K_R(\Delta c) &= K_{I0} + K_\mu(\Delta c) \\ &or \\ R(\Delta c) &= R_o + R_\mu(\Delta c) \end{aligned} \tag{2.13}$$

where $K_\mu(\Delta c)$ and $R_\mu(\Delta c)$ represent the crack length dependent contribution of the microstructure to crack resistance, also known as the microstructural shielding term.

This part contains all the crack closing stresses from the crack tip until the last intact crack bridge. K_μ and R_μ are related by the following equation [67]:

$$R_\mu = \frac{K_\mu^2 + 2K_{IO}K_\mu}{E'} \tag{2.14}$$

The energy approach allows, within limits, the elastic-plastic behaviour of crack bridging elements to be determined. The dispersed bridging energy of a crack bridging element, $R_{\mu i}$, can be calculated from the integral of the crack closing stresses, $p_i(u)$, from the crack tip to the crack opening, $u*$, at which a bridging element has failed:

$$R_{\mu i}(c) = f \int_0^{u*} p_i[u(c)]]du \tag{2.15}$$

where f = the area fraction of the crack bridging elements

The resistance curve or R-curve is a graphical representation of K_R or R as a function of Δc. Whether a crack grows in a stable or instable manner depends on how G and R, or K_A and K_R vary with crack length:

$$\text{stable crack growth: } \frac{dG}{dc} < \frac{dR}{dc} \text{ or } \frac{dK_A}{dc} < \frac{dK_R}{dc}$$

$$\text{instable crack growth: } \frac{dG}{dc} > \frac{dR}{dc} \text{ or } \frac{dK_A}{dc} > \frac{dK_R}{dc}$$

Stable crack growth requires increasing load to maintain crack growth, whereas instable crack growth leads to spontaneous fracture. The transition is at the point where the G-curve is tangent to the R-curve or the K_A curve is tangent to the K_R curve. At this point, K_A has reached a critical value of stress intensity, K_{IC}, called the fracture toughness. G_{IC} is analogous. K_R can be determined experimentally, as long as the Young's modulus of the material is known. This is advantageous when the shape factor of the given material and loading conditions cannot be determined analytically.

Determination of crack tip toughness and the microstructural shielding term

The crack tip toughness of a material is an important parameter representing the stress intensity factor when crack growth begins. In practice it is difficult to measure directly, since crack extension measurements are usually measured starting from a notch or a sharp crack that has be cut to make it a short crack (to remove the bridged zone). This method was developed by Steinbrech and Knehans [68] in order to measure the R-curve behaviour of alumina as a function of grain size. However, in this method it is essential

to have a continuous crack front. This necessitates a minimum crack length of 100 to 200 μm, where it is not possible to ignore the effects of a crack bridging region.

Fett et al. [69] developed a method to determine K_{IO} using a strain gauge to detect the first deviation from linearity in the load-displacement measurement of a V-notched beam under four-point loading. K_{IO} can also be determined by measuring the profile of a crack under load, also called **c**rack **o**pening **d**isplacement or COD. The width of the crack is measured from the tip of the crack, through the bridged region to well within the unbridged region of the crack. Ideally this would be measured at the critical load. However, since this would lead to crack extension, the crack profile is measured at one or more loads below the critical load and extrapolated to the critical load. Using the Irwin equation [70], K_{IO} can be calculated by fitting an appropriate function to the first 50 to 100 μm of the crack profile (equation 2.16):

$$u(x) = \frac{K_{IO}}{E'}\sqrt{\frac{8x}{\pi}} \tag{2.16}$$

Results obtained with the COD method have shown that the strain gauge technique overestimates K_{IO} [71]. Kounga et al. [72] developed a more rigorous mathematical approach based on the Irwin equation. It takes the whole of the measured COD into account when calculating K_{IO}. However, since this yielded similar results to the Irwin approach, the simpler Irwin approach is used in this work. Different methods used to measure the crack profile include optical interference [73], SEM [74], Raman microscopy [75] and atomic force microscopy [76]. Once K_{IO} has been determined, $K_\mu(\Delta c)$ can thus be determined according to equation 2.14.

Toughening mechanisms

There are two broad categories of toughening mechanisms: process zone mechanisms and crack bridging mechanisms. In some ceramic materials and CMCs the high stress at the crack tip triggers particular processes in a finite area around the crack tip. This is known as a process zone. Some examples are localised microcrack formation (which in contrast to thermally induced microcracks do not weaken the material), phase transformation or ferroelastic domain switching. As the crack grows into the process zone, this zone applies closure stresses to the crack wake such that a higher load is required for further crack propagation. Since this category is not relevant to alumina-copper composites, this will not be dealt with further. Of particular relevance are crack bridging mechanisms. These have been discussed in detail by Rödel [67]. The four major categories are: i) elastic or intact bridges, ii) plastic or friction bridges, iii) elastic-plastic or mechanically interlocking bridges and iv) ductile bridges. These categories are illustrated in figure 2.6. In interpenetrating metal-ceramic composites,

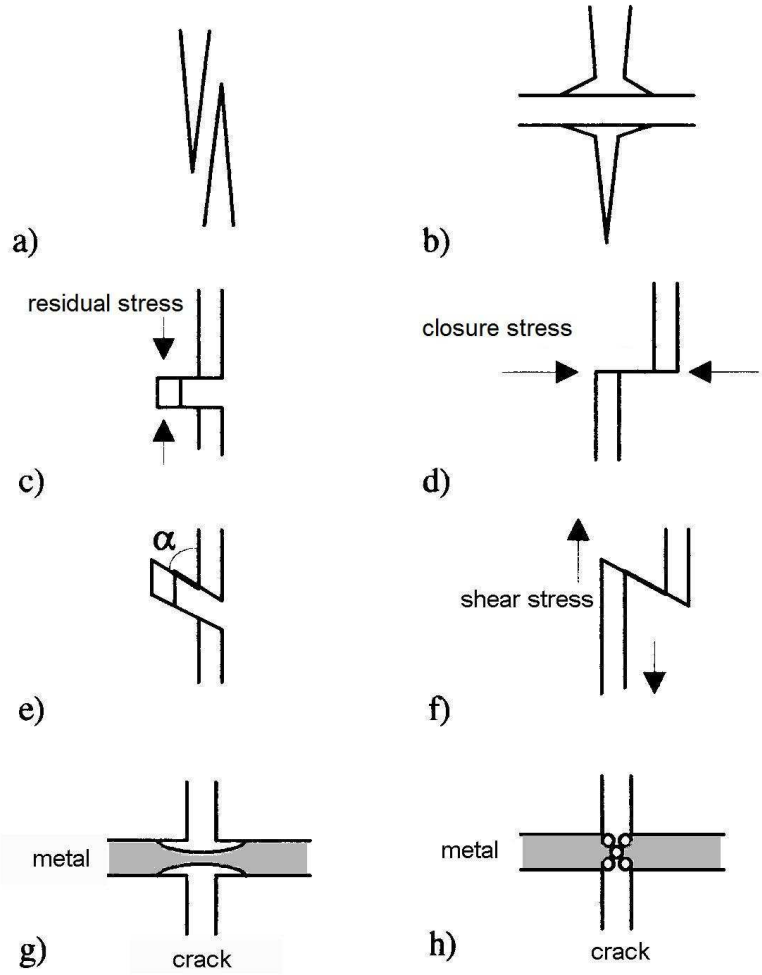

Figure 2.6: Schematic representation of possible bridging mechanisms: a) and b) intact (elastic) bridges with a) constant delamination length and b) increasing delamination length; c), d) friction (plastic) bridges of different geometries; e) and f) different forms of mechanical interlocking; ductile bridges with failure due to g) necking or h) cavity formation [67].

the dominant toughening mechanism is due to ductile bridging. Many aspects of the metallic bridges can affect the toughening behaviour:

1. the morphology including metal ligament diameter, ligament orientation and metal content
2. the properties of the metal like yield strength, Young's modulus and ductility
3. the interaction between the metal and ceramic phases including interface strength and difference in thermal expansion coefficients

By tailoring the microstructure of the metallic network via the porous ceramic preform it is possible to influence the $p(u)$ function and thus the mechanical properties of the composite. The influence of the metal ligament diameter on the $p(u)$ function and the

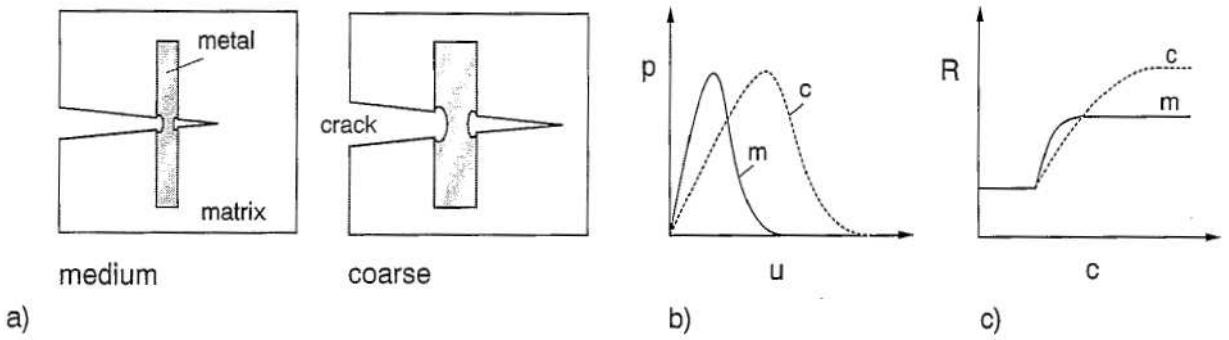

Figure 2.7: Schematic diagram describing b) $p(u)$ functions and c) R-curves for metal reinforced ceramics with varying metal ligament diameter a), based on the assumption of scale independent metal deformation [32].

R-curve is shown in figure 2.7. During crack propagation finer metal ligaments lead to a steeper $p(u)$ curve with a smaller critical crack opening at which the ligament fails. The area under the curve is proportional to the energy absorbed by the bridging elements. Finer ligaments can only accommodate limited dislocation motion (plastic deformation) and thus only dissipate a limited amount of energy. In coarser metal ligaments more dislocation motion is possible, thus the plastic deformation and dissipated energy is larger. This leads to smaller crack closure stresses for a given crack opening and an increase in the critical crack opening. The initial slope of the $p(u)$ curve is reduced, while the peak value remains constant and is shifted to a higher u. Similarly, the slope of the R-curve is also lower. The plateau value of crack resistance is higher since the coarse ligaments are able to accommodate more strain. The fracture toughness is higher due to the higher plateau but the fracture strength lower due to the lower slope of the R-curve.

The effect of metal content on the R-curve is shown in figure 2.8. With increasing metal content both the slope and the peak of the R-curve are higher. For a constant metal ligament diameter, with increasing metal volume fraction, the ligaments must be closer together, resulting in a steeper slope. A higher metal content means that more energy is absorbed by plastic deformation, hence the higher plateau. Thus with increasing metal content, both the fracture toughness and fracture strength increase.

Not just the morphology of the composite effects the $p(u)$ curves; the properties of the metal phase also play a role. The yield strength, Young's modulus and ductility of the metal phase also have an effect on the $p(u)$ function. A higher yield strength enables each ligament to withstand a higher stress before failing, thus increasing the peak value. A higher Young's modulus would increase the initial slope of the $p(u)$ curve, analogous to a stress-strain curve. An increased ductility would enable each ligament to plastically deform further and absorb more energy before failing, thus shifting the peak of the $p(u)$ curve to higher u values.

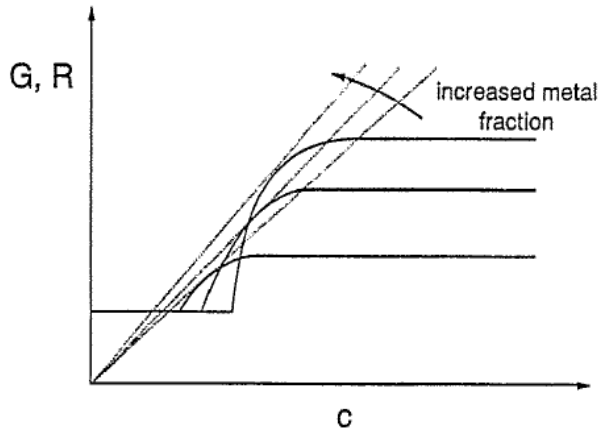

Figure 2.8: Schematic diagram describing the effect of metal fraction on the R-Curve [32].

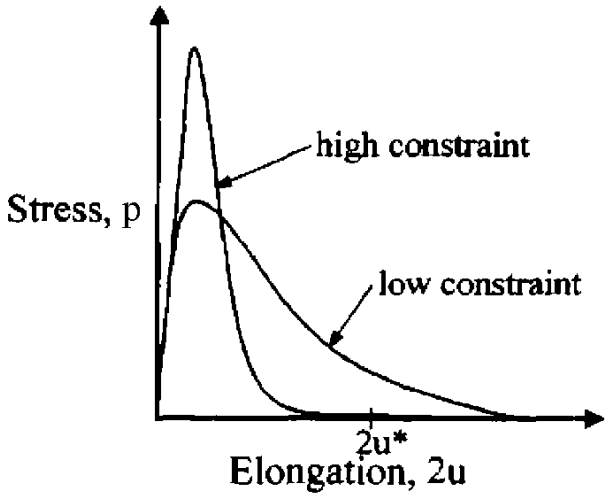

Figure 2.9: Schematic diagram describing the variation in the $p(u)$ function with varying constraint of the metallic phase [77].

The interaction between the metal and ceramic phases also influences the $p(u)$ curve. A high interface strength means that the metal ligaments are highly constrained and vice versa. The effect of mechanical constraint is shown in figure 2.9. A low interface strength between the two phases causes delamination between the metal ligament and the ceramic during crack propagation. The length of the ligament able to plastically deform is longer, meaning more energy can be dissipated leading to a higher toughness value. As mentioned in section 2.1, the higher the difference in thermal expansion coefficient between the metal and ceramic phase, and the higher the processing temperature, the more thermal residual stress is present within the composite. This is before any external load is applied. The compressive stress present in the ceramic phase is advantageous, since more opening stress can be applied before the compressive stress is reversed and the tensile stress for crack growth is reached. The tensile stress present in the metallic phase would allow for less elastic deformation before the yield stress is achieved and plastic flow occurs.

2.2.3 Thermal expansion and conductivity

Thermal strain

In homogeneous materials, the strain-temperature curves generally follow the same path for heating and cooling. In metal-ceramic composites the thermal expansion behaviour is more complicated. Skirl et al [22] found the strain curves of interpenetrating alumina-aluminium composites to be hysteretic, with the strain curve higher upon heating and lower upon cooling. The total strain increased linearly with metal content, but the amount of hysteresis was unaffected. The hysteresis was proposed to be due to one or more of the following reasons: i) flow of metal into residual porosity[1], ii) microcavitation in the metal phase formed during cooling after production, or iii) intrusion/extrusion of metal ligaments at the surface of the sample ($\approx 6.5\ \mu$m). Hoffman et al [2] explained the results from Skirl et al using two different models. The first approach was a macroscopic consideration of the total composite strain based on the variation of stress in the metal phase during thermal cycling. The second approach was a micromechanical consideration of time-dependent effects in the metal phase, such as creep. Figure 2.10 a) is a representation of the effect of stress and plastic flow in aluminium upon macroscopic thermal expansion. This describes the typical hysteretic strain curve of the alumina-aluminium composites. Figure 2.10 b) schematically shows the variation of stress in aluminium as a function of temperature. The different regions in the curve are explained in detail in [2] so only a brief description of regions 1 to 5 will be given here.

Curve 1: Starting at T_{visc}, upon cooling the metal shrinks elastically and tensile stress builds up.

Curve 2: There is a decrease in the slope of the curve when the tensile yield stress of the metal is reached with further strain requiring plastic deformation. The stress in the metal remains constant. Here cavitation or delamination may occur.

Curve 3: Upon reheating the metal expands elastically and is parallel to curve 1. The tensile stress in the metal is reduced to zero and compressive stress builds.

Curve 4: When the compressive yield stress of the metal is reached the slope of the curve decreases and the stress in the metal remains constant. The balance between thermal strain and gradual reduction of plastic strain leads to the slope of the curve (CTE) being less than that of pure alumina.

[1] only 0.05 to 0.29 % needed for 15 to 35 vol.% metal

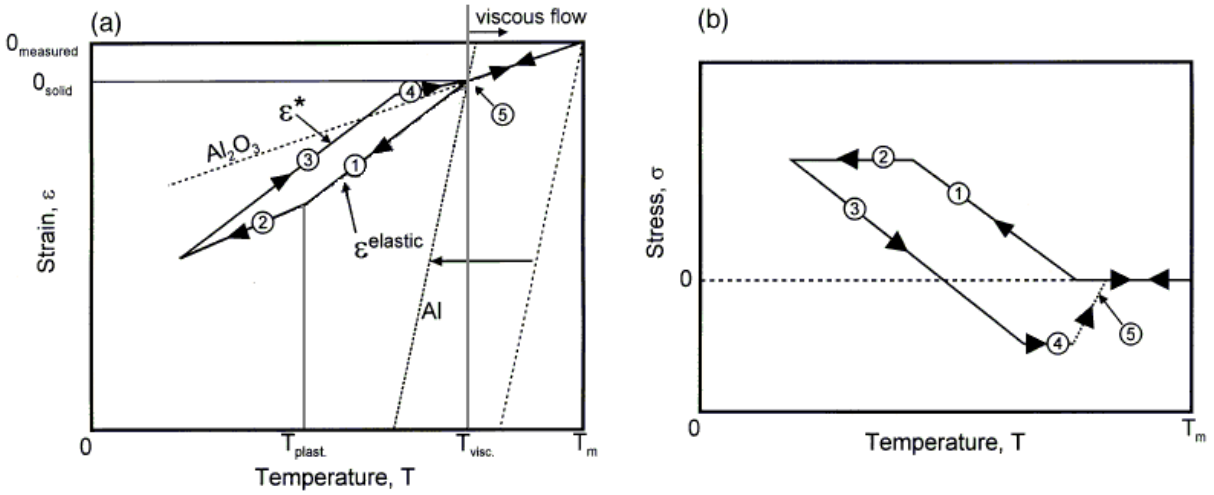

Figure 2.10: (a) Schematic representation of the effect of plastic flow in the aluminium upon macroscopic strain $\varepsilon*$ and the application of approach 1 to calculate (b) stress in the metal phase as a function of temperature [2].

Curve 5: T_{visc} has been reached as the metal flows viscously, leading to a relaxation of stress to zero. The slope of the composite strain curve approaches that of pure alumina.

The second model considered the effects of different creep mechanisms at different temperatures, but was acknowledged to be inappropriate in the case of extensive cavitation or microcracking, as might be expected in alumina-copper. It was concluded that the plastic deformation of the metal was largely due to diffusion based processes at high temperatures and a limited amount of cavitation yielding close to room temperature.

Alumina-aluminium has a strong interface whereas alumina-copper does not. Since no publication on the thermal strain behaviour of alumina-copper were found, the thermal strain behaviour of another system with a weak interface, alumina-Ni_3Al, is briefly described here. Skirl et al. [53] found there to be no hysteresis in strain curve up to 900 °C. Between 900 and 1000 °C there was a small hysteresis. It was presumed that there was only elastic deformation of Ni_3Al below 900 °C and that the weak interface prevented a stress build up. For the same reason it was assumed there was only a minimal amount of residual stress present after production (see also section 2.1 on residual stress), although this was not measured. The total strain increased with increasing Ni_3Al content, but the amount of hysteresis was not significantly affected.

Coefficient of thermal expansion (CTE or α)

CTE is calculated either as an average value across a particular temperature range, $(\Delta\varepsilon/\Delta T)$, or as an instantaneous value, $(d\varepsilon/dT)$, and is often plotted against

temperature. There are a number of different models to predict the variation in CTE with composition in two component composites. The simplest is the Wiener model [78, 79], analogous to the rule of mixtures (RoM), but derived for thermal and electrical properties. In equation 2.5, E is simply replaced with α. This assumes that both phases are able to slide freely and do not exert a force upon each other. There are two different models to predict the CTE of composites with a strong interface, where both phases deform elastically; the Kerner and Turner models.

i) The Kerner model [80]: considers a spherical particle of one phase enclosed by a matrix (perfectly bonded), as in an MMC or a CMC. By using an averaging procedure due to Bruggeman [81], and analysing the effect of a uniform hydrostatic compression and of a uniform tension on an average grain, an equation for the bulk modulus was found. The composite CTE was found from an analysis of the dilatation and bulk stress when the composite as a whole is subjected to some small temperature change:

$$\alpha = f_1\alpha_1 + f_2\alpha_2 + \left[\frac{4G_2}{K_c}\right]\left[\frac{(K_c - K_1)(\alpha_2 - \alpha_1)f_1}{4G_2 + 3K_1}\right] \tag{2.17}$$

where subscript 1 and 2 represent the outer phase and inner phase, respectively, K is the bulk compression modulus, G is the shear modulus and K_c is the bulk compression modulus of the composite, given by the Hashin-Shtrikman equation (equation 2.7). This gives an upper bound for when the less stiff phase is the matrix (MMC), and a lower bound for when the more stiff phase is the matrix (CMC).

ii) The Turner model [82]: a purely hydrostatic stress is applied and it is assumed that there is a homogeneous strain across the composite. No shape factor is taken into account. This was one of the first models for composite CTE that took the elastic constants of the constituent phases into account. This model would be expected to be more suitable for interpenetrating composites [22, 83], since the interpenetrating structure would cause constraint of each phase such that the strain should be homogeneous throughout the sample, which is not the case with MMCs or CMCs (Kerner model). The equation for the composite CTE is:

$$\alpha = \frac{f_1K_1\alpha_1 + f_2K_2\alpha_2}{f_1K_1 + f_2K_2} \tag{2.18}$$

For alumina-aluminium, Skirl et al. [22] found the average CTE from 100 to 180 °C, where thermal strain is purely elastic, to fit the upper Kerner bound, despite the fact that the Turner model would be expected to be more accurate for an interpenetrating composite. The average CTE from 200 to 280 °C, where there would be a limited amount of ductile flow in the metal, was found to fit the rule of mixtures. The instantaneous CTE showed a large hysteresis with a crossover around 400 °C. Below 400 °C the CTE was

markedly lower upon cooling than heating. Above 400 °C the CTE was somewhat lower upon heating. The lower CTE in the respective regions was concluded to be due to plastic strain in the metal phase restricting the thermal strain. Hsieh et al. [84] measured the thermal expansion behaviour of alumina-Ni_3Al composites from 0 to 100 % alumina and found the Kerner and Turner models the only bounds to be able to encompass all experimental data.

Thermal conductivity

The most important mechanism of heat transfer in solid materials is conduction. The ability of a material to transport heat is described by λ, the thermal conductivity (unit W/mK). This describes the heat flow, dQ/dT, through the cross section of a material with an area, A, that is under a temperature gradient of dT/dx. The relationship is analogue to the equation for diffusion:

$$\frac{dQ}{dt} = \lambda A \frac{dT}{dx} \tag{2.19}$$

Thermal conductivity can be measured using either steady-state methods or transient methods.

i) Steady-state: In steady state methods, the temperature difference across a sample is constant. For example, if a temperature difference, ΔT, across a sample of length, L, and cross section, A, is applied using electrical power ($P = V^2/R$) with a known voltage, V, and resistance, R, in ohms, to supply the heat flow $dQ/dt = P$, equation 2.19 can be rearranged to calculate the thermal conductivity:

$$\lambda = \frac{V^2 L}{RA\Delta T} \tag{2.20}$$

This method is mathematically simple, however, requires a constant temperature difference across the sample to have been achieved. This can be time consuming.

ii) Transient: In transient methods, the change of temperature over time is measured. The differential equation for heat transport is analogue to Fick's second law of diffusion:

$$\frac{dT}{dt} = a \frac{\partial^2 T}{\partial x^2} \tag{2.21}$$

where a is the thermal diffusivity of the material. To determine thermal conductivity, the following relationship is used:

$$\lambda = a \rho C_p \tag{2.22}$$

where C_p is the heat capacity and ρ the density of the material. One such method is the 'Laser-flash' method [85]. A thin disk-shaped sample is heated on one side with a short laser pulse and the change in temperature on the other side is detected with an infrared detector. This method is much faster than any steady-state method, however, mathematically more complicated.

The thermal conductivity of a material is strongly influenced by its microstructure. Any defects, pores or microcracks can significantly decrease the conductivity. If the material is anisotropic, the conductivity will also be anisotropic. In composites, the thermal conductivity will be between that of the phases composing it. The interface between phases also effects the conductivity. The interface itself is a barrier to heat flow. Any delaminated areas on the interface cause a significant decrease in conductivity, since the thermal conductivity of air is much lower than that of typical solids.

The variation of thermal conductivity with composition in a two phase composites can be described by a number of models. As in CTE, the Wiener model [78,79], analogous to the rule of mixtures (RoM), can be used. In equations 2.5 and 2.6, E is simply replaced with λ.

The Hashin-Strikman bounds: Using similar principles to the derivation of the bounds for elastic properties (section 2.2.1), Hashin and Strikman [86] also developed bounds for thermal and electrical properties that can be applied to thermal conductivity. The equations for the upper (U) and lower (L) bounds are:

$$\lambda_{HS-U} = \lambda_2 + \frac{f_1}{\frac{1}{\lambda_1 - \lambda_2} + \frac{f_2}{3\lambda_2}} \tag{2.23}$$

$$\lambda_{HS-L} = \lambda_1 + \frac{f_2}{\frac{1}{\lambda_2 - \lambda_1} + \frac{f_1}{3\lambda_1}} \tag{2.24}$$

where the subscript 1 and 2 represents the phases with the lower and higher thermal conductivity, respectively.

The Lichtenecker average

Lichtenecker [87] was the first to consider an interpenetrating composite geometry in the modelling of electrical and thermal properties of composites. It is based on a unit cell of a cube with one phase located at the edges of the cube, the other phase within the cube. An elegant averaging formula was derived based on slicing the microstructure into many thin slices and considering either infinite conductivity surface between two slices, or infinite resistance. These two conditions ultimately lead to a combination of mixing rules, like RoM. The general equation is:

$$K_C = K_1^{f_1} + K_2^{f_2} \tag{2.25}$$

where K stands for any material constant, subscript C for composite, subscripts 1 and 2 for the two components and f the volume fraction of the respective component. This formula is basically a generalized geometric mean. It has been shown to match many experimental results dielectric constants, the light refraction indices, thermal conductivities and electric resistivities [88].

2.2.4 Friction and wear

Wear is not a materials property, but rather a system response [89]. Until now relatively few wear studies have been published on alumina-copper composites, with only one found by the author in the literature. In that study, copper was reinforced with particulate alumina [90]. The author did not find any articles on the wear of alumina-copper interpenetrating composites, or indeed any copper-based interpenetrating composites. A similar system that has already received some attention is based on alumina-aluminium composites. Aluminium-alumina MMCs have been explored for over three decades, interpenetrating composites since the mid-1990s. One drawback of this combination is the relatively low melting point of aluminium (660 °C) limiting the possible application temperatures. Since copper has a higher melting point (1083 °C), alumina-copper composites have the potential for applications in a wider temperature range. The higher thermal conductivity of copper also allows heat generated at the wear surface to be more rapidly dispersed, thus reducing thermal mismatch stresses and the likelihood of thermal shock [91].

There are many factors influencing wear behaviour, making it difficult to compare results from different laboratories or different testing methods. Even results from a single laboratory and using the pin-on-disc dry sliding wear test have been shown to have a variation of 28 to 56 % [92]. Despite this, it is interesting to compare trends found in previous studies. Relevant results from the literature have been summarized below.

i) Alumina content: In aluminium MMCs, increasing alumina content has been found to increase wear resistance [93–95]. With fibrous alumina reinforcement this effect was only seen up to a content of 20 %, above which there was no improvement [94]. There were no studies found on the effect of the amount of alumina reinforcement in copper MMCs, but in Cu-TiB_2-TiN MMCs, the same trend as above was found [96]. Surprisingly, El-Hadek et al found the wear resistance of pure copper to be higher than that of copper-alumina MMCs with 15 % alumina, grain size 6 and 20 μm [90]. When reinforced with 100 nm alumina grains, the wear resistance of the composite was higher. The larger grains could be more easily removed from the copper matrix, thus increasing weight loss, whereas the 100 nm grains were more strongly bonded to the copper. In alumina-aluminium interpenetrating composites, increasing alumina content was also

found to increase wear resistance [97, 98]. It was also found that interpenetrating composites have a significantly higher wear resistance than MMCs [99,100]. It would be expected that the same trend be found in alumina-copper interpenetrating composites.

ii) Metal cell size and alumina grain size: Increasing metal cell size was recently found to increase wear resistance in alumina-aluminium interpenetrating composites [3,98]. It was postulated that a larger distance between thicker alumina struts provided a more effective shielding of the composite. There are conflicting results in the literature on the effect of ceramic grain size on the wear resistance of MMCs. Some studies found increasing particle size increases wear resistance in aluminium MMCs [93, 94], stating that increased particle size causes more of the load to be carried by the hard particles thus lowering the wear of the softer matrix. Others found that wear resistance increases with decreasing particle size, both in aluminium MMCs [101] and copper MMCs [3, 90, 102]. These studies postulated that larger particles are more likely to contain microcracks, therefore fracture more readily and decrease wear resistance. The effect of ceramic grain size on the wear behaviour of interpenetrating composites was not found by the author in the literature. In the wear of pure alumina, refining grain size was found to slightly increase wear resistance in the mild wear regime, and significantly delay the transition from a mild to a severe wear regime [103].

iii) Load: It is generally agreed that increasing the applied load increases the wear rate [95, 96, 98, 99, 101]. In the mild wear regime this only seems to have a small effect. However, the transition from mild to severe wear, at which point a sudden increase in wear rate of around two orders of magnitude, occurs earlier (in terms of sliding distance) with increasing load [95].

3 Production

3.1 Selection and characterisation of materials

Alumina powders

The porous ceramic preforms were made using three methods. The first method involved partially sintering a coarse alumina powder with a grain size of 5.3 μm (HVA FG, Almatis GmbH, Ludwigshafen) to give a pore channel diameter large enough to be infiltrated with copper with the available infiltration furnace (0.5 to 1 μm). The other two methods both utilised a sacrificial template. Method two involved using different starches (rice and corn) mixed into an alumina slurry with an alumina grain size of 1 μm (CT3000 SG, Almatis GmbH, Ludwigshafen). This medium sized grain was to allow for the starch granules to be adequately surrounded, such that the shape of the starch granules would be reproduced in the porous alumina. The third method used wool felt as sacrificial templates, which was infiltrated with a slurry of fine-grained alumina (0.1 μm TAIMICRON TM DAR, Taimei Chemicals, Tokyo). This was to ensure that the smallest gaps between wool fibres would be infiltrated with the slurry. The relevant product data for the three different alpha alumina powders is given in table 3.1. High purity alumina was used to ensure only solid state sintering occurred.

Sacrificial preforms

Three different starches were investigated in order to have three different pore sizes in the porous ceramics and copper cell diameters in the composites. The relevant properties of the starches are shown in table 3.2. Images of the three starches are shown in figure 3.1. Since starch is insoluble in water below 50 °C, it is suitable for use in alumina

Table 3.1: Product data of the alumina powders used.

	HVA FG	CT3000 SG	TM DAR
purity, %	99.7	99.8	$\geq$ 99.99
spec. surface area, m^2/g	0.7	3.8	14.5
avg. particle size/D50, μm	5.3	0.8	0.1
sintered density, g/cm^3	3.90	3.90	3.96

Table 3.2: Product data of the starch powders [104].

	potato	corn	rice
avg. size (μm)	33	15	5
size range (μm)	15-100	5-26	3-8
gelatinisation temp. (°C)	59-68	62-72	68-78
shape (g/cm^3)	oval, spherical	round, polygonal	polygonal

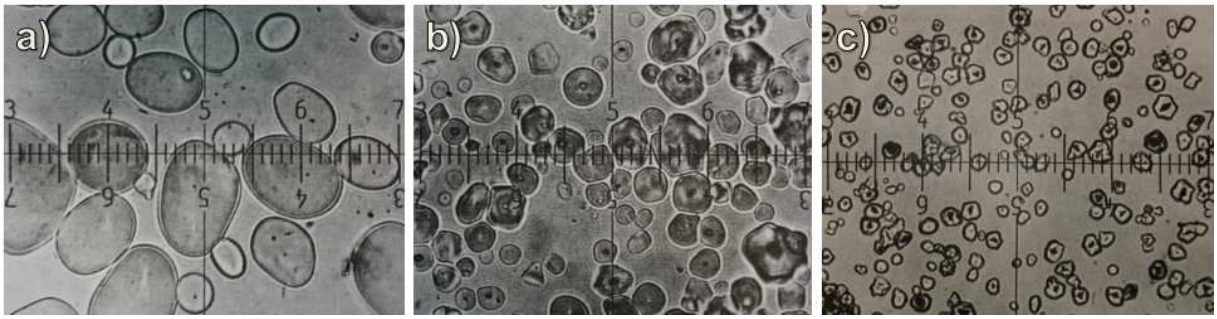

Figure 3.1: Photomicrographs of a) potato starch, b) corn starch and c) rice starch granules. The finest scale division represents 3 μm [104].

slurries. It was not possible to produce porous alumina with potato starch without drying or sintering cracks forming. For this reason only corn and rice starch were used.

Three different felts were examined (figure 3.2), however, only wool felt was chosen. Carbon felt was not dense enough (10 vol.%) and polypropylene felt had an undesirable superstructure. The scaled surface of the wool fibres was interesting in that it could potentially enhance the bonding between copper and alumina. The wool felt had a specific density of 1.32 g/cm^3 as determined via helium pycnometry (Pycnomatic ATC, Porotec, Hofheim/Taunus). It is available in a number of different relative densities, the ones chosen being 20, 30, 40 and 50 vol.%. The wool felt had an average fibre diameter of 29 μm with a range from 17 to 49 μm, determined by examination of SEM images (44 measurements taken).

In order to determine the temperature at which the sacrificial preforms would be pyrolised, thermogravimetry of the starches and wool felt was conducted (Netzsch Simultaneous Thermoanalysis STA 429, Selb/Bavaria). Figure 3.3 shows the pyrolisation curves. Based on this, pyrolisation temperatures of 650 °C for the wool felt and 550 °C for the starches were chosen.

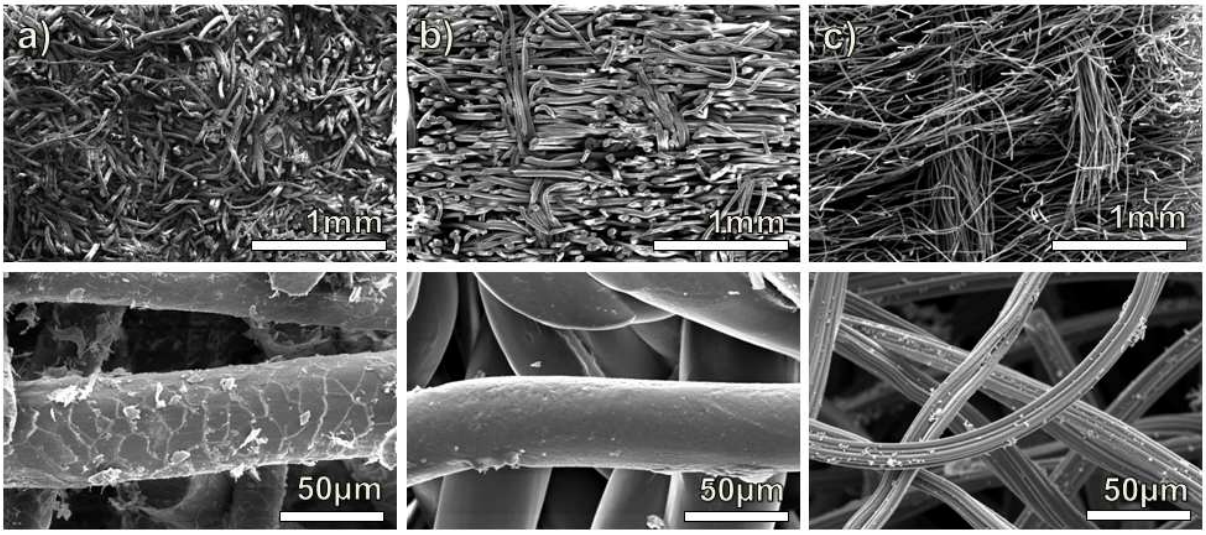

Figure 3.2: SEM images of a) wool felt, b) polypropylene felt and c) carbon felt.

Copper

A high purity copper of 99.95 % (Cu OF 2.0040, free of oxygen and phosphorous, Bikar Metalle, Bad Berleburg) was chosen as the metallic reinforcement of these interpenetrating ceramic-metal composites for a number of reasons. Firstly, a high thermal conductivity was one of the target properties. Options to fulfil this would have been copper or silver, but silver was deemed to be too expensive. The high ductility of copper (60 % elongation to break at room temperature) makes it a good candidate for providing a high fracture toughness in a composite. Although the wetting of copper on alumina is very poor (see chapter 2.1.3), no additions were made to reduce the wetting angle. This would have reduced the thermal conductivity or potentially led to a brittle interface between the copper and alumina.

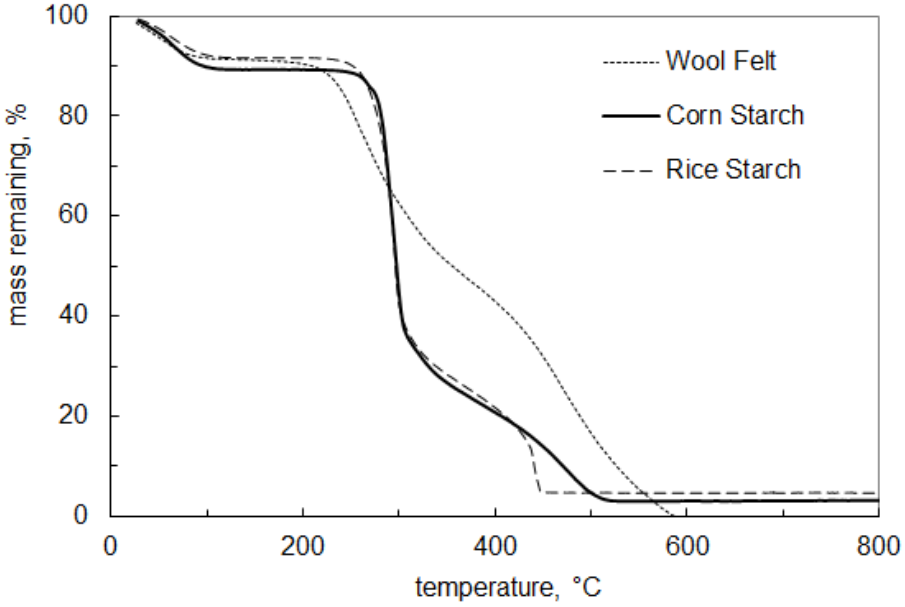

Figure 3.3: Pyrolisation curves for wool felt, corn starch and rice starch.

3.2 Porous alumina preforms

Slurry preparation

Three different alumina slurries were prepared using the recipes in table 3.3. The amount of Dolapix added corresponded to 0.8 mg/m^2 surface area of HVA FG and CT3000, 2.3 dry-wt.% of TM DAR [105] and 1 dry-wt.% of starch. The amount of Glydol used was 0.6 wt.% for all solid powders. The liquid ingredients were combined in a beaker with a magnet stirrer. The alumina powder was then slowly added to prevent clumping. The slurry was periodically treated ultrasonically (UP200S, Dr Hieschler GmbH, Stahnsdorf) to destroy agglomerates and allow a high solid content (cycle 0.5, power 100 %). If the slurry foamed, a drop or two of contraspum was added to remove the bubbles. Once the target solid content was reached, the slurry was again treated ultrasonically for 15 min, then poured through of sieve of 25 μm in order to remove any stubborn agglomerates. The slurry was then evacuated to 30 mbar for 10 min in order to remove entrapped air. All slurries were placed in jars and left for at least 24 h on rotating rollers to ensure homogeneity of the slurries, and that the glydol and dolopix had enough time to coat the particles.

i) Partially sintered: A high solid volume fraction slurry was made according to the recipe for HVA FG (Almatis) in table 3.3 in order to minimise drying time and any settling inhomogeneities.

Table 3.3: Recipes for the different alumina and starch slurries.

ingredient	mass, g HVA FG	mass, g CT3000 SG	mass, g TM DAR	mass, g Starch	function
alumina/starch	100	100	100	100	-
distilled water	24.5	24.5	72.85	100	-
Dolapix	0.064	0.6	2.3	1	deflocculant
Glydol	0.6	0.6	0.6	-	wetting agent
vol.% solids	50	50	25	40	-
mass slurry, g	125.16	125.3	175.15	201.0	-
vol. slurry, ml	49.82	49.95	100.4	167.67	-

ii) Starch-based samples: The whole amount of starch was added to the liquid ingredients at once and stirred with a rod. This method enabled the highest solid content. The CT3000 slurry and the starch slurries were combined in the ratios necessary to have the volume fraction of starch (dry) be equal to the target porosity of the porous alumina. Each mixture was left in the magnet stirrer for 10 min, then treated ultrasonically for 15 min. This was done in an ice bath to prevent the starch from becoming warm enough to swell or gelatinise. The mixtures were placed on the rotating rollers for another 24 h.

iii) Wool-based samples: A piece of wool felt the size of the mold was immersed in a large beaker with ample TM DAR slurry and evacuated to 30 mbar for 30 min to ensure that the wool felt was completely infiltrated with slurry and to minimise any residual air bubbles.

Casting and drying

The casting mould was made up of four pieces fitted together, placed on a gypsum block and sealed with a water soluble sealant for unidirectional casting. The inner dimensions of the casting mould were 70 x 70 x 20 mm^3. The mould was lined with Teflon band to prevent sticking and cracking during drying, as well as aid demoulding. Before casting a small amount of distilled water was poured into the mould to moisten the gypsum block to aid removal of the liquid from the slurry. The slurries (and infiltrated felt in the case of the wool based samples) were cast into the mould. The mould and block were then placed in an evacuation chamber and evacuated to 30 mbar in order to remove any air bubbles entrapped in the slurry.

The moulds were covered and placed in a box with a dish of water to ensure that drying would not occur too quickly or unevenly on the surface in the critical drying phase, and

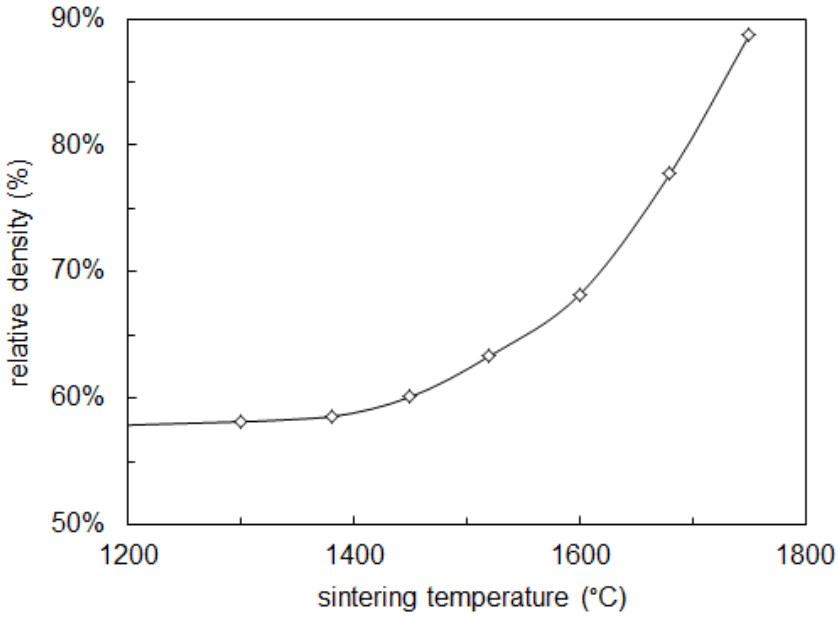

Figure 3.4: Sintering curve for HVA FG.

to minimise the danger of shrinkage cracks. After 48 h (when the green body could be easily shifted off the gypsum block) the green bodies were removed from the moulds, placed on a sponge block with large pores and left to dry in air until no weight loss was measured. The samples were then placed in a drying oven (Memmert Model 400, Schwabach) at 40, 55, 70 then 85 °C for 4 h at each step. The oven ventilation was turned off to avoid a high gradient in water vapour partial pressure. Finally, the green bodies were left for at least 24 h at 95 °C. The bottom side of the samples were sanded with SiC sandpaper of 80 and 320 grit to remove any remainders of the gypsum block. Even very small amounts of SiO_2 or CaO could cause abnormal grain growth during the sintering of alumina [106]. The samples were then transferred to a desiccator until further use.

Pyrolisation and sintering

For the partially sintered samples, a sintering curve for HVA FG was first made by sintering small samples at different temperatures, measuring the resulting porosity via the Archimedes principle (see section 4.1.1), and plotting porosity against sintering temperature (figure 3.4). The sintering temperatures required for the different target porosities were then interpolated from the curve (table 3.4). The sintering temperatures used for CT3000 and TM DAR were 1550 and 1350 °C, respectively [107]. For the wool and starch-based samples, the sacrificial preform was first burnt out in a furnace (Nabertherm HT 16/17, Flörsheim am Main) inside a fume hood. Since this furnace was limited to 1100 °C the pyrolisation and sintering steps had to be conducted

Table 3.4: Sintering temperatures interpolated from the sintering curve for HVA FG to achieve target porosities.

porosity, vol.%	20	25	30	35	40
sintering temperature, °C	1695	1660	1620	1550	1450

separately. The samples were heated quickly to 100 °C, then very slowly (0.5 K/min) up to 550 °C for the starch based samples and 650 °C for the wool based samples and held at that temperature for 12 hours to allow complete pyrolisation of the sacrificial preforms (fractography of preliminary samples revealed carbon flakes sometimes being the fracture source prompting a longer burnout time). The samples were then heated at 10 K/min up to 1100 °C and presintered in order to make them stable enough to be carried to the sintering furnace. For the sintering step, all samples were heated at 10 K/min, held at the relevant sintering temperature for 2 h, then cooled at 10 K/min to room temperature.

3.3 Copper infiltration

a) Materials preparation: The sintered porous alumina samples were infiltrated with distilled water to avoid contamination and cut according to figure 3.5 to enable them to be hung above the crucible, inserted and removed from the copper melt. After cutting, the samples were cleaned with fresh distilled water in an ultrasonic bath and dried. The density and weight of the porous alumina samples were also measured at this point to enable the amount of copper and residual porosity in the composites to be determined. A high purity copper of 99.95 % was used (Cu OF 2.0040, free of oxygen and phosphorous, Bikar Metalle, Bad Berleburg). A large sheet of copper with a thickness of 5 mm was

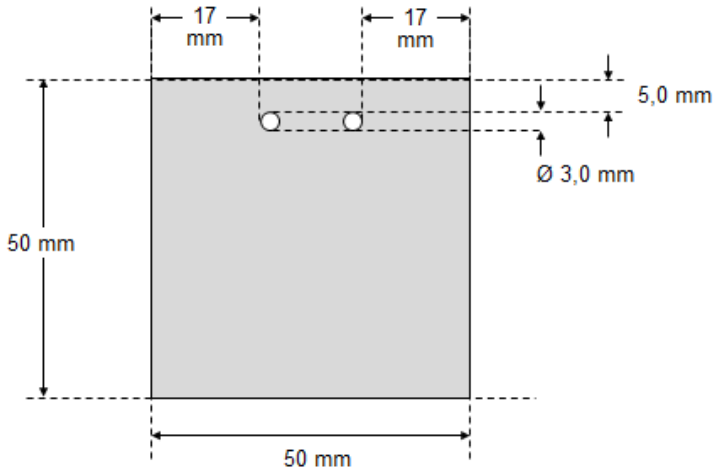

Figure 3.5: Sample dimensions for porous alumina to be infiltrated with copper.

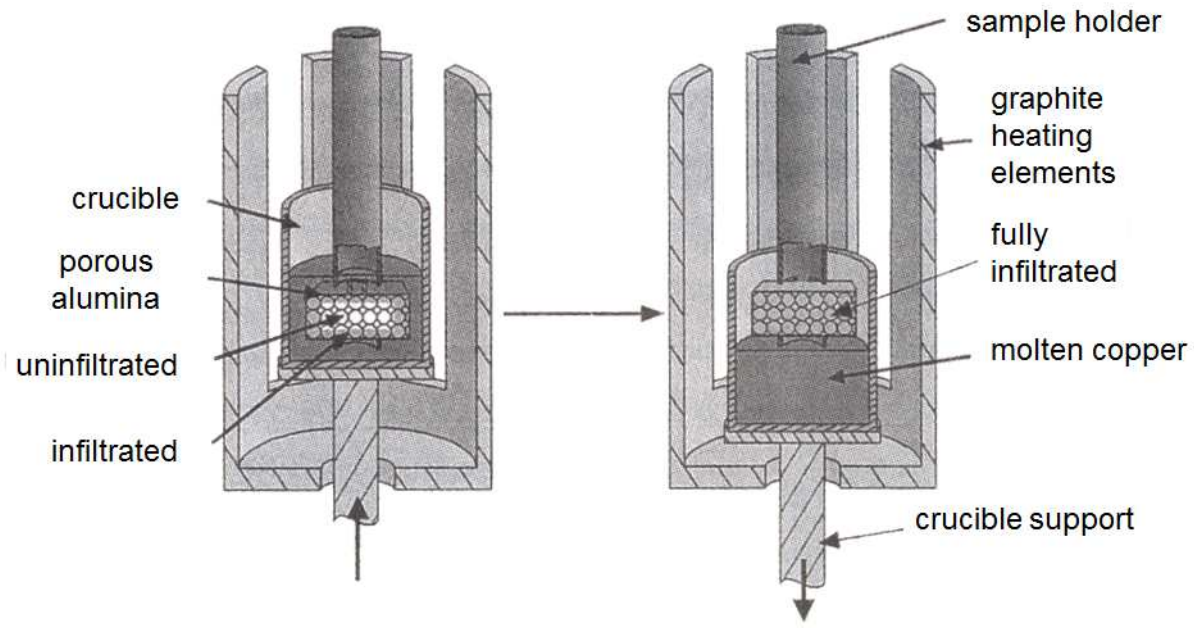

Figure 3.6: Schematic diagram of gas pressure metal infiltration furnace [32].

cut up into smaller pieces to allow an alumina crucible (Morgan Technical Ceramics, Haldenwanger) to be filled with an appropriate amount of copper before infiltration. The amount needed to fully infiltrate the sample as well as cover all the samples during and just after infiltration was calculated based on the volume and porosity of the samples to be infiltrated. The copper pieces were cleaned in acetone in an ultrasonic bath and dried before placing in the crucible. The samples to be infiltrated were hung in the sample holder and rested on the copper in the crucible to be transferred to the infiltration furnace.

b) Infiltration: A gas pressure infiltration furnace enabling operation under vacuum as low as 1×10^{-3} mbar or high pressure up to 10 MPa was used (Type FPW 125/180-2200-100-SP-AS, Fine Ceramics Technology, Rödenthal). The furnace is heated with graphite elements and cooled with a cooling water circuit. The support for the crucible has a hydraulic press for adjusting the height. A schematic diagram of the infiltration furnace is shown in figure 3.6. The alumina crucible with copper pieces was placed in the graphite crucible on the crucible support of the furnace. The sample holder and samples were screwed into the lid of the furnace chamber, the support lowered and the lid put into place. The furnace was closed and evacuated overnight, such that a vacuum of approximately 3×10^{-3} mbar was reached. Processing parameters are shown in table 3.5. The samples were weighed before and after infiltration in order to determine how much copper infiltrated the sample and whether it had been fully infiltrated.

Table 3.5: Process parameters of copper infiltration.

Set temperature, °C	dT/dt, °/min	$\mathbf{time_{hold}}$, h:mm	Parameter
20		0:02	vacuum off, p_{Ar} = 2 bar
300	10	0:30	vacuum on
1200	15	0:60	
1200	0	0:10	raise crucible
1200	0	0:10	vacuum off, p_{Ar} = 100 bar
1200	0	2:00	p_{Ar} = 100 bar
1050	10	0:00	lower crucible
800	10	0:00	
400	10	0:00	p_{Ar} = 30 bar
20	4	0:00	p_{Ar} = 0 bar

3.4 Processing issues and optimisation

The composites were produced over a period of two years. There were a number of difficulties encountered, some of which were overcome and others which were not. The results of fractographic analysis (chapters 5.2.3 and 6.2.3) also led to changes in the method of production to improve the resulting microstructure of the composites.

The porous alumina preforms

The main difficulty faced in the production of the alumina preforms was the formation of shrinkage cracks. Shrinkage cracks often occurred during either drying, pyrolisation or sintering, despite having a very slow and careful drying program in comparison to others [108–110]. In the partially sintered and starch-based samples, this was partially overcome by making the samples thinner, but a thickness of at least 4 mm was required to be able to produce bend bars or CT samples with a final thickness of 3 mm. The thickness of the wool felt (5 to 10 mm with the thinnest felt for the highest density) dictated the thickness of the wool-based samples.

Shrinkage cracks were worst in the partially sintered samples: they often cracked into two pieces through the middle during sintering. Casting the samples thinner only partially improved this problem. Slower drying also did not improve this. It was necessary to cast many more samples than needed to produce enough uncracked samples.

The potato starch based samples always cracked during drying and were therefore eliminated from the sample range. This was despite wanting to be able to compare the properties of composites with 30 μm copper spheres with 30 μm copper fibres. It was intended to investigate whether the diameter of the sphere/fibre or the diameter of the pore window is more critical in affecting the mechanical and thermal properties. This was unfortunately not possible. The relatively large potato starch particles (30 μm) swelled in water and upon drying would have shrunk significantly. A strong adhesion to the alumina particles would have caused some to pull into the middle of the pore (also discussed in section 6.1.1), thus potentially weakening the green body. This would have also been the case with the rice and corn starches, but with a less detrimental effect due to the smaller particles size of these starches (5 and 15 μm, respectively).

During the infiltration of wool felt with slurry, a long evacuation time (approximately 1 h) was needed to remove air entrained between the fibres. If the evacuation time was not long enough, there were regions of the wool felt that were not fully infiltrated with slurry. This led to extensive shrinkage and deformation during pyrolisation and sintering. Wool based samples often curved upwards slightly after sintering, indicating that the porosity was not uniform throughout the sample. This may have been due to a density gradient across the wool felt sacrificial preform. Also, after infiltration there was a layer of alumina above and below the felt which was ground away with sandpaper. If this was not ground away sufficiently, or not evenly enough, there would be a more dense layer either above or below with a different shrinkage behaviour during sintering. The other samples did not curve after sintering, indicating that the porosity was homogeneous throughout the porous ceramic preform.

Fractographic analysis revealed the presence of abnormally large alumina grains, copper regions and carbon flakes in starch-based samples. Although the reason for the large alumina grains was not clear, the slurries were milled to destroy any stubborn agglomerates. The slurries were also poured through a fine sieve to remove any impurities or remaining large particles. To avoid large copper regions the slurries were evacuated for longer, before and after casting. Carbon flakes in the starch-based samples were avoided by increasing the pyrolisation holding time from 2 to 12 h.

Copper infiltration

Approximately 1 out of 5 times, the copper infiltration did not work, despite all conditions being the same. The samples were simply not infiltrated. It is possible that there was not enough copper in the crucible. If the samples were not fully submersed in copper when the vacuum was switched off and 100 bar of pressure applied, the argon would have filled the pores and prevented copper from infiltrating. Alternatively, there

may not have been enough copper covering the samples, so that even if they were submersed, the layer of copper covering the samples may have been swept aside by the argon entering the furnace, long enough for argon to fill the pores.

The partially sintered samples were difficult to infiltrate fully. There was often a porous layer remaining in the middle the sample. Either the pressure was not high enough, or the infiltration time not long enough. Since it was not possible to increase the pressure, the copper infiltration time was increased from 1.5 to 2 h.

Starch-based samples with more than 25 % porosity were mostly well infiltrated, but there were some exceptions. For example, one batch of samples with 50 % porosity had a residual porosity of 5 % after infiltration, despite all other known conditions being identical. Since the cause for this was unknown, it was not possible to change any parameters to avoid it.

The wool-based samples were also difficult to infiltrate fully, but for a different reason. Inside the sample was generally fully infiltrated, however, on the surface there was a thick uninfiltrated layer, where copper had flown back out of the sample after removing from the melt. It was necessary to grind away approximately 0.5 to 1 mm of the surface to remove this porous layer. This was not an issue with the starch based samples, where the lower permeability of the porous ceramic preform helped to retain the copper after removal from the melt. The finer pore structure of the partially sintered sample retained the copper better due to capillary forces. Generally less than 100 μm had to be ground away from the surface of these samples.

Many of the problems faced with copper infiltration could potentially be overcome by using the squeeze casting method. The higher pressures ensure complete infiltration. In addition the cycle time is much quicker - minutes as opposed to 24 hours - making it more viable for industry.

3.5 Sample nomenclature

Based on the sacrificial preform used and the shape of pore (and hence copper region) it produced, the copper ligament diameter and the volume fraction of copper, the following sample nomenclature will be used from this points onwards:

1p	=	**p**artially sintered HVA FG, copper ligament diameter 1μm
5s	=	copper **s**pheres, avg. diameter 5 μm(rice starch)
15s	=	copper **s**pheres, avg. diameter 15 μm(corn starch)
30f	=	copper **f**ibres, avg. diameter 30 μm(wool felt)
x	=	avg. volume per cent copper for the sample(s) tested

For example, sample 5s-20 had a rice starch sacrificial preform, has copper spheres with a diameter of 5 μm and contains 20 vol.% copper.

4 Characterisation

4.1 Microstructure and composition

4.1.1 Porous alumina preforms

Porosity

The porosity of the samples was determined using the Archimedes principle. This principle describes that the bouyancy force acting upwards on a solid object in a liquid is equal to the weight of the fluid displaced by the object. The samples were infiltrated with distilled water by submerging them in a beaker of water, placing the beaker in sealed container and evacuating to 30 mbar until no more air bubbles left the sample. This typically required at least 30 min. The bulk density of the samples could then be determined according to the following formula:

$$\rho_{arch.} = \frac{m_{dry}}{m_{sat} - m_{susp}} \cdot \rho_{aq}, \tag{4.1}$$

where m_{dry} is the weight of the dry sample in air, m_{sat} is the weight of the infiltrated sample in air, m_{susp} is the weight of the infiltrated sample suspended in water and ρ_{aq} is the density of water. The relevant weights were measured with high accuracy scales (Sartorius BA 110 S, Göttingen). The temperature of the water at the time of measuring was also recorded and the density of water for that specific temperature read from a chart.

This method also allows the open porosity of the sample, i.e. that which can be infiltrated with water, to be determined. The porosity can be calculated from the ratio of the Archimedes density to the theoretical density:

$$P_{\text{open}} = 1 - \frac{\rho_{arch.}}{\rho_{theo.}} \tag{4.2}$$

Pore size

Small samples of the porous ceramics were ground flat with a 15 μm diamond wheel on a grinding machine (Ziersch und Baltrusch, Reutlingen), then polished with diamond

paste on a polishing cloth in an automatic polishing machine (Phoenix 400, Jean Wirtz. Düsseldorf) in four stages: 15, 6, 3 and 1 μm, using diamond paste (DP-Paste, Stuers, Düsseldorf). These were then inspected in an SEM (Philips FEG-XL30, Netherlands) and pictures taken. The program Lince 2.4.3e (S. L. dos Santo e Lucato, "Lince v2.4-Linear Intercept," Department of Materials Science (1999))was used to determine the average pore size. A mercury porosimeter (Micrometrics Poresizer 9320, Narcross, USA) was used to determine the average pore channel diameter. However, since this is limited by the smallest diameter, this method actually determined the size of the pore channels in the partially sintered samples and the size of the bottle necks between pores in the starch based samples.

4.1.2 Composites

The composites were ground and polished in the same manner as the porous ceramics. Due the softness of the copper and hardness of the alumina phase, it was difficult to obtain a good polishing finish. The exact polishing parameters are therefore given in table 4.1. A plate speed of 150 rpm with a head speed of 150 rpm in the opposite direction was used. Diamond paste was reapplied every 5 min.

Table 4.1: Polishing parameters for the composites.

stage, μm	cloth	pressure, bar	time, min	target condition
15	MD-Allegro	1.3	5	grinding marks removed
15	DP Plan	1.4	20	no scratches in alumina, rough
6	DP Plan	1.6	30	alumina white, not rough
3	DP Plan	1.4	20	no scratches in copper
1	DP Nap	1.4	10	

Microstructure

The samples were examined in the optical and electron microscopes. SEM images were analysed with the program Lince in order to estimate copper ligament diameter. The copper ligament diameter refers to the width of the copper channels in the partially sintered samples, the diameter of the copper spheres in the starch based samples and the diameter of the copper fibres in the wool based samples.

Two cylindrical samples of M30 and W30, diameter 2 mm, height 4 mm, were analysed with X-ray computer tomography (v tome x c, 240 kV Microfocus-X-ray Tube Focus 4 to 200 μm, Resolution $\geq$5 μm, Flat panel detector, GE Sensing and Inspection Technologies, Wunstorf, Germany) at the Österreichisches Gießerei-Institut (Austrian Casting Institute)

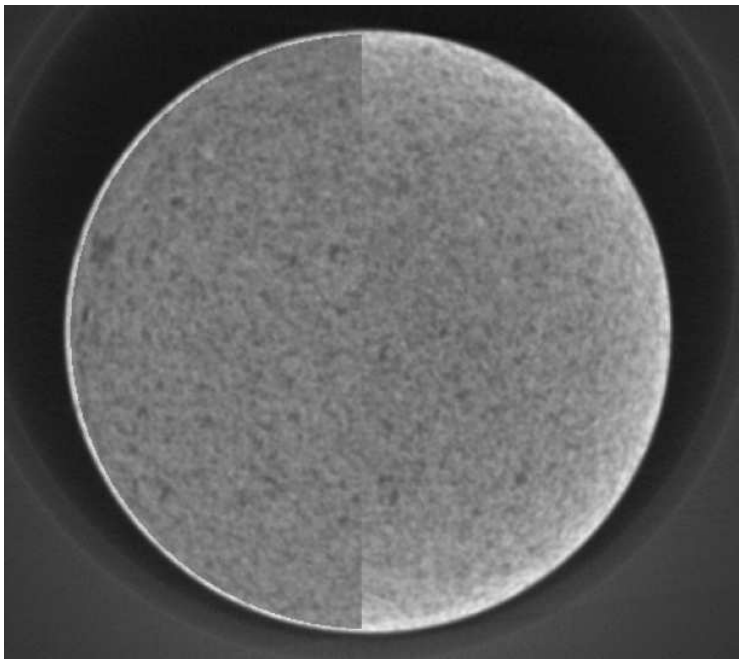

Figure 4.1: Before and after normalisation of the intensity with the left half of the corrected image superimposed on the original one [113].

in Leoben, Austria. Since the resolution of the machine was 4.85 μm, the partially sintered samples or rice starch based samples with copper ligament diameters of 1 μm and 5 μm, respectively, were not measured.

The raw data obtained was organised in Matlab [111] into a 3D matrix with intensity values sorted by coordinates. The resolution of the scan is the distance between two points, which for the samples scanned was 4.85 μm. Structural defects due to processing were cropped out and ignored. Scanning artefacts included noise and non-uniform intensity. The noise around the sample was constant and was assumed to also be constant within the sample. The noise was considered to have no impact on the morphology and was ignored. Due to a so-called 'beam hardening' effect [112] caused by thickness dependent absorption of the polychromatic beam, the centre of the sample appeared to be darker than the edge. This symmetrical variation in intensity over the cross-section of the cylinder was measured and normalised to give an image of uniform intensity. An example of what an image looked like before and after this normalisation is shown in figure 4.1. To separate the two phases, an appropriate threshold value in the continuous grey scale must be chosen, which was done using a built-in function in Matlab ('greythresh'). This function chooses the threshold that *"minimises the intraclass variance of the black and white pixels"* [111]. The resulting binarised image (figure 5.3 in the results chapter) was translated to a finite element model, with one voxel (volume element, analog to pixel: picture element) corresponding to one finite element.

Residual porosity

The amount of open porosity could be determined via the Archimedes principle as for porous alumina. The amount of closed porosity was then estimated by assuming the average alumina content from the porous alumina Archimedes density results. A theoretical density (TD) was calculated assuming no porosity according to 4.3:

$$TD = V_{Al_2O_3}\rho_{Al_2O_3} + \left(1 - V_{Al_2O_3}\right)\rho_{Cu} \tag{4.3}$$

The apparent specific gravity (ASG) was calculated from the Archimedes measurement and compared with TD to calculate the closed porosity. Any difference in the densities was due to a lack of infiltrated copper, which could be calculated and converted to a value for vol.% closed porosity (CP) according to equation 4.4:

$$CP = \frac{TD - ASG}{\rho_{Cu}.100\%} \tag{4.4}$$

4.2 Mechanical properties

4.2.1 Young's modulus

Experimental

The Young's modulus of each of the composites was measured on bend bars with an approximate cross-section of 3x4 mm^2 and at least 25 mm long with the impulse excitation technique according to ASTM-E1876-99 [114]. The resonance frequencies were detected by the Grindosonic (MK5 Industrial, J.W. Lemmens N.V., Leuven, Belgium). The average value was used to calculate the Young's modulus at room temperature using equations (4.5) and (4.6). A minimum of ten bend bars were measured for each composition.

$$E = 0.9465\frac{m{f_f}^2L^3}{bt^3}T_1 = 0.9465\frac{\rho{f_f}^2L^4}{t^2}T_1 \tag{4.5}$$

$$\begin{aligned} T_1 =& 1 + 6.585(1 + 0.0752\nu + 0.8109\nu^2)\left(\frac{t}{L}\right)^2 - 0.868\left(\frac{t}{L}\right)^4 \\ &- \left(\frac{8.340(1 + 0.2023\nu + 2.173\nu^2)\left(\frac{t}{L}\right)^4}{1 + 6.338(1 + 0.1408\nu + 1.536\nu^2)\left(\frac{t}{L}\right)^2}\right) \end{aligned} \tag{4.6}$$

Finite element modelling

The modelling was conducted by V. Salit from Festkörpermechanik (solid state mechanics), TU Darmstadt and will only be described briefly here. The X-ray CT data had a size of 800 × 800 × 512 voxels , making it impossible to analyse a whole sample at once on an average computer. It was therefore necessary to partition the sample into subvolumes and calculate the average result of all the subvolumes. A subvolume size of 50^3 was found to give an appropriate approximation of Young's modulus, with a further decrease in subvolume size reducing the accuracy of the approximation.

Using FEAP, linear elastic material properties were assigned to the two phases and the boundary conditions were defined (displacement controlled loading). In the general, 3D case, six homogeneous loading cases would be required to calculate the full stiffness tensor: three tensile and three shear. Since only the Young's modulus, E, was sufficient to compare with the existing experimental results, a simple tensile load case was applied. Once the displacement d was applied, the resulting average strain, ε, could be calculated as $\varepsilon = \frac{d}{L}$ where L is the edge length. The average stress is the resulting reaction force, F, divided by the sample face area, A, that is, $\sigma = \frac{F}{A}$. Finally E was calculated according to the one dimensional Hooke's law: $E = \frac{\sigma}{\varepsilon}$

4.2.2 Hardness

Hardness was tested with a Vickers indenter (HPO 250, Fabr. 308/64 VEB Werkstoffprüfmaschinen Leipzig) at the Institure for Materials Research, Slovak Academy of Sciences in Kosice, Slovakia (IMR-SAS). It was tested under a load of 98 N for 10 s. This was to ensure that the indentation covered an area representative of the composite, particularly the wool based composites with the largest copper ligament diameter. Ten indentations were made on each sample and lengths of the diagonals of each indentation (d_1 and d_2, average value d in mm) indentation used to calculate hardness, HV(GPa) according to equation 4.7:

$$HV = 1.8544\frac{F}{1000d^2} \tag{4.7}$$

4.2.3 Bending strength and fractography

At IMR-SAS the bending strength of a selection of samples was tested under four point loading (similar to figure 4.2) with an inner span, S_2, of 10 mm and an outer span, S_1, of 20 mm (Material Testing System model LR5K Plus, Lloyd Instruments Limited, England). Sample dimensions of approximately B=4 mm, W=3 mm were used. The crosshead

rate was 0.5 mm/min. Using the load at failure, F, the bending strength was calculated according to equation 4.8:

$$\sigma_b = \frac{3F(S_1 - S_2)}{2BW^2} \tag{4.8}$$

Fractographic analysis of the fracture surfaces was carried out to locate and identify the flaws where fracture originated. This was first carried out in a stereo optical microscope (Nikon SMZ-2T, Japan) to determine the location of the flaw. The fracture-causing flaws were then analysed in an SEM (JSM-7000F, JEOL Ltd, Japan) to determine what they were. Where necessary, EDS composition analysis was conducted.

4.2.4 Fracture toughness

Two different sorts of samples were used to measure the R-curve behaviour of the composites: single edge V notched beam (SEVNB) bending bars and compact tension (CT) samples. For each type, the samples were cut to the required dimensions, shown schematically in figures 4.2 and 4.3, and polished as described above to a finish of 1 μm on one of the faces as shown in the aforementioned figures.

Single edge V notched beam (SEVNB)

The R-curves of a selection of compositions were initially measured using SEVNB bend bars in a four-point bending apparatus (ARCO-4PB, TU Darmstadt). The sample geometry and loading arrangement is shown in figure 4.2. A notch approximately 900 μm deep was cut with a diamond saw, with the last 100 μm cut with a razor blade with a thickness of 0.3 mm and a suspension of 3 μm diamond particles in silicon oil. In order to achieve a sharp notch tip the blade was changed shortly before the target notch depth was reached. A notch radius of around 20 μm could be achieved. The inner span (S_2) was 10 mm and the outer span (S_1) 20 mm. The sample dimensions were approximately B=3 mm, W=4 mm and sample length $\geq$25 mm, although this varied from sample to sample.

The load was applied with a piezo actuator across a load cell and could be adjusted by hand. The sample was placed in the apparatus such that the notch was exactly in the middle of and parallel to the loading spans and a small preload applied. The testing apparatus was then placed in an optical microscope (Leica 301-371.011, Wetzlar). Crack initiation and propagation was observed under careful manual control of the applied load. After each crack growth increment of 30 to 100 μm the load was reduced by

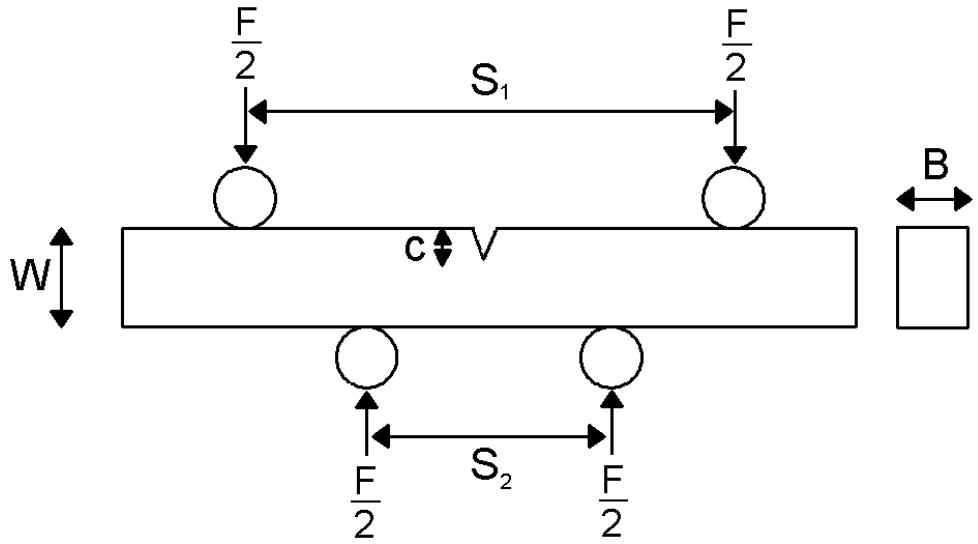

Figure 4.2: Loading arrangement and dimensions of the four-point-bend sample.

around 20 % and the maximum load and crack length before propagation recorded. The value of K for each data point was calculated with the following formulas [115]:

$$K_{app} = \sigma Y \sqrt{c} = \frac{F}{B\sqrt{W}} \cdot \frac{S_1 - S_2}{W} \cdot \frac{3 \cdot \sqrt{\frac{c}{W}}}{2\left(1 - \frac{c}{W}\right)^{\frac{3}{2}}} \cdot f_1\left(\frac{c}{W}\right) \tag{4.9}$$

$$f_1\left(\frac{c}{W}\right) = 1.9887 - \left(\frac{c}{W}\right) \cdot \left(1.1326 - \frac{\left(3.49 - 0.68\left(\frac{c}{W}\right) + 1.35\left(\frac{c}{W}\right)^2\right) \cdot \left(1 - \frac{c}{W}\right)}{\left(1 + \frac{c}{W}\right)^2}\right) \tag{4.10}$$

Compact tension (CT)

Since for most samples tested no plateau in the R-curve was achieved, the R-curves were then measured with CT samples (figure 4.3) such that the crack tip was under tensile stress (ARCO-CT, TU Darmstadt). The outer sample dimensions (HxL) were approximately 33x35 mm^2 and the dimension W 28 mm. The sample thickness (B) varied from 2 to 3 mm. Although the standard thickness is 3 mm, some samples only had a fully infiltrated region of 2 mm thickness. All sample dimensions were remeasured in the optical microscope. A cut was made with a diamond wire saw into the notch, diagonally under the polished surface, at an angle of around 25°. A Knoop indentation was then applied 100 μm from the end of the cut on the polished surface with a load large enough to produce a crack through the thickness of the sample between the cut and the polished surface [67]. The sample was placed in the setup under the optical microscope and a load carefully applied until the crack grew at least 200 μm into the region of constant sample thickness. The sample was then removed and the notch extended with

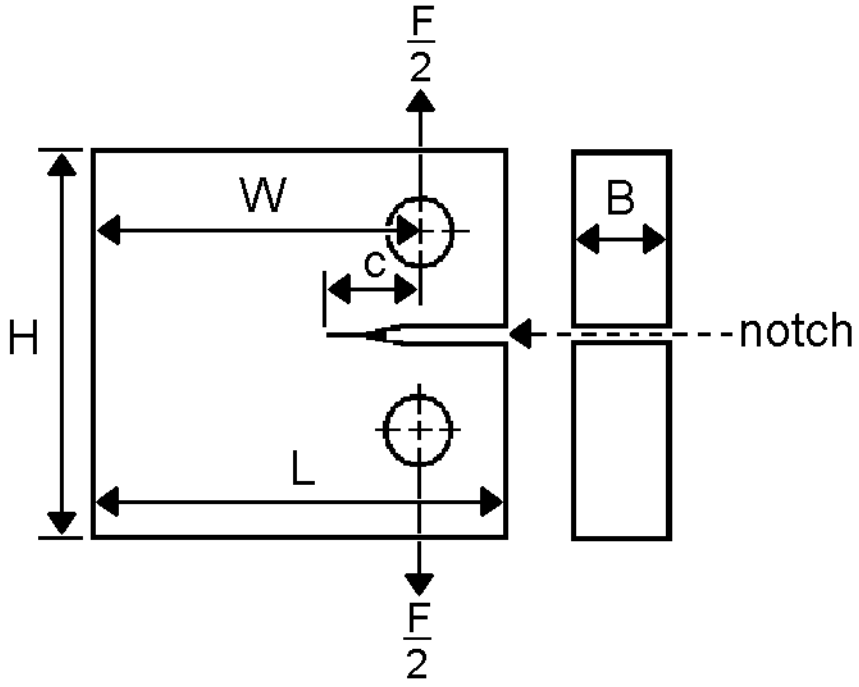

Figure 4.3: Loading arrangement and dimensions of the compact tension sample.

the diamond wire saw such that diagonal cut and indentation, but not the precrack, were removed, with a precrack of length 100 to 200 μm remaining. The crack length from the axis of loading was designated c.

The application of load and measurement of load and crack length was conducted similarly to the SEVNB method. The load of crack propagation and corresponding crack length could be recorded automatically and converted to K with equations 4.11 and 4.12 using a Labview software program. The test was conducted until a plateau in the R-curve was reached. The crack was then cut away such that only 100 to 200 μm was remaining using the diamond wire saw. A new R-curve could then be measured in the same sample. This was repeated until $a/W \geq 0.8$. In this way 2 to 4 R-curves could be measured in each CT sample in order to ensure the reproducibility of the results.

$$K = \frac{F}{B\sqrt{W}} \cdot f_2\left(\frac{c}{W}\right) \tag{4.11}$$

$$f_2\left(\frac{c}{W}\right) = \frac{\left(2+\frac{c}{W}\right)\left(0.886+4.64\left(\frac{c}{W}\right)-13.32\left(\frac{c}{W}\right)^2+14.72\left(\frac{c}{W}\right)^3-5.6\left(\frac{c}{W}\right)^4\right)}{\left(1-\frac{c}{W}\right)^{\frac{3}{2}}} \tag{4.12}$$

Crack opening displacement (COD)

A drawback of the above method for determining the R-curve is that the crack tip toughness K_{IO} cannot be determined, since it is impossible to have a starting crack length

equal to zero. Measuring the crack opening profile near the crack tip allows K_{IO} to be estimated. After the last R-curve measurement the samples M30, M40, M60 and H40 were sputtered with a thin layer of carbon (≈20nm). The sample was placed in the CT loading equipment with a small preload and placed in the SEM. The door of the SEM had connections allowing load to be applied to the sample and measured. After evacuating the chamber the crack tip in the sample was located and the load increased until the crack grew a short distance, approimately 20 μm. This load was called the critical load. The critical load was not taken from the last R-curve measurement because the load under vacuum varied significantly from the load measured in air. This was assumed to be due to the load cell behaving differently under vacuum, and not the atmosphere affecting the crack growth behviour in the sample. The value of K at the critical load was taken from the R-curve measurements. In order to avoid further crack growth, a load less than the critical load was used to measure the crack opening profile [74, 116].

The total crack length was remeasured and the crack tip relocated. Starting at the crack tip, loads of approximately 80 and 95 % of the critical load were applied alternatively and the crack opening under these two loads measured as a function of distance from the crack tip. This was in order to be able to extrapolate to the crack opening at 100 % of the critical load. This was continued until at least 3 data points were within the unbridged region of the crack. The unbridged region of the crack was identified both visually and by checking that the crack profile fit the Irwin parabola (equation 2.16 replacing K_{IO} with K_A). The total crack length varied from 2 to 3 mm. At the crack tip a magnification of 35,000x was used with data points around 3 to 5 μm apart. As the distance from the crack tip increased the magnification used was gradually decreased to 10,000x and distance between data points gradually increased to 150 μm in order to be able to measure the whole crack profile within one day. The crack tip toughness K_{IO} was calculated by fitting equation 2.16 to the first 100 μm of the crack profile. The microstructural shielding term, $K_\mu(\Delta c)$, was calculated by subtracting K_{IO} from the measured R-curves.

4.3 Thermal properties

4.3.1 Thermal expansion

The thermal expansion behaviour of a selection of composites was investigated with a dilatometer (Netzsch DIL 402 E7, Selb). In order to calibrate the machine and enable the strain due to the machine itself to be separated from the strain of the sample, a correction measurement was carried out with a sapphire rod aligned in the [0001] crystallographic direction. The sapphire rod was remeasured and compared with the standard expansion curve for this material to check the reliability of the calibration method as well as the accuracy of temperature measurement. After evacuating the chamber and flushing with argon twice, then establishing a steady flow of argon (to avoid oxidation of copper), the samples were heated at 3 K/min up to 800 °C, held for 1 h, then cooled at 3 K/min down to room temperature[1]. An extra holding time of 2 h was added at the end in order to capture the whole cooling curve, since the cooling rate of the sample was exponential. The length of the sample was measured continuously throughout the heating cycle. Strain was plotted as a function of temperature. The incremental coefficient of thermal expansion (CTE) was also plotted as a function of temperature. The average linear CTE was calculated across the whole temperature and strain range, as well as heating from room temperature to 200 °C.

4.3.2 Thermal conductivity

Steady-state

Bend bars (approx 3 x 4 x 25 mm^3) of each sample were placed upright in an apparatus for measuring thermal conductivity. Cotton wool was placed around the sample to minimize heat loss from the free faces to the surroundings. Each end of the sample was in contact with a copper plate, using a small amount of conductivity paste and a spring mechanism behind the plates to ensure a good contact and thermal transfer between the copper plates and the sample. The lower copper plate was heated electrically using a 120 Ω resistor. The upper copper plate was kept at a constant temperature with water cooling. The heat flow was determined by measuring the drop in voltage across the resistor with a voltmeter. The temperatures of the upper and lower ends of the sample were measured with two thermoelements. The voltage supplied to the resistor was adjusted twice for each sample, such that there were temperature differences of

[1] In the dissertation by Skirl [52] it was found that reducing the heating rate from 5K/min down to 0.5K/min had only a very small effect on the strain curves, with a slightly lower total strain and the same shape curve shifted to slightly lower temperatures. Therefore, 3 K/min was deemed to be a suitable heating and cooling rate.

approximately 5 and 10 K, respectively. It was necessary to wait a few minutes for the temperature difference across the sample to reach a steady state. The thermal conductivity of each sample could thus be calculated according to equation 2.20.

Transient

The thermal diffusivity, a, of a selection of composites was measured at ZAE in Würzburg using the Laser Flash method according to ASTM E 1461-07 [85]. The samples were prepared by drilling cylinders 9 mm in diameter out of plates of the composites which were then ground to a thickness of 1.5 mm, taking care that the surfaces were parallel. The samples were coated on the front and back with a thin layer of graphite. The front of the sample was heated with a Nd-YAG-Laser (λ=1.064 μm) for 0.3 ms at room temperature. The temperature of the back of the sample was recorded with an infrared sensitive MCT-detector and plotted as a function of time. At least five measurements were made for each sample and the average curve calculated. The thermal diffusivity was extracted from an analysis of the curve. In the analysis a theoretical solution suitable for the experiment was fitted to the average curve (the theoretical solution was not supplied by ZAE). The theoretical solution took into account heat loss and the finite duration of the laser pulse. By assuming the value of the thermal capacity, C_p, of the samples obeyed the rule of mixtures, the thermal conductivity, λ (W/mK), was then calculated according to equation 2.22

4.4 Wear behaviour

Wear testing was carried out using the pin-on-disc method [117]. In order to reduce chemical reactions and the complexities associated with tribochemical behaviour, an alumina ball (diameter 5 mm, hardness 1700 HV, grade 25) was used on a composite disc. Samples were cleaned in acetone and thoroughly dried before testing. Preliminary tests were carried out on sample 15s-20 in order to determine the parameters required to achieve a steady state wear, have a measurable mass loss, but avoid severe or excessive wear. This would enable the samples to be reused for further testing. During preliminary tests, steady state wear appeared to be achieved after a distance of 100 m, so a wear distance of 300 m was deemed sufficient.

As per ATSM G99, each test was carried out for the complete sliding distance, not stopped and started, so as to avoid alignment problems. Under a load of 20 N there was less noise in the torque measurements than under lower loads. A speed of 0.2 m/s and wear track diameter of 10 mm was used. Tests were repeated 3 times per sample. Samples with around 20 % copper were also tested under a load of 10 N. During the wear test torque and temperature were measured, with the torque converted to a friction coefficient automatically during the test. The temperature of the alumina ball was measured with a contact thermocouple. With the equipment available, the temperature of the wear surface could not be measured.

The average specific wear factor was determined by the mass loss during the test, converted to volume loss from the measured density of the sample, and confirmed by measuring the volume loss via 3D profilometry using a white light microscope (Confocal White Light Microscope μ Surf, Nanofocus, Oberhausen, Germany). The specific wear factor (mm^3/Nm) was calculated by dividing the total volume lost (mm^3) by the applied load (N) and wear distance (m). To determine the wear mechanisms involved, the wear tracks were investigated in a scanning electron microscope (SEM, Model No. XL 30 FEG, Philips Electronic Instruments, Mahwah, NJ).

5 Results

5.1 Microstructure and composition

5.1.1 Porous alumina preforms

Pore size

Table 5.1 gives an overview of the pore shapes, average pore sizes and the size of the necks between pores. Figure 5.1 shows the microstructures of the four different porous ceramics produced, all at the same magnification for the purpose of comparison. The surface structure of the wool fibres has been reproduced in the pore channel surface (compare figures 3.2 and 5.1).

Porosity

The average open, closed and total porosities of the different porous ceramic preforms is shown in table 5.2. The samples measured were mostly plates ready to be infiltrated. The sample names contain the target porosity, not the actual porosity. The starch based samples, 5s-20 and 15s-20, had a 17 to 19 % closed porosity compared to 4 to 5 % open porosity, showing that percolation of the porosity in these samples was not achieved. In comparison 1p-20 and 30f-20 samples had open porosities of 18 and 23 % and closed porosities of 3 and 0 %, respectively. Sample 30f-50 had relatively high amount of closed porosity, 8 %, compared to the other 30f samples, 0 to 1 %. The total porosities were in general within 3 % of the target porosity, with the exceptions of 1p-30 with 6 % more and 5s-30, 15s-50 and 30f-20, all with 4 % more open porosity than the target.

Table 5.1: Pore shapes, pore neck sizes from mercury porosimetry and pore sizes from SEM image analysis.

sample	pore shape	pore neck size, μm	avg pore size, μm	St.Dev.
1p	ligaments	0.7	1	<1
5s	spheres	1.3	5	1
15s	spheres	2.0	15	2
30f	fibres	4.7	30	8

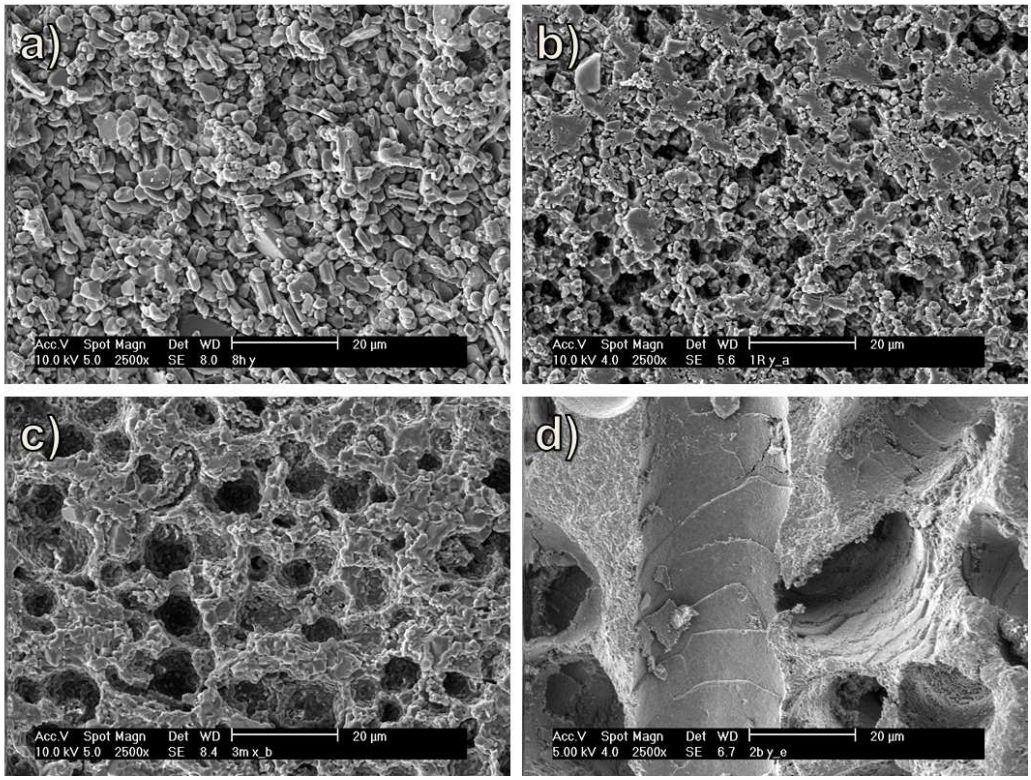

Figure 5.1: SEM images of porous samples based on a) partially sintered HVA FG, b) rice starch, c) corn starch and d) wool felt. Scale bar represents 20 μm.

Table 5.2: Closed, open and total porosities of porous ceramic preforms (+/- is the standard deviation).

sample	% open porosity	+/-	% closed porosity	+/-	% total porosity	+/-
1p-20	17.9	1.8	3.0	2.0	20.9	2.6
1p-30	32.7	1.3	3.5	0.9	36.2	1.5
1p-40	38.7	3.3	2.9	1.3	41.6	3.3
5s-20	4.9	0.1	17.4	0.2	22.3	0.3
5s-30	34.2	0.6	0.2	0.1	34.4	0.6
5s-40	37.9	3.1	2.8	2.9	40.7	2.8
5s-50	45.2	1.4	2.4	1.4	47.6	1.4
15s-20	4.2	1.7	18.6	1.3	22.8	0.4
15s-30	22.7	3.4	8.4	1.6	31.1	1.9
15s-40	38.2	4.7	4.4	3.3	42.6	1.4
15s-50	49.4	4.0	4.6	2.9	54.0	1.6
15s-60	57.9	2.7	2.4	1.1	60.3	2.2
30f-20	23.3	1.4	0.2	0.2	23.5	1.5
30f-30	32.3	1.5	0.1	0.2	32.3	1.4
30f-40	38.5	1.0	1.5	2.3	40.0	3.0
30f-50	43.0	0.1	13.5	0.1	56.5	0.1

5.1.2 Composites

Microstructure and composition

The microstructures of the four types of composites produced are shown at the same magnification for the purpose of comparison in figure 5.2. In the partially sintered samples (1p), the copper network fills the spaces between single alumina grains connected at small points. In the starch based samples (5s and 15s) the copper network consists of copper spheres joined by small necks between each sphere. Inside some of the copper spheres is a cluster of alumina, also seen in figure 5.1. The wool felt based samples (30f) contain a copper network consisting of long tangled fibres, as in the felt, with a limited number of contact points between individual fibres. The average amounts of copper, alumina and residual porosity in each type of composite is shown in table 5.3. Here, the sample names contain the target copper content, not the actual copper content. The samples measured were either infiltrated plates with the porous outer layer ground away, bending bars or compact tension samples. The residual porosities were generally around 2 to 4 %, with the exceptions of 5s-20 with 9 % and 15s-20 with 8 %. These values are lower than the closed porosities measured in the porous ceramic preforms (table 5.2). The average copper content was generally within 4 % of the target value, apart from the two aforementioned samples with high residual porosity and 15s-60 with 5 % less copper than the target.

X-ray computer tomography

The data produced during the X-ray scans of cylindrical samples of 15s-30 and 30f-30 was processed to generate 3D images of the copper networks of the samples (figure 5.3). It can be seen that the microstructure is isotropic in the starch based (5s) sample. In the wool felt based sample (30f) the microstructure is anisotropic. The majority of the fibres run along the X-Y plane, with some movement in the Z-direction. The fibre packing is more dense in the Z-direction due to the production method of the wool felt.

Table 5.3: Average compositions of alumina-copper composites (+/- is the standard deviation).

sample	vol.% porosity	+/-	vol.% copper	+/-	vol.% alumina	+/-
1p-20	1.3	1.0	20.8	2.7	77.9	1.9
1p-30	2.7	2.3	30.0	2.9	67.3	3.0
1p-40	1.8	1.5	40.8	5.2	57.3	5.0
5s-20	9.8	1.0	11.5	1.2	78.7	0.2
5s-30	4.4	1.1	25.6	0.9	70.0	0.1
5s-40	2.3	2.1	37.7	1.9	60.0	0.6
5s-50	3.5	0.4	43.0	0.2	53.5	0.1
15s-20	8.5	1.9	13.0	2.6	78.5	0.9
15s-30	5.2	1.5	25.5	1.6	69.3	0.0
15s-40	1.8	2.5	38.1	2.0	60.0	1.5
15s-50	3.5	2.7	45.7	2.4	50.8	2.2
15s-60	2.2	0.6	55.2	2.1	42.6	2.0
30f-20	2.7	1.8	21.9	1.4	75.5	1.7
30f-30	2.2	1.3	29.8	1.5	68.8	1.2
30f-40	4.2	3.5	36.3	7.2	59.5	4.8
30f-50	2.5	2.4	50.9	1.9	46.7	1.0

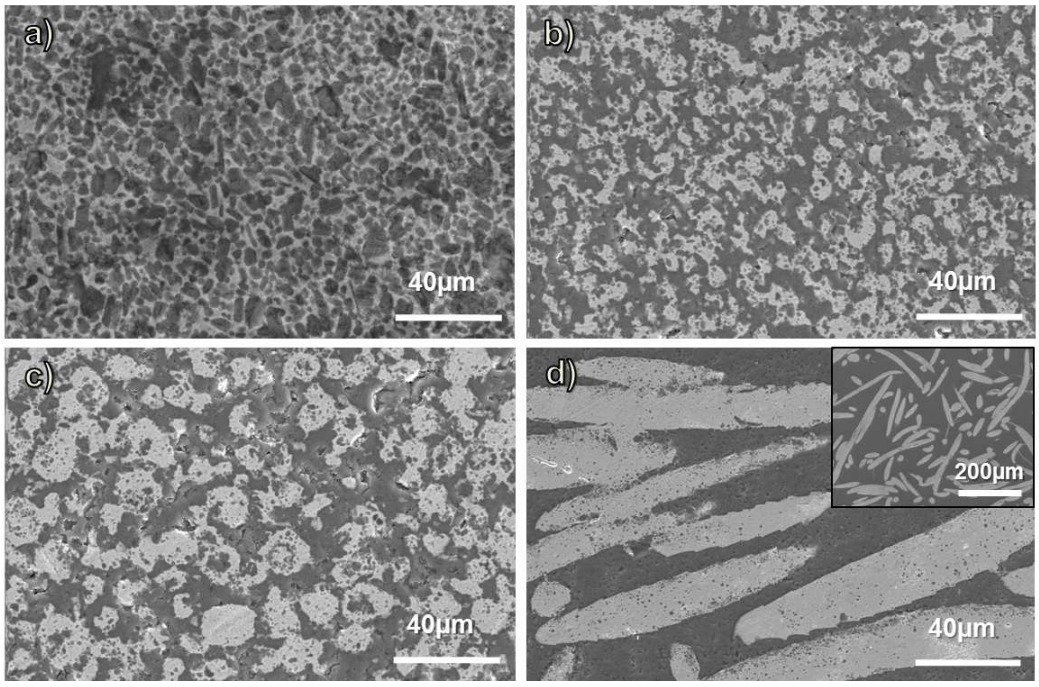

Figure 5.2: HRSEM images (at equal magnification) of alumina-copper composites based on a) HVA FG, b) rice starch, c) corn starch and d) wool felt, with insert of lower magnification to better see the overall structure. The lighter phase is copper, the darker phase alumina.

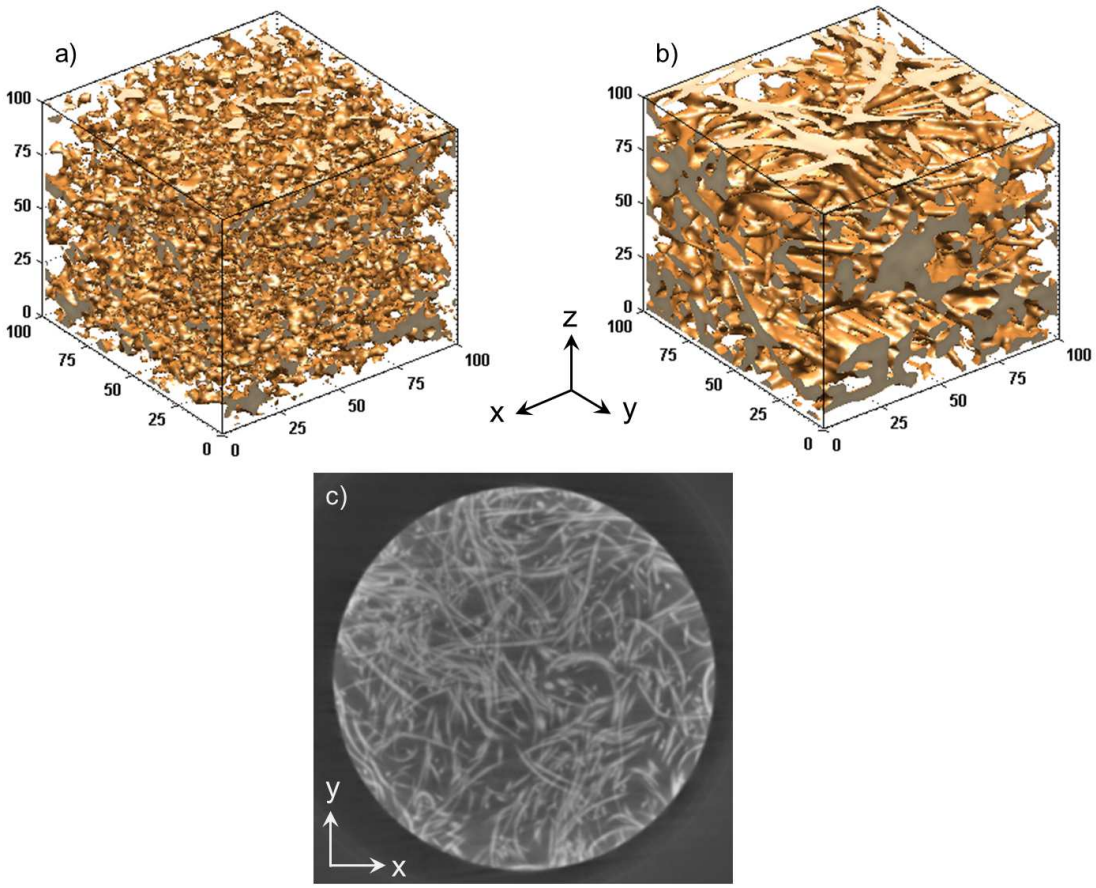

Figure 5.3: 3D images generated from X-ray CT data of the copper network from composites based on a) corn starch and b) wool felt. Both contain 30 vol.% copper. The scale is in voxels with 1 voxel representing 4.85 μm. c) A 2D slice of the wool felt based sample taken from the X-ray CT data. The circle has a diameter of 2 mm [113].

5.2 Mechanical properties

5.2.1 Young's modulus

a) Experimental:

The experimental values of Young's modulus are shown in figure 5.4. Young's modulus decreases with increasing copper content from around 260 to 283 GPa at 20 to 22 vol.% Cu down to 158 to 172 GPa at 50 to 54 vol.% Cu. Looking at the data points around 36 vol.% Cu, Young's modulus decreases from 254 to 237 to 214 GPa with increasing copper ligament diameter from 5 to 15 to 30 μm. The value of Young's modulus for a copper ligament diameter of 1 μm, 225 GPa, lies between that of the 15 and 30 μm data points. There is a large scatter in Young's modulus for the 5s-28 sample of 50 GPa, corresponding to the large scatter in copper content of 12 vol.%. .

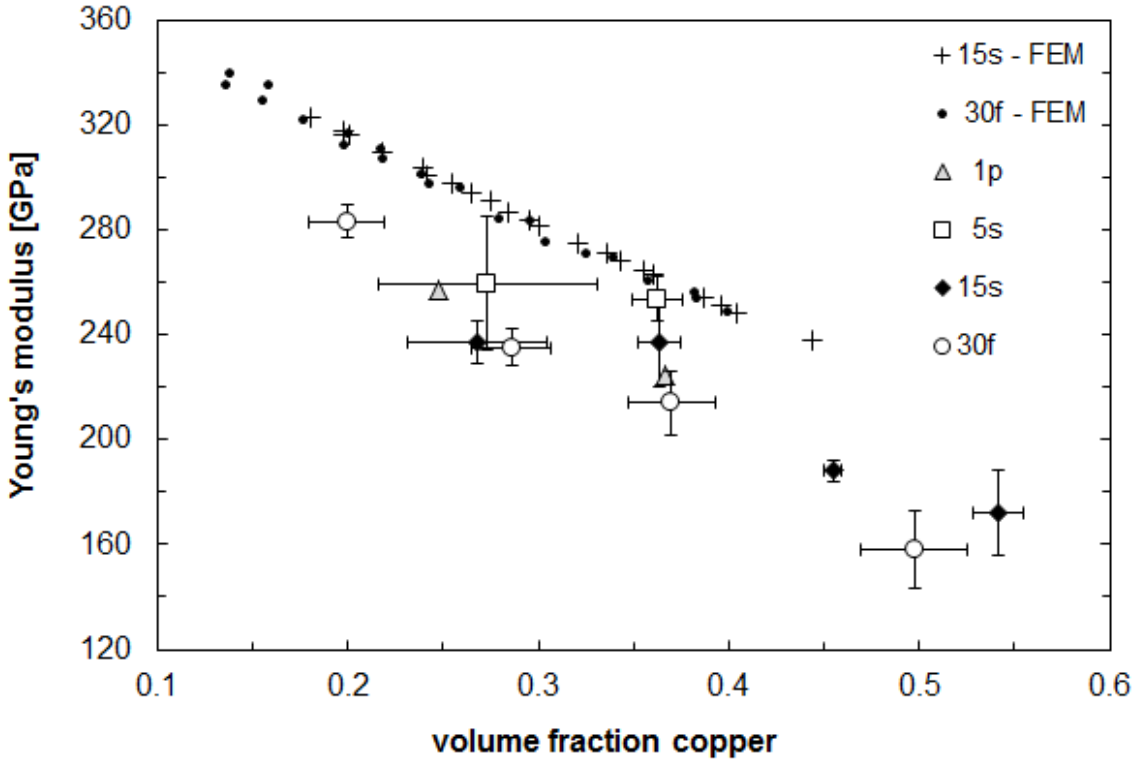

Figure 5.4: Young's modulus of different copper-alumina composites determined experimentally and from finite element modelling (FEM) based on X-ray computer tomography images.

b) Finite element modelling:

In figure 5.4, the values of Young's modulus based on finite element modelling of the 3D X-ray CT images of two samples, 15s-30 and 30f-26, are shown. The range in the copper volume fraction comes from the local variations of copper content within the samples scanned. There is a linear decrease in Young's modulus with increasing copper content from 314 GPa at 14 vol.% Cu to 238 GPa at 44 vol.% Cu. The FEM values are roughly 30 GPa higher than the experimental values. The amount of scatter in the data decreases from 7 GPa at the lowest copper content to 0 GPa at the highest copper content. The amount of scatter is also lower for the 15s sample than the 30f sample.

5.2.2 Hardness

Figure 5.5 shows the variation in hardness with copper content. It can be seen that hardness decreases with increasing copper content. There is a sharp decrease in hardness from 6.3 to 7.5 HV down to 2.6 to 3.6 HV with an increase of 15 to 35 vol.% Cu, with a more gradual decrease in hardness of 1.3 to 3.5 HV above 35 vol.% Cu. With the exception of the 30f data series, the hardness decreased slightly with decreasing copper ligament diameter.

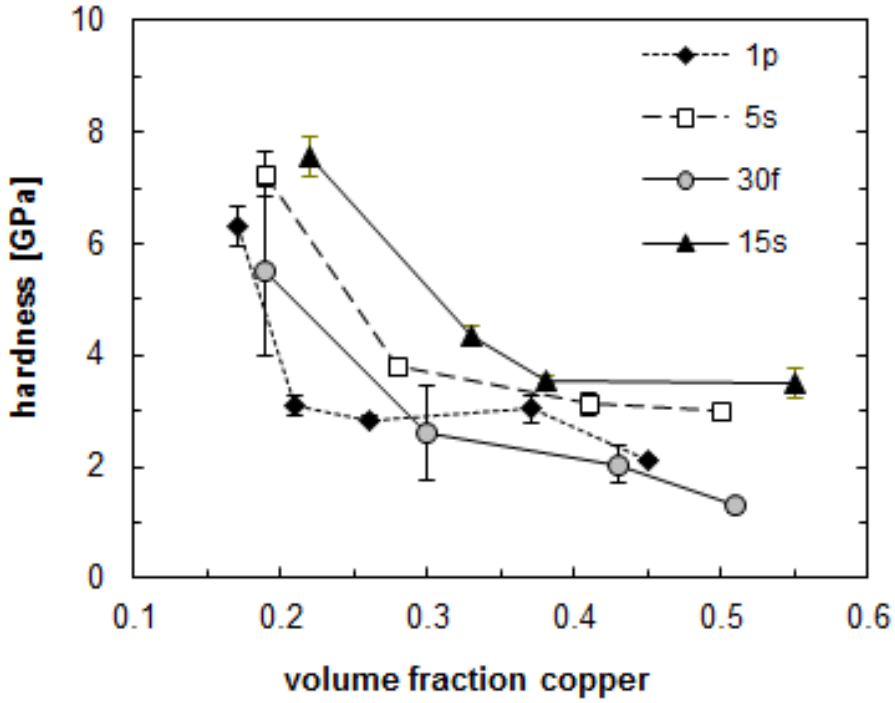

Figure 5.5: Variation in Vickers hardness with copper content.

5.2.3 Bending strength and fractography

As seen in figure 5.6, the bending strength increased from 90 to 319 MPa with increasing copper content from 19 to 55 vol.%. The data points with a low scatter were taken from the average of only three to four measurements. A limited amount of samples were tested due to the destructive nature of test and the difficulty producing samples. The 15s-47 samples had a particularly low bending strength of 155 MPa in comparison to the general trend. They also had a higher residual porosity than the other samples (4.5 vol.% compared to 0.5-1 vol.%). The effect of copper ligament diameter is not clear. Since only a limited number of samples were available, the Weibull moduli were only calculated for the two sample sets with more than 10 measurements, with the results in figure 5.7. The 15s-47 and 15s-40 samples had Weibull moduli of 4.0 and 9.4, respectively.

Figure 5.8 shows typical fracture causing defects found in the 5s and 15s samples. All images, except for figure 5.8 e), were in back scattered mode in order to show the different phases more clearly. Figure 5.8 e) was not in back-scattered mode so as to emphasise the structure. Image a) shows a large copper region. Image b) shows an area of residual porosity in the lower right region. Image c) shows an abnormally large alumina grain. The dark regions in image d) were found under EDS analysis to be carbon. These regions were found on the surface as well as within the volume. Image e) shows a machining defect on the surface of the sample. Image f) shows quite a large structural defect which had not been filled with copper.

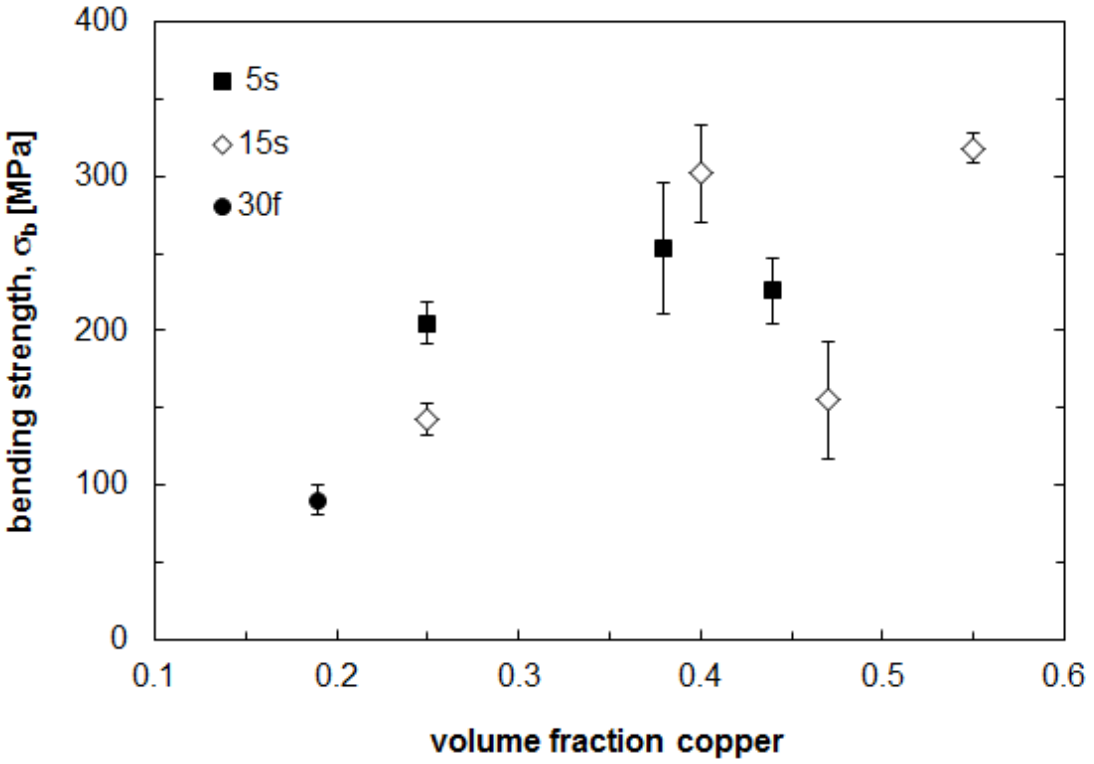

Figure 5.6: Bending strength of a range of composites with error bars showing the standard deviation.

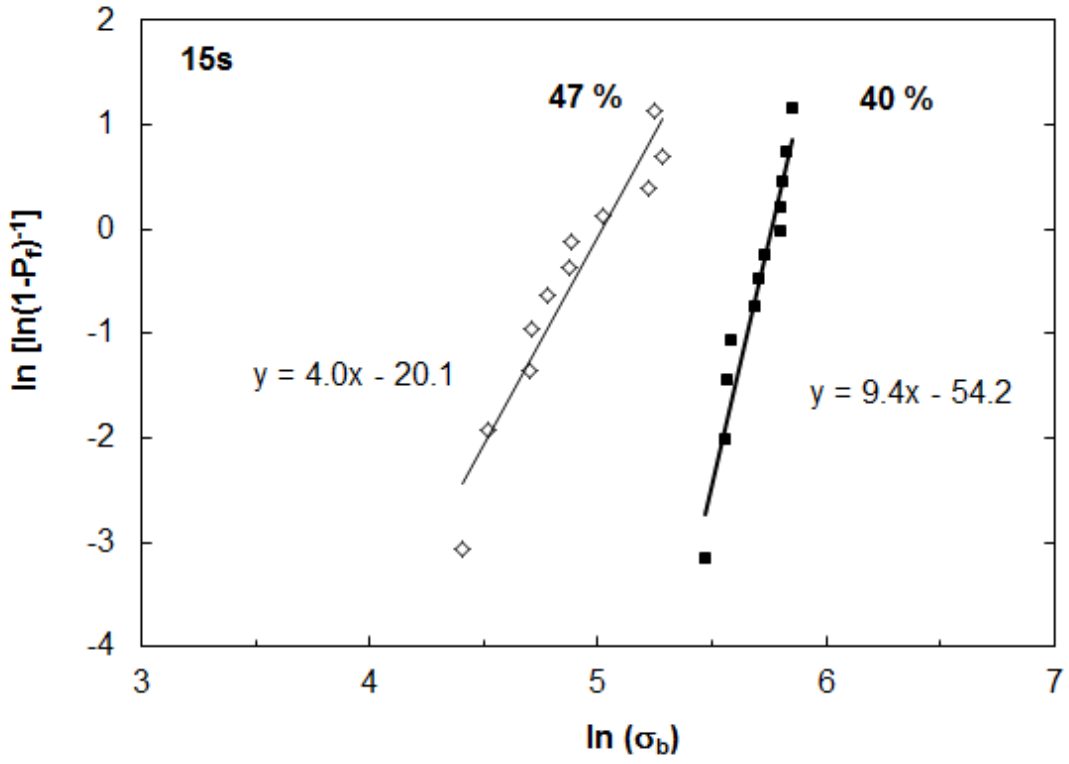

Figure 5.7: Double log graph to calculate the Weibull modulus of two sample sets: Cu ligament diameter 15 μm with Cu contents of 40 and 47 vol.%.

Figure 5.9 shows representative fracture surfaces of the 30f samples. In these samples no obvious fracture causing defects were found. There are, however, some features revealing more details about the microstructure than had been observed in the SEM images of polished surfaces (compare with figure 5.2). Image a) shows that the fibres along the surface had been pulled out up to several millimetres. Fibres perpendicular to the surface surrounded in a black region reveal delamination and necking of the fibres. In image b) there are dimples along the surface of the copper fibre. In image c) there are 'flakes' of copper to be seen. It can also be seen that the copper fibres have undergone extensive plastic deformation: stretching and necking before fracture. The slip planes of dislocation movement can be seen at the tips of the fractured copper fibres.

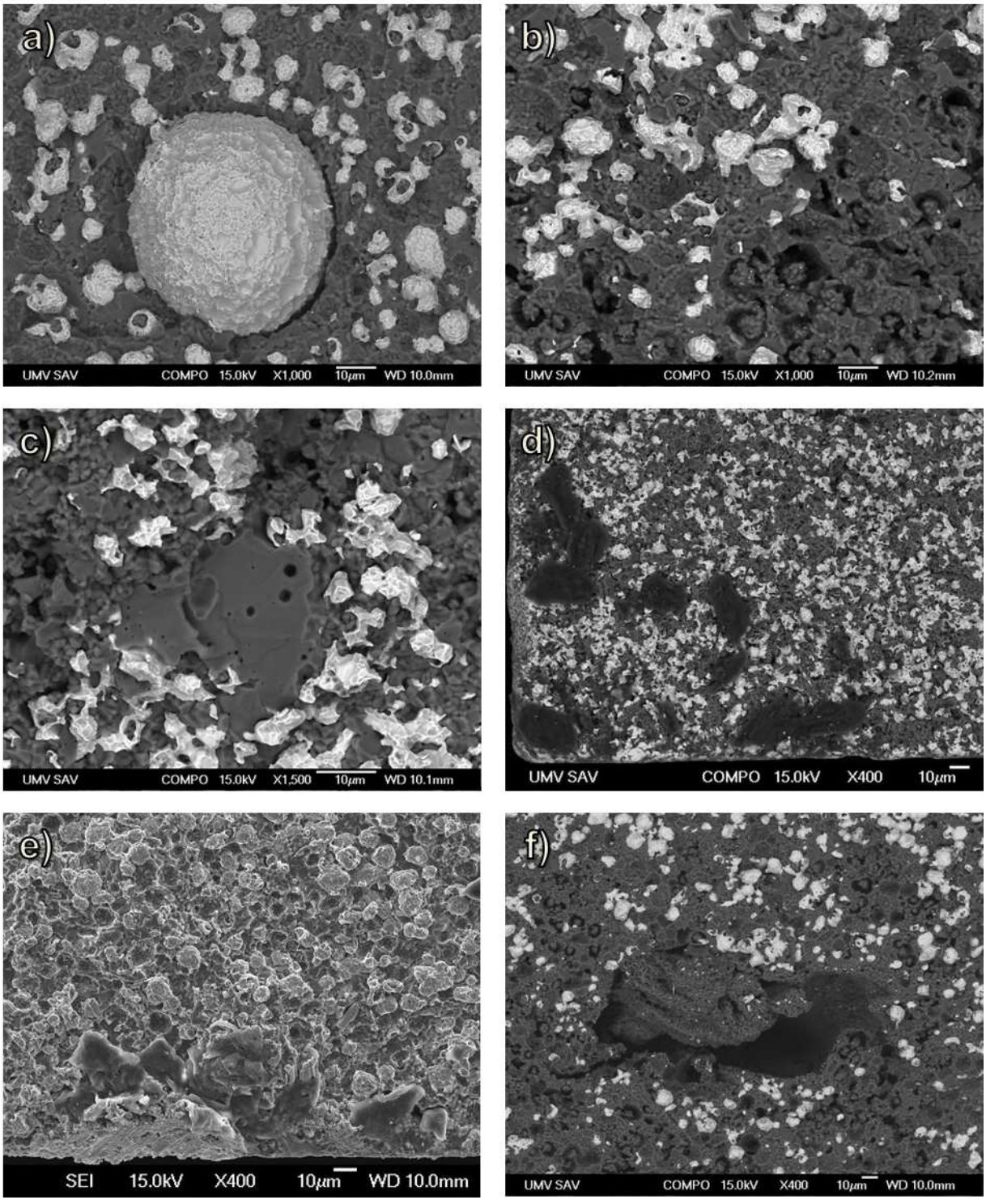

Figure 5.8: Fracture surfaces of starch-based samples with fracture causing defects: a) air bubble filled with copper, b) residual porosity, c) large alumina grain, d) carbon impurities, e) machining defect and f) structural defect. The bright phase is copper.

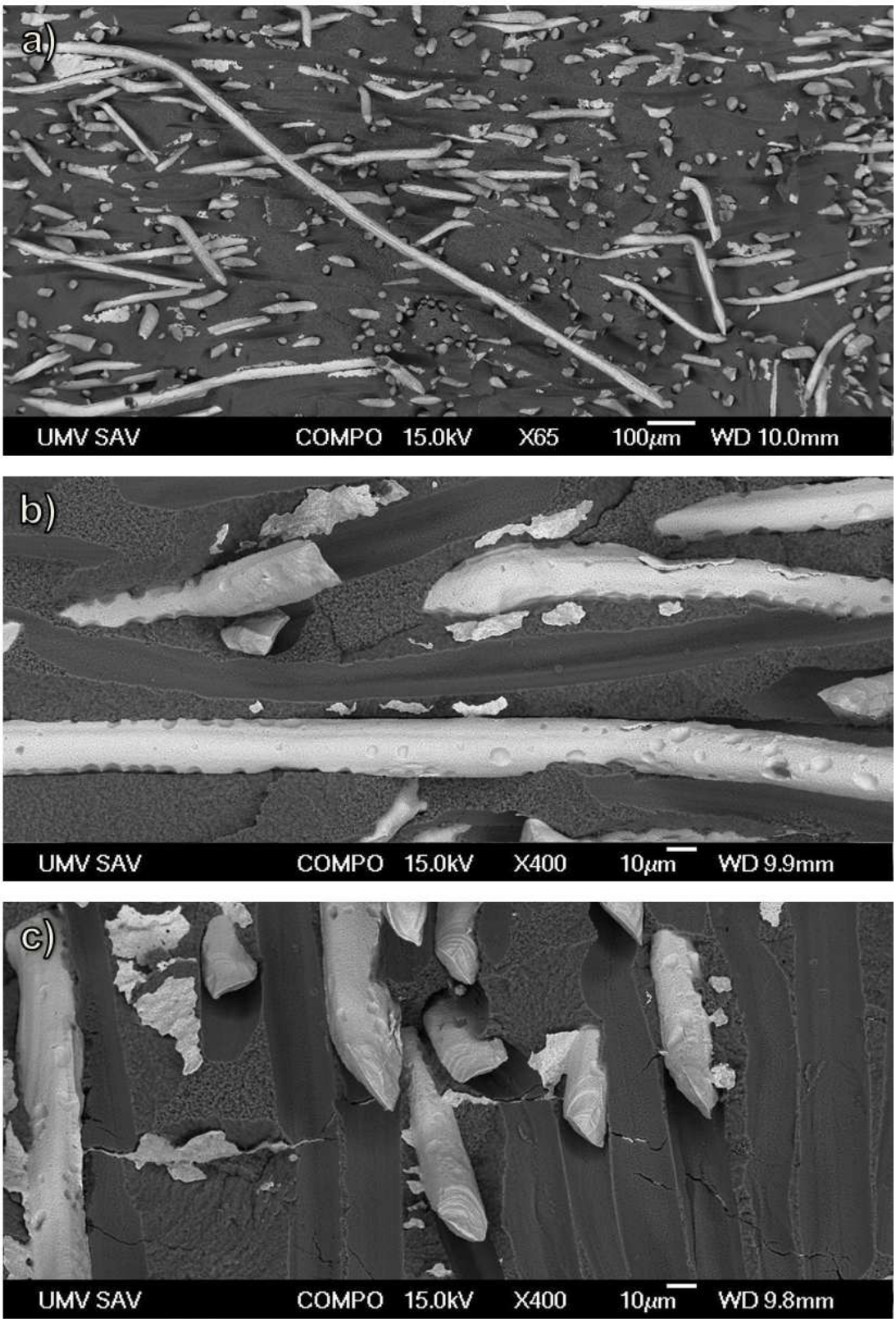

Figure 5.9: Fracture surfaces of 30f samples. The bright phase is copper. There are no obvious fracture causing defects. Microstructural features include: a) extensive delamination of copper fibres from matrix, b) dimples along the copper fibres and c) necking and fracture of copper fibres, and cracks in alumina filled with copper.

5.2.4 Fracture toughness

Single edge V-notched beam (SEVNB)

a) Crack paths: In figure 5.10 are some examples of crack paths and typical crack bridging mechanisms observed. Images a) and b) show sample 1p-25. In image b), the crack path of 1p-25 can be seen to travel along alumina-copper interfaces, between alumina grains (intergranular), through the copper and even through an alumina grain (intragranular). The copper bridging the gap has already fractured even though the crack is not particularly wide. An inelastic bridge around 8 μm wide can be seen in image a). Alumina grains are rounded and contact mostly at small points.

Images c) and d) show sample 5s-26 and images e) and f) show sample 15s-35. In both samples the crack grows mostly through the alumina, around copper spheres along the alumina-copper interface, with the approximately 1 μm wide points of contact between copper spheres bridging the crack. Image d) also shows crack branching in the 5s sample.

Sample 30f-21 is shown in images g) and h). The crack grows through the alumina network and is bridged by copper fibres. The crack also grows along alumina-copper interfaces. The fibres bridging the crack are delaminated from the alumina up to around 60 μm from the crack. Crack branching can also be seen. In image g) it can be seen that the fibres perpendicular to the crack have been pulled out and stretched up to 100 μm before necking and breaking. All samples also showed crack deviation, which is also a toughening mechanism.

b) Fracture surfaces: Some examples of fracture surfaces can be seen in figure 5.11. Sample 1p-25 is shown in images a), b) and c). Fracture is predominantly intergranular, with isolated grains where intragranular fracture has occurred (as seen also in figure 5.10 b)). There is some delamination between alumina and copper. Copper has plastically deformed to chisel points, with a close-up shown in image b). Image c) shows a large copper region with a 1 μm gap between the alumina and the copper. The copper has plastically deformed upon pulling away from the alumina.

Images d) and e) show 5s-26 and 15s-35, respectively. Fracture is intergranular. There appears to be less plastic deformation in the copper phase compared to 1p-25, due to the crack often growing along the alumina-copper interface. There are some regions where copper has delaminated from the alumina perpendicular to the crack front, and others where the copper is still bonded to the alumina.

Parts of the fracture surface of the 30f-21 are shown in images f), g) and h). There is extensive delamination of the copper from the alumina, with all visible interfaces

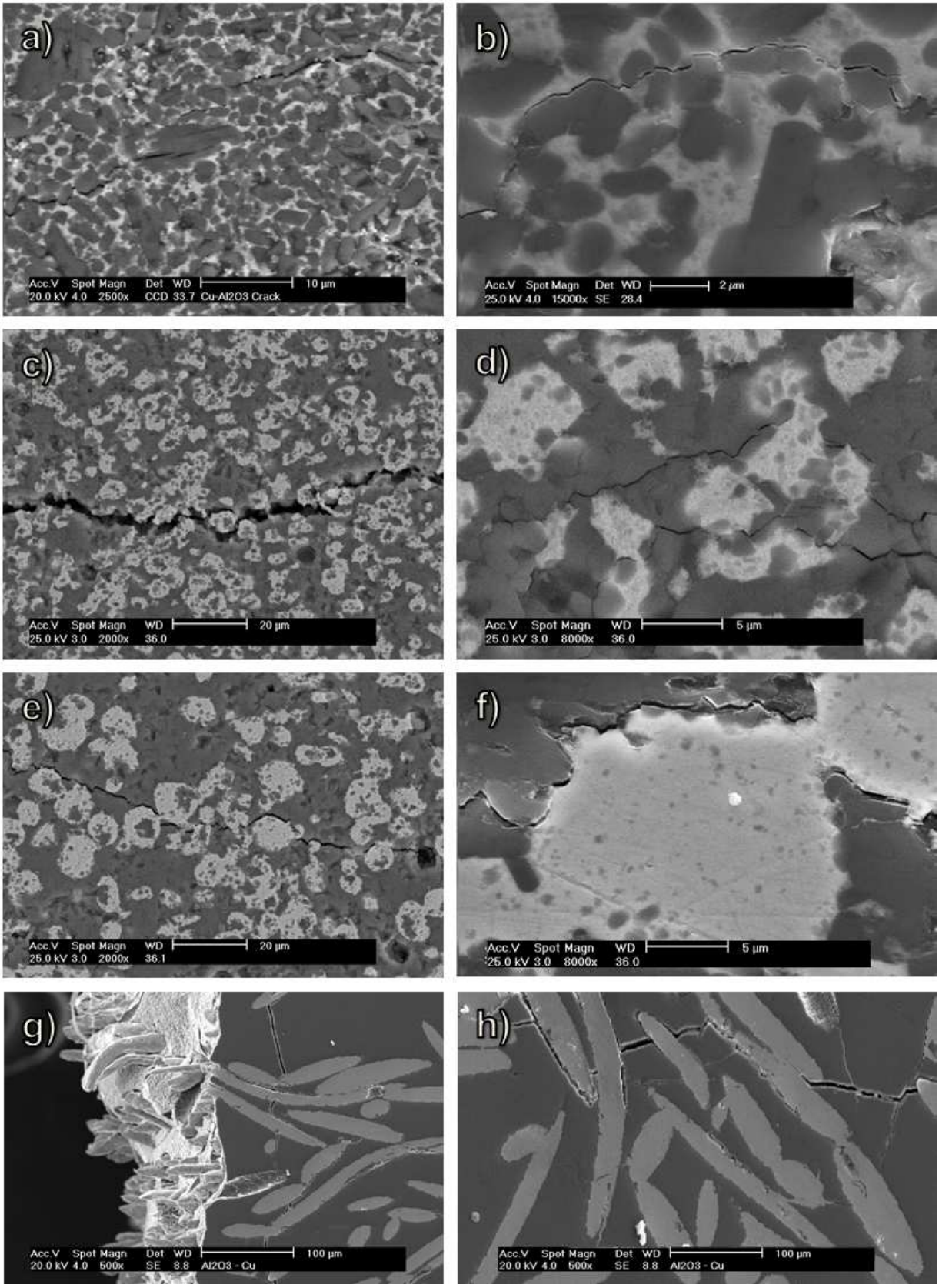

Figure 5.10: Crack path images from SEVNB crack extension in samples a), b) 1p-25, c), d) 5s-26, e) f) 15s-35, and g), h) 30f-21.

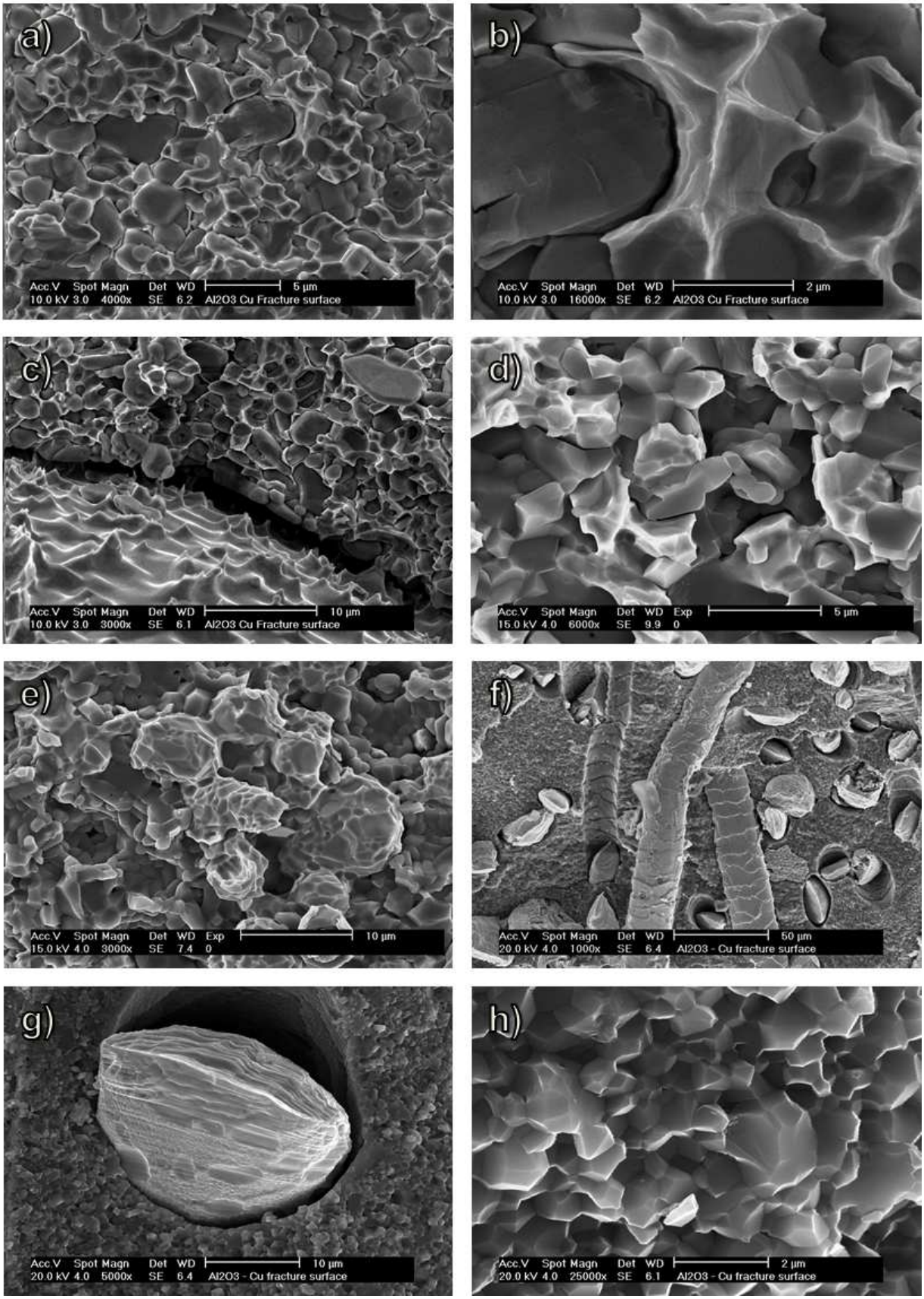

Figure 5.11: Fracture surface images from SEVNB crack extension in a), b), c) 1p-25, d) 5s-26, e) 15s-35, f), g), h) 30f-21.

delaminated, shown by the black areas around the copper. The copper fibres have stretched and necked before fracturing to form chisel points. The alumina grains are highly faceted and fracture in the alumina is intergranular.

c) R-curves: The R-curves of a selection of composites are shown in figure 5.12. The only sample where a plateau was reached was 5s-26: from crack lengths of 2.7 to 3.1 mm the fracture toughness was 6.3 MPa$\sqrt{\text{m}}$. It is not possible to make a detailed comparison of the R-curves. Nevertheless, a few observations have been made. The curves of 15s-39 and 5s-26 follow a very similar path. 15s-35 started 1 MPa$\sqrt{\text{m}}$ lower that 15s-39, but rose more steeply to approach the other curves. 5s-37 started 1.2 MPa$\sqrt{\text{m}}$ higher and was flatter, but failed before the whole R-curve could be captured. The R-curves of the 30f samples rose with increasing copper content, although the curves overlap for 44 and 53 vol.% Cu. Up until a crack length of 2 mm the slopes of the curves are similar. Above this crack length, the scatter of the data makes it difficult to compare the slope of the curves. In most samples no plateau in the R-curve was achieved. Further R-curve measurements were carried out on CT samples, where much longer crack lengths were possible, to attempt to achieve a plateau in the R-curves for all samples.

Compact Tension (CT)

A summary of the R-curves measured with CT samples is shown in figure 5.13. In figure 5.13 a), the effect of copper content on the 15s samples is shown. The plateau value of K increased from 4.4 to 6.4 to 8.8 MPa$\sqrt{\text{m}}$ for increasing copper contents from 15 to 41 to 55 vol.%. The crack length where the plateau value of K was achieved increased from approximately 1.4 to 2.0 to 2.5 mm, respectively. Figure 5.13 b) illustrates the effect of copper content on the 30f samples. The data points are further apart than in the 15s samples because of the larger distance between copper ligaments. The plateau values for copper contents of 22 and 28 vol.% were around 6.0 and 6.8 MPa$\sqrt{\text{m}}$, respectively. For the samples with higher copper contents, no plateau in the R-curve was achieved with the CT sample geometry used. The R-curves with these samples were remeasured up to a crack length of 12 mm. Above a crack length of 2 mm, K increased linearly with crack length.

In general, the R-curves rose with increasing copper content. There is, however, very little difference between the curves for 39 vol.% and 48 vol.% copper. Figure 5.13 c) shows the effect of copper ligament diameter of samples with approximately 40 vol.% copper ($\pm$2 vol.%). For increasing copper ligament diameters from 1 to 5 to 15 μm, the slope of the R-curve increases and the plateau value of K also increases from 5.6 to 5.8 to 6.4 MPa$\sqrt{\text{m}}$. These curves intersect at a crack length of around 1 mm. For a ligament diameter of 30 μm, the R-curve is much higher than the other three curves.

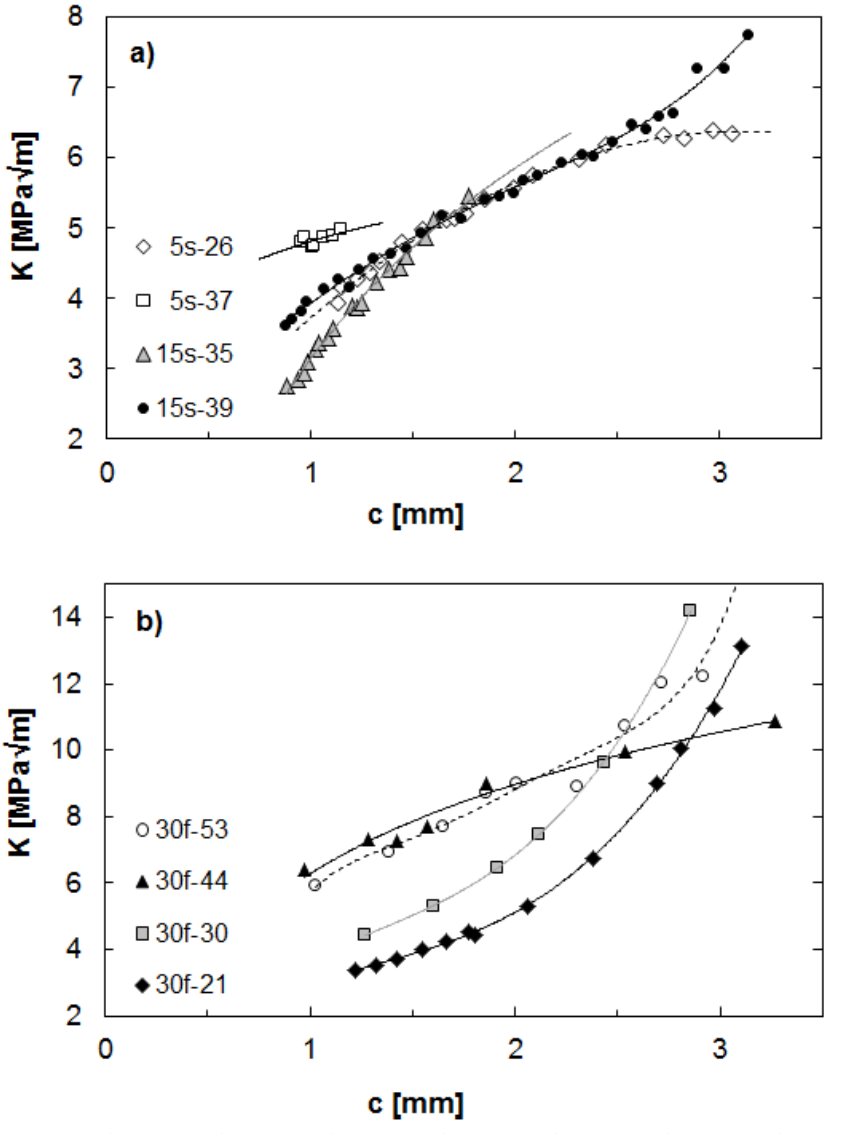

Figure 5.12: R-curves measured with the SEVNB method of composites with copper ligament diameters of a) 5 and 15 μm and b) 30 μm.

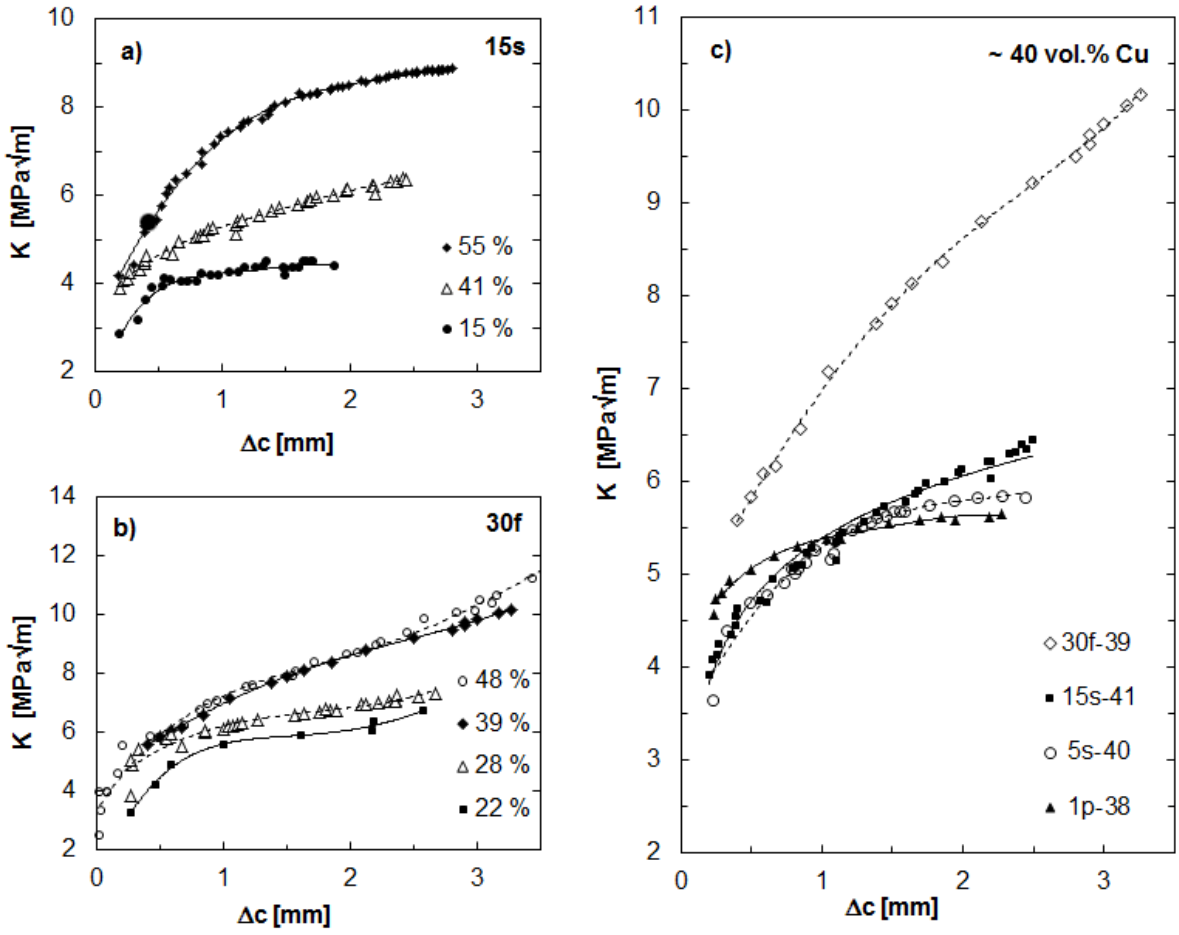

Figure 5.13: R-curves showing the effect of Cu content on composites with a Cu ligament diameter of a) 15 μm and b) 30 μm. R-curves showing the effect of Cu ligament diameter of composites with c) approximately 40 vol.% Cu.

5.2.5 Crack opening displacement

The crack profiles measured are shown in figure 5.14. The samples measured were 15s-15, 15s-41, 15s-55 and 1p-38. Since the 5s and 15s samples showed similar R-curve behaviour, no 5s samples were measured. Due to extensive crack bridging in the 30f samples, it was not possible to measure the crack profiles of theses samples. The data points represent the measured values. The solid lines show the parabolic crack profile expected for a crack without crack bridging, according to the Irwin equation (eq. 2.16).

The effect of varying copper content for a copper ligament diameter of 15 μm can be seen in figure 5.14 a). For increasing copper content, the width of the crack profile increases. Up until a distance from the crack tip of around 600 μm, the profiles follow a similar path. At this point they deviate from one another, increasing almost linearly towards the respective Irwin parabola. The distance at which the crack opening nears the Irwin parabola increases with increasing copper content: approximately 1.6, 2.1 and 2.4 mm for copper contents of 15, 41 and 55 vol.%, respectively.

The effect of varying copper ligament diameter (for a copper content of around 40 vol.%) is shown in figure 5.14 a). For increasing ligament diameter from 1 to 15 μm, the width of the crack profile increases. This effect is less pronounced than the effect of varying copper content. The crack length at which the crack opening approaches the Irwin parabola increases with increasing ligament diameter: approximately 1.5 and 2.1 mm for ligament diameters of 1 and 15 μm, respectively. This effect is more pronounced for varying ligament diameter than varying copper content. The extrapolation of the crack profiles to 100 % of the critical load and the determination of K_{IO} and R_μ is in section 6.2.5.

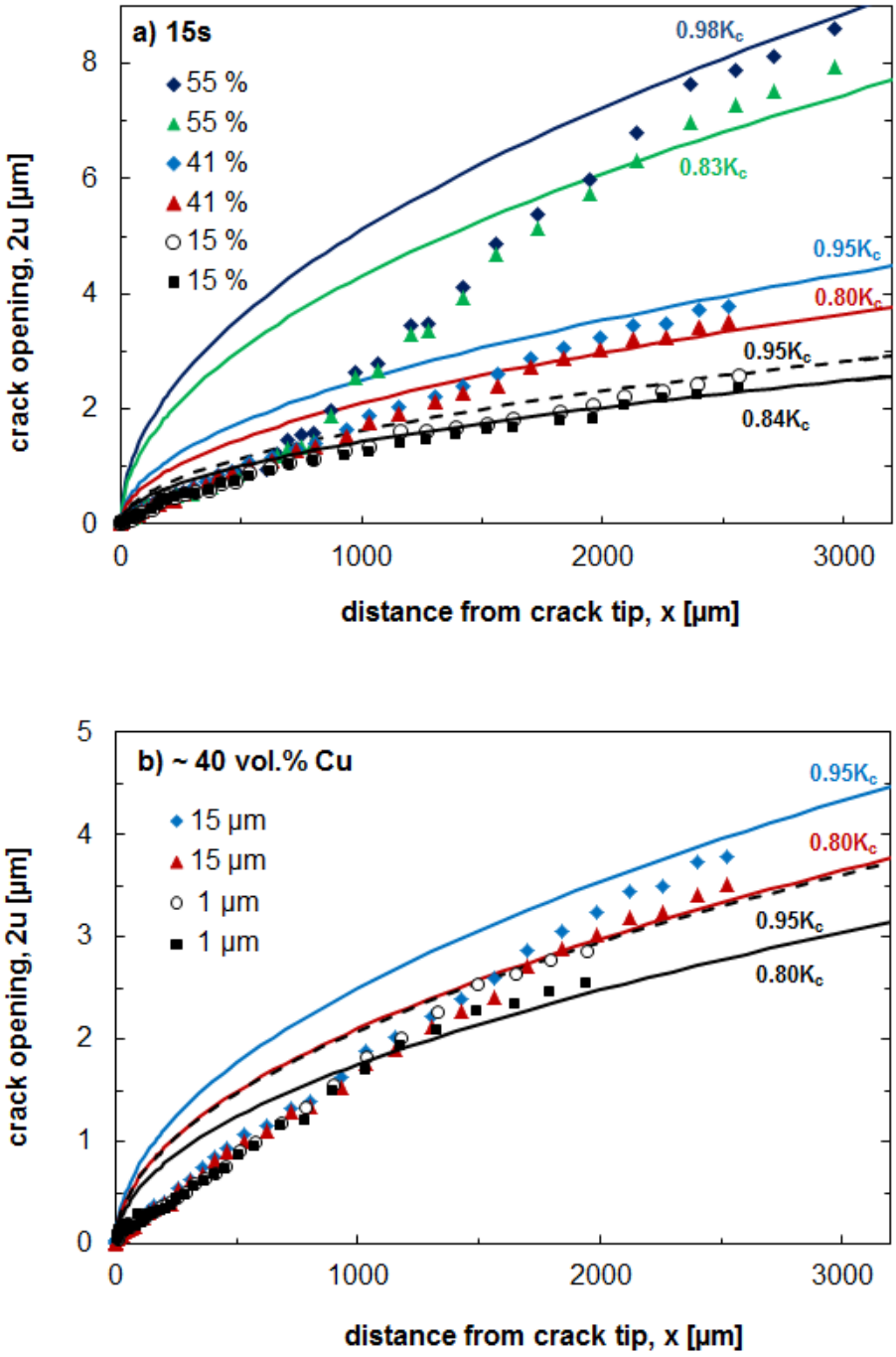

Figure 5.14: Crack profiles of samples with varying a) Cu content (ligament diameter 15 μm) and b) Cu ligament diameter (40 vol.% Cu). The data points are the measured values and the curves are the predicted Irwin parabolas for the respective applied K.

5.3 Thermal properties

5.3.1 Thermal expansion behaviour

Thermal strain

The thermal strain curve was measured four times for each sample, with the four curves shown for one representative sample in figure 5.15. After the first thermal cycle the sample had become shorter. Upon further cycling the effect decreased until the strain curve was closed in the third and fourth cycles. It was assumed that an equilibrium state had been achieved after four cycles. This effect was seen in the 5s and 15s samples but not the 1p and 30f samples, which did not shrink. The mass of all samples remained constant after each cycle.

In figure 5.16, the fourth cycle of thermal strain for each sample was plotted. The effect of varying copper content for a) 15 μm and b) 30 μm copper ligament diameter and the effect of varying ligament diameter for c) 30 vol.% Cu and d) 40 vol.% Cu is shown. The arrows indicate that the upper part of the curve was measured during heating and the lower part of the curve during cooling. The thermal strain curves for pure copper and pure alumina are shown for comparison. These curves follow the same path for cooling and heating, however, most of the curves for the composites show hysteresis.

i) Effect of copper content: In the 15s samples, increasing the copper content from 27 to 38 to 43 vol.% led to an increase in the maximum strain from 0.69 to 0.81 to 0.91 %, respectively (figure 5.16 a)). The area of the hysteresis decreased by 13 % and then 7 %. In the 30f samples, increasing the copper content from 31 to 39 to 53 vol.% led to an increase in the maximum strain from 0.70 to 0.81 to 1.07 % (figure 5.16 a)). The area of the hysteresis decreased by 4 % and then 82 %. The cooling curves of the samples with 27-31 vol.% Cu (apart from 1p-28) were very close to the strain curve of alumina (figure 5.16 a),b),c)) and had a similar amount of hysteresis. The strain curve of 1p-28 was higher (peak strain 17 % higher than 15s-27 and 30f-31).

ii) Effect of copper ligament diameter: For the samples with approximately 30 vol.% copper, decreasing the ligament diameter from 30 to 15 μm had very little effect (figure 5.16 c)). The maximum strain decreased from 0.70 to 0.69 % and the area of the hysteresis decreased by 5 %. Decreasing the ligament diameter further to 1 μm, however, led to an increase in the maximum strain to 0.82 % and a reduction in the area of the hysteresis by 22 %. For the samples with approximately 40 vol.% copper (figure 5.16 d)) changing the ligament diameter had very little effect on the maximum strain: samples with a copper ligament diameter of 30, 15 and 5 μm had maximum strains of 0.81, 0.81 and 0.83 %, respectively. Despite the maximum strain being very similar, the strain curve

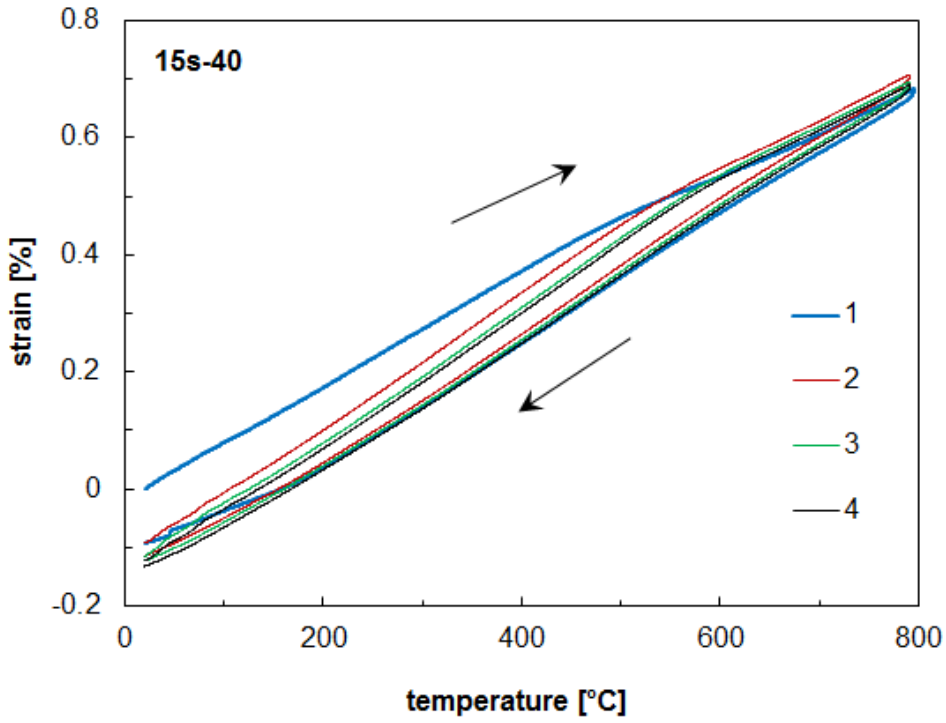

Figure 5.15: Thermal strain as a function of temperature for four consecutive cycles. The sample had a Cu ligament diameter of 15 μm and a Cu content of 40 vol.%.

of the 30f sample was lower in the intermediate region, particularly in the cooling curve. The strain at 400 °C was 0.40 compared to 0.42 and 0.41 % upon heating and 0.29 compared to 0.33 and 0.34 % upon cooling. Decreasing copper ligament diameter from 30 to 15 to 5 μm led to a decrease in the area of the hysteresis by 14 % and then 28 %. Note that the smallest ligament diameters in figures 5.16 c) and d) are not the same.

Coefficient of thermal expansion (CTE)

The physical coefficient of thermal expansion is plotted as a function of temperature in figure 5.17. For the sake of clarity, the curves were separated into different graphs for heating and for cooling. To eliminate the large amount of noise in the curve, average values across 20 °C were taken and plotted. This did not affect the overall shape of the curve. The values below 200 °C upon heating are not shown, due to equipment limitations causing large fluctuations in the curve. Upon cooling this was not a problem, since the cooling rate was much slower and the temperature thus more stable. The curve for pure alumina is also included as the black dashed line for comparison. The curve for alumina should be smooth and not have the fluctuations seen from 200 to 400 °C. All the curves for all the samples also have similar fluctuations in this temperature range, which is assumed to be an artifact of the testing method, possibly due to inaccuracy of the temperature measurement below 400 °C.

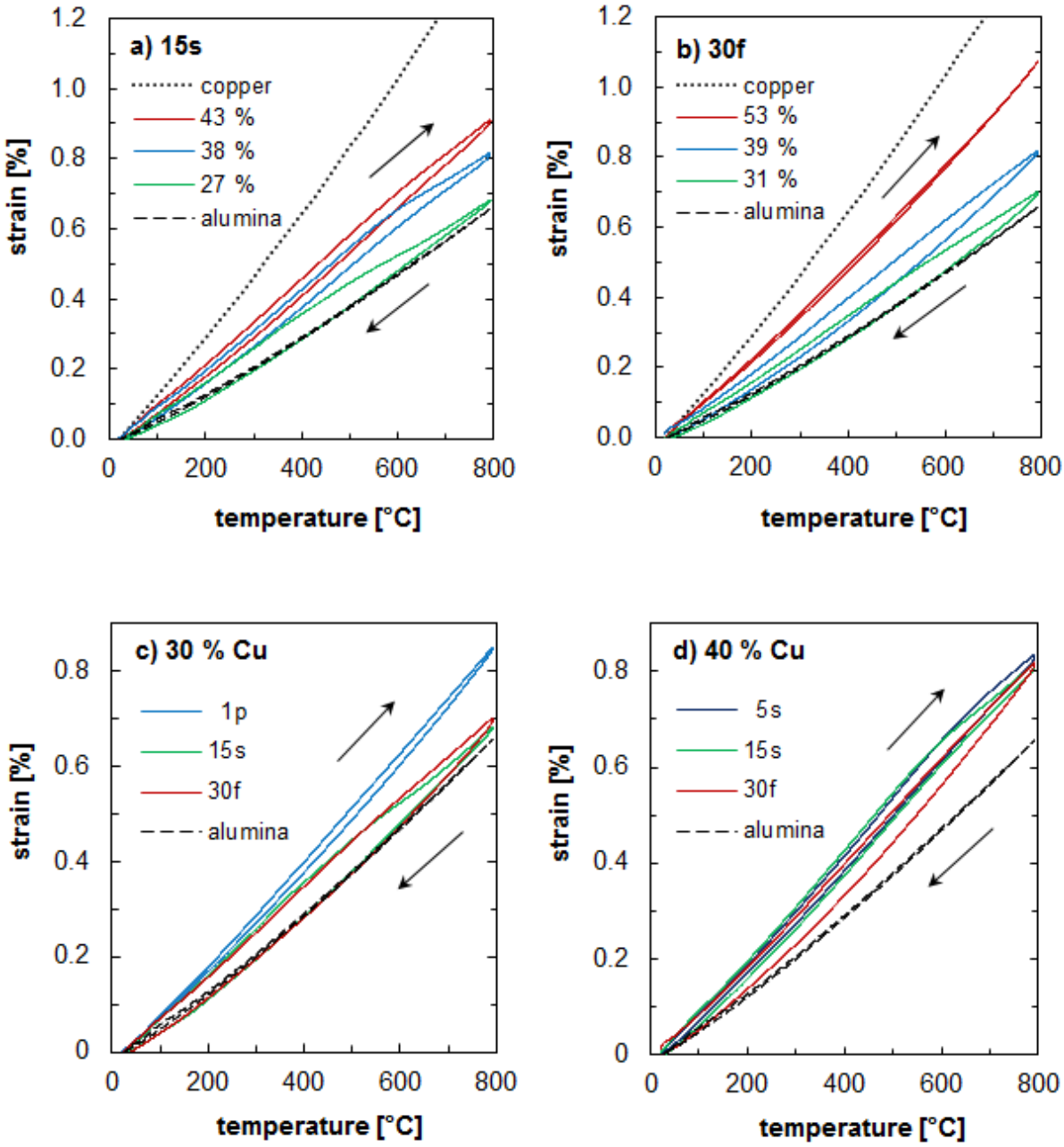

Figure 5.16: Thermal strain as a function of temperature showing the effect of varying Cu content for a) 15 μm and b) 30 μm Cu ligament diameter and the effect of varying ligament diameter for c) 30 vol.% and d) 40 vol.% Cu.

Upon heating, the CTE of the 5s and 15s samples (figure 5.17 a)) initially increased gradually from between 11.0 and 11.9×10^{-6} /K up to a maximum of between 12.1 and 12.4×10^{-6} /K at 470 °C for samples 15s-43, 15s-38 and 5s-38. Sample 15s-27 reached a maximum of 10.4×10^{-6} /K at around 310 °C. The curves then decreased steadily, with samples 15s-43, 15s-38, 15s-27 and 5s-38 reaching minimum values of 10.7, 8.3, 7.3 and 8.5×10^{-6} /K at 690, 680, 590 and 750 °C, respectively. The CTE curves of samples 15s-27, 15s-38 and 5s-38 cross and drop below the curve of alumina at temperatures of

450, 590 and 670 °C, respectively. After that, all the curves rose almost linearly with increasing temperature to final values of 10.9, 8.8, 9.1 and 8.6×10^{-6} /K, respectively. For the 15s samples, the temperature of the maximum and the minimum increased with increasing copper content. The curves also shifted to higher CTE values with increasing copper content. The 5s-38 sample behaved similarly to the 15s-38 sample, with the maximum CTE at a similar temperature but the minimum around 70 °C higher.

Upon cooling (figure 5.17 b)), the CTE of 15s-43, 15s-38, 15s-27 and 5s-38 started at much higher values than at the end of heating: 15.4, 13.0, 12.0 and 13.0×10^{-6} /K, respectively. There was initially a sharp decrease in CTE to 12.4, 10.2, 10.1 and 10.8×10^{-6} /K at 750 °C, followed by a broad minimum to 710 °C. The CTE of 15s-43 increased until 610 °C up to 12.8×10^{-6} /K, plateaued until 470 °C, then decreased almost parallel to the curve for alumina to a value of 10.3×10^{-6} /K at 110 °C. Finally the CTE dropped sharply to 8.3×10^{-6} /K at room temperature. The CTE of 15s-38 and 5s-38 increased until 490°C to 11.7×10^{-6} /K, then decreased parallel to the alumina curve to 10.0×10^{-6} /K at 170°C. After a small increase in the 5s-38 curve, both drop sharply below 110 °C to 7.1 and 7.9×10^{-6} /K, respectively by room temperature. The CTE of 15s-27 stayed almost constant until 530 °C (10.1 to 10.3×10^{-6} /K), then decreased almost parallel to the alumina curve to a value of 8.3×10^{-6} /K at 210°C. The CTE dropped down to 4.9×10^{-6} /K by room temperature. The values of CTE were overall higher for higher copper contents.

The variation of CTE with temperature of the 1p and 30f samples was different to that of 5s and 15s samples. Sample 1p-28 behaved very similarly to 30f-39 and so will not be described in detail separately. Upon heating to 330 °C, the CTE of 30f-31, -39 and -53 increased gradually from 9.1, 10.7 and 12.8×10^{-6} /K up to 9.9, 11.5 and 13.9×10^{-6} /K, respectively. With increasing temperature the CTEs stayed relatively constant (variation within 1×10^{-6} /K) for all samples except 30f-53. For this sample, the CTE increased almost parallel to the alumina curve up to 700 °C, with a sharp increase in the slope of the curve up to 800 °C to a final value of 17.9×10^{-6} /K. For the 30f samples, increasing copper content shifted the CTE curve upwards.

Upon cooling all the curves followed a similar trend: Starting at maximum values of 18.5, 15.5 and 14.7 $\times10^{-6}$ /K for 30f-53, -39, and 31, there was a sharp decrease in CTE down to 16.3, 12.8 and 11.8×10^{-6} /K at 750 °C, then a linear decrease parallel to the alumina curve down to 110, 130 and 170 °C to values of 11.3, 8.5 and 7.4×10^{-6} /K. Below this temperature there was a sharp decrease in CTE down to room temperature to values of 9.3, 5.9 and 5.2×10^{-6} /K, respectively. Below 110 °C the CTE of 1p-28 did not drop as sharply as the 30f samples and at room temperature had a value of 8.3×10^{-6} /K. There was no clear relationship between copper ligament diameter and CTE, apart from

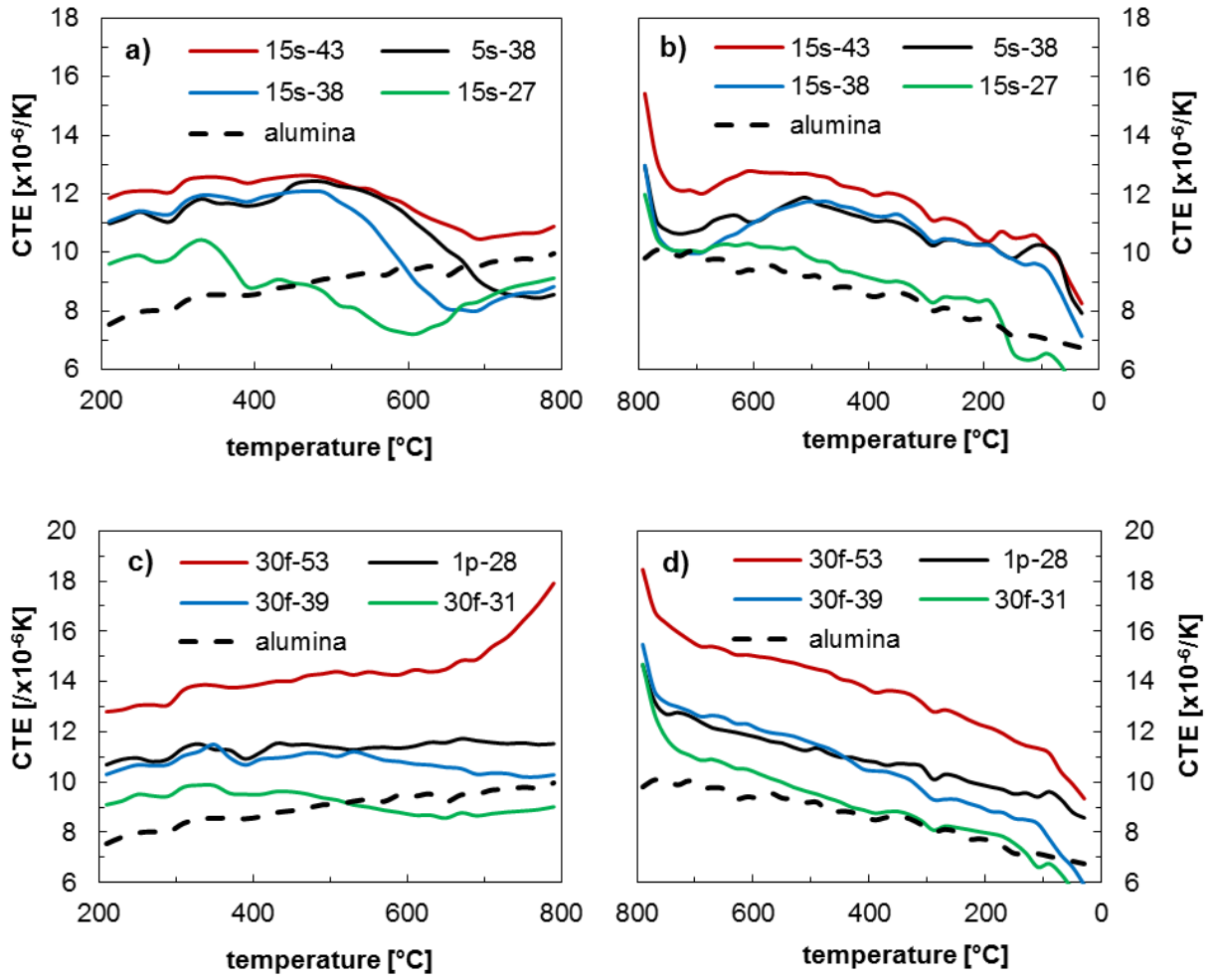

Figure 5.17: Instantaneous CTE for a) and c) heating from 200 °C and b) and d) cooling to room temperature.

that the 5s sample behaved similarly to the 15s samples, and that the 1p sample behaved similarly to the 30f samples.

The average CTE was calculated as the maximum strain over the total temperature range and displayed in figure 5.18. In general, the average CTE increased with increasing copper content. For the 1p samples an increase in copper content from 24 to 28 vol.% led to an increase in CTE from 10.6 to 11.0×10^{-6} /K. For the 15s samples an increase in copper content from 27 to 43 vol.% led to an increase in CTE from 8.9 to 11.8×10^{-6} /K. For the 30f samples an increase in copper content from 31 to 53 vol.% led to an increase in CTE from 9.1 to 13.9×10^{-6} /K. Although not enough samples were available to determine conclusively, indications are that the average CTE decreases with increasing copper ligament diameter (figure 5.18). However, the three samples with around 38 vol.% copper had a similar CTE: around 10.4 to 10.7×10^{-6} /K.

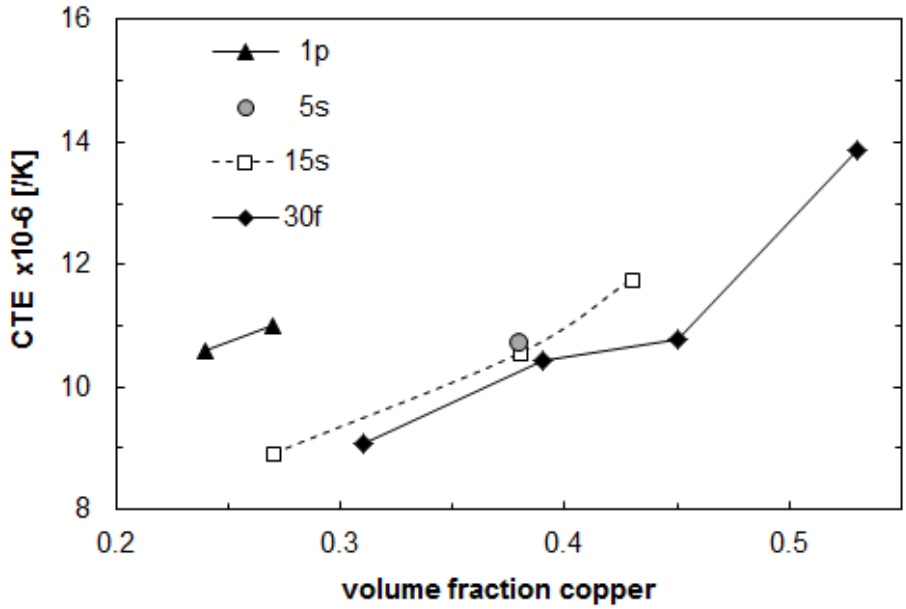

Figure 5.18: Variation in average CTE with copper content.

Change in sample length and Young's modulus

Since a reduction in sample length was observed after the first temperature cycle (figure 5.15), the reduction in sample length after each cycle was measured for every sample. This was taken from the final strain value after cooling to room temperature. The change in Young's modulus of the sample after each temperature cycle was also measured. The results are shown in figure 5.19. To make the results comparable, the changes in length and Young's modulus were reported as a percentage change for each heating cycle. In figure 5.19, a positive '-ΔL' means that the sample became shorter. A positive 'ΔE' means that the Young's modulus increased, and vice versa.

The length of the 15s-43, -38 and -27 samples all decreased after the first cycle: by 0.2, 0.1 and 0.05 %, respectively, minimally after the second cycle (max. 0.03 % for 15s-38), with hardly any change in length for the last two cycles (figure 5.19 a)). These changes could be measured with callipers. 5s-38 behaved similarly to 15s-38. The 1p and 30f samples stayed almost constant in length after each thermal cycle (figure 5.19b), with a maximum change of 0.01 % in any one cycle and sample. These changes were below the measurement resolution of the callipers.

The change in Young's modulus of the 15s samples was almost analogous to the change in length. After the first cycle, E of 15s-43, -38 and -27 samples had increased by 7.3, 3.4 and 0.8 %, respectively. After the second cycle, E of 15s-43 and -38 increased by 0.7 % with no further change in the following cycles. 15s-27 stayed constant after the third cycle and decreased by 3.1 % after the last cycle. 5s-38 behaved differently to 15s-38:

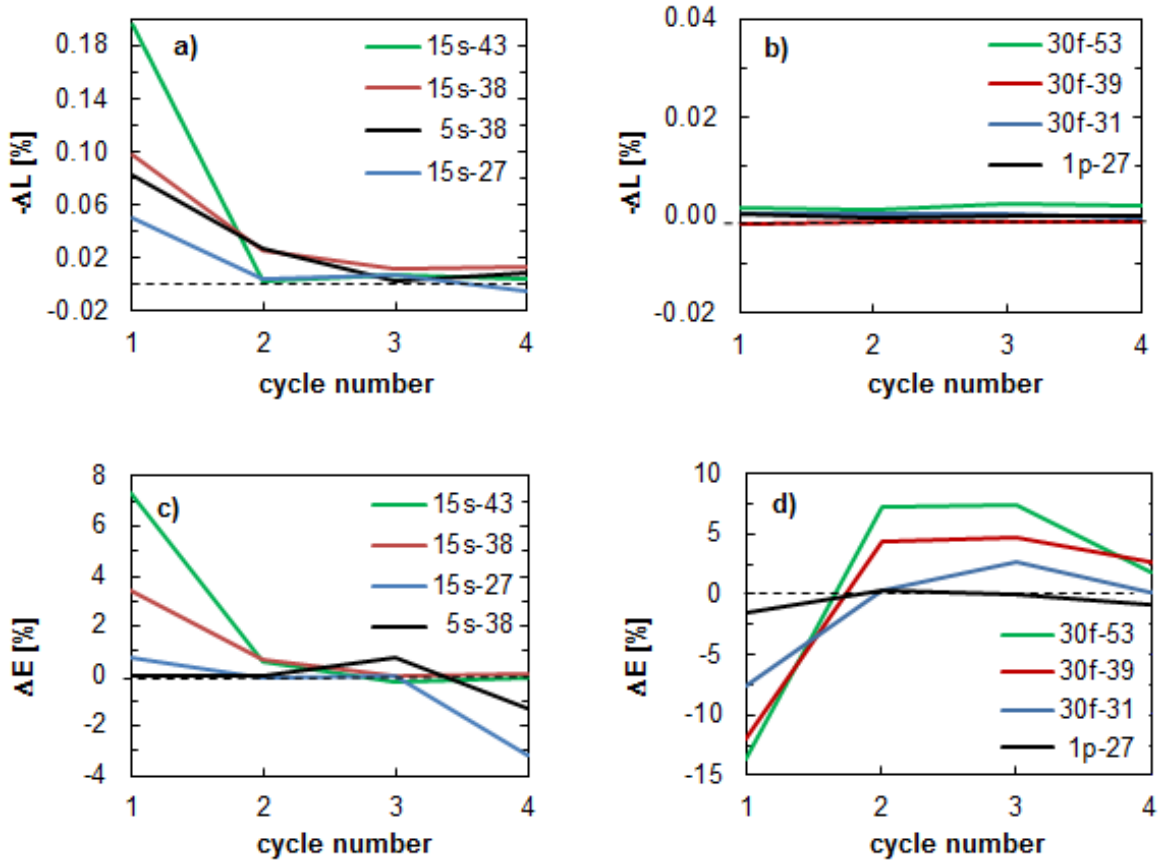

Figure 5.19: Shrinkage of samples after each thermal cycle for a) 5 and 15 μm samples and b) 1 and 30 μm samples. Change in Young's modulus after each thermal cycle for c) 5 and 15 μm samples and d) 1 and 30 μm samples. A dashed line at zero has been included.

after no change in the first two cycles, E increased 0.75 % after the third and decreased 1.3 % after the fourth cycle. The total changes in E after all four cycles for samples 15s-43, -38, -27 and 5s-38 were +7.6, +4.3, -2.4 and -0.5 %, respectively.

The change in Young's modulus of the 30f samples was quite different (figure 5.19 d)). In the first cycle the Young's modulus decreased by 13.6, 12.0 and 7.6 % for samples 30f-53, -39, and -31, respectively. In the second cycle, the E of 30f-53 and -39 increased by 7.2 and 4.4 %, and -31 remained constant. In the third cycle E increased by 7.4, 4.8 and 2.6 %, respectively. In the fourth cycle, the E of 30f-53 and -39 increased by 1.8 and 2.7 %, and -31 remained constant. The Young's modulus of 1p-27 remained relatively constant with only small decreases in the first and last cycle of 1.5 and 0.9 %. The total changes in E after all four cycles for samples 30f-53, -39, -31 and 1p-27 were +1.3, -1.2, -4.8 and -2.1 %, respectively.

5.3.2 Thermal conductivity

The copper ligament diameter, copper content, residual porosity, measured thermal diffusivity, estimated heat capacity and calculated thermal conductivity of the samples tested with the transient method are shown in table 5.4. Table 5.5 shows the residual porosity and thermal conductivity of the samples tested with the steady-state method. In figure 5.20 a), thermal conductivity is plotted as a function of copper content and in b) as a function of copper ligament diameter for the samples containing approximately 40 vol.% copper. The values of thermal conductivity measured with both methods are included.

The thermal conductivity increases with increasing copper content (figure 5.20). In the 30f samples, conductivity increased from 48 to 69 W/m.K for an increase in copper content from 22 to 39 vol.%. In the 15s samples, conductivity increased from 46 to 154 W/m.K for an increase in copper content from 14 to 55 vol.% in the transient method, and from 58 to 99 W/m.K for an increase in copper content from 25 to 47 vol.% in the steady state method. All other samples were only single data points, but were consistent with the other samples. The change in thermal conductivity with copper content was similar for both methods of measurement.

The effect of copper ligament diameter on the thermal conductivity was not investigated in detail, since the copper contents and residual porosities of the samples with approximately 40 vol.% copper were not consistent enough (compare tables 5.4 and 5.5), with copper contents varying from 35 to 41 vol.% and the porosities from 0.7 to 13.9 %. The steady-state values varied minimally with ligament diameter. The transient values were more highly scattered, but also had more scatter in the copper content and residual porosity.

Table 5.4: Residual porosity, thermal diffusivity a, thermal capacity C_p and thermal conductivity λ of the samples tested with the transient method.

sample	vol.% porosity	a, mm^2/s	C_p, J/g.K	λ, W/m.K
1p-36	4.4	30	0.62	103
5s-40	0.7	32	0.60	114
15s-14	7.9	15	0.72	46
15s-41	0.3	27	0.60	96
15s-55	2.5	42	0.55	154
30f-22	1.8	14	0.67	48
30f-29	3.3	16	0.64	54
30f-39	1.5	19	0.61	69

Table 5.5: Residual porosity, and thermal conductivity λ of the samples tested with the steady-state method.

sample	vol.% porosity	λ, W/m.K
5s-32	8.0	63
5s-38	2.4	79
15s-25	5.4	46
15s-26	4.4	69
15s-36	13.9	67
15s-38	1.6	84
15s-38	1.8	84
15s-47	2.7	99
30f-35	7.4	77
30f-36	6.3	82

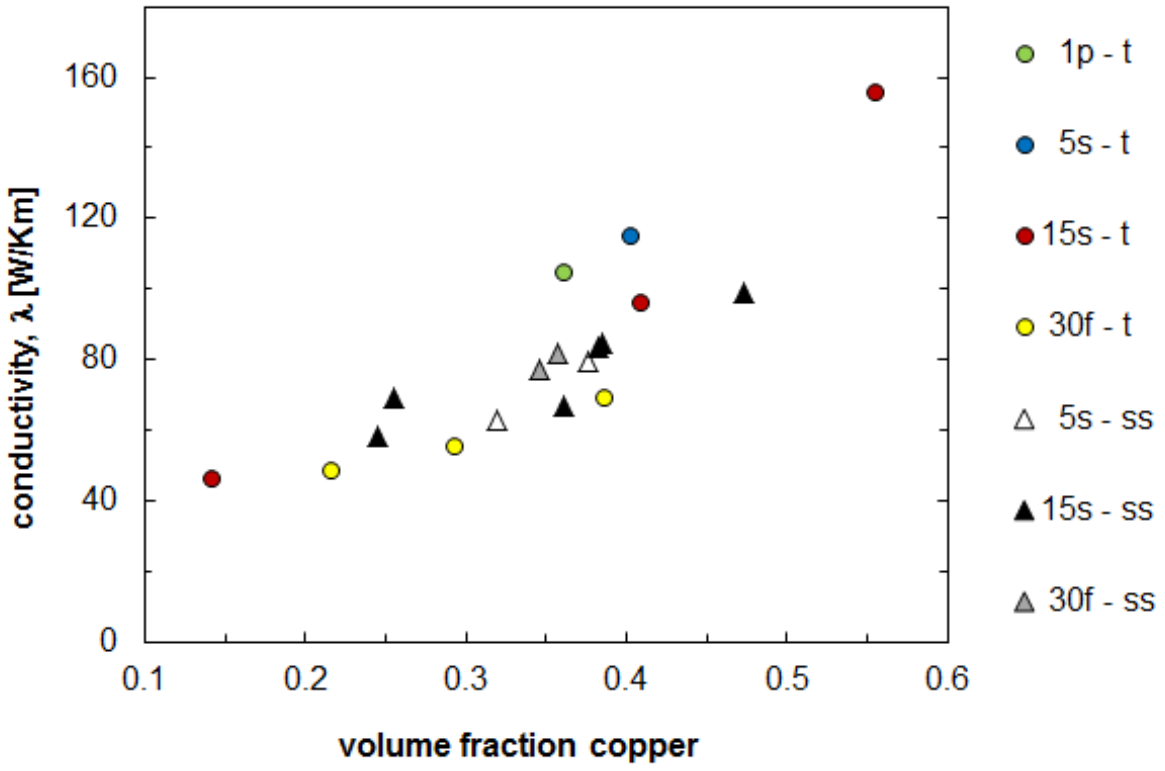

Figure 5.20: Variation of thermal conductivity with copper content measured with the transient (t) and steady-state (ss) methods.

5.4 Wear behaviour

Friction coefficient and temperature

Figure 5.21 shows four different representative data curves obtained during wear testing. Most samples had a data curve similar to figure 5.21 a) with a plateau in friction coefficient and temperature achieved by 30 to 100 m sliding distance. It was assumed that after 100 m a steady state had been achieved. In some samples, the curve of the friction coefficient had a zig-zag form (figure 5.21 c)). The samples where it occurred are: 1p-21, 1p-45, 5s41, 5s-50, 15s-20, -33, -38 and -55. In 1p-21 and 5s-50, this occurred in all three tests. In the other samples it only occurred in one of the three tests. This effect was not observed in tests under a 10 N load or in any 30f samples. There was no identifiable trend as to when this behaviour would occur. The friction coefficient of the 30f samples (figure 5.21 b)) had a different trend: a maximum around 100 m, then a minimum around 140 m, then a linear increase. The temperature had reached a plateau by a sliding distance of 100 m. In figure 5.21 d) it can be seen that alumina has a higher friction coefficient than copper, and that there is more noise in the curve.

In table 5.6, the average plateau values of friction coefficient and temperature of the alumina ball during testing are summarised. The colours of the wear track and wear debris are also included. There was a general increase in temperature with increasing friction coefficient. The temperature of the alumina pin was lowest against the 30f samples: 32 to 39 °C compared to 38 to 56 °C in all other composites, although they had a friction coefficient comparable to the other composites. The samples containing 20 vol.% copper (apart from 30f-20) had a higher friction coefficient than all the other samples: 0.8 to 1.0 compared to 0.5 to 0.7. The friction coefficient was even higher than in pure alumina against alumina (0.7 to 0.8). 30f-20 had less residual porosity and a lower friction coefficient of 0.7. The colours of the wear track and wear debris (table 5.6) indicate that oxidation of the copper had occurred. It was not possible to collect enough wear debris for this to be analysed under SEM or XRD.

Specific wear rate

Figure 5.22 provides the variation in specific wear rate as a function of copper content. The specific wear rate of the 30f samples was about an order of magnitude lower than the others (figure 5.22). The wear rate of the 30f samples increased from 1.1 to 1.5×10^{-4} mm^3/Nm for increasing copper content from 20 to 55 vol.%. Due to the size of the error bars, the trend for the 15s samples is not clear. There was a slight increase in average specific wear rate from 1.1 to 6.9×10^{-5} mm^3/Nm for increasing

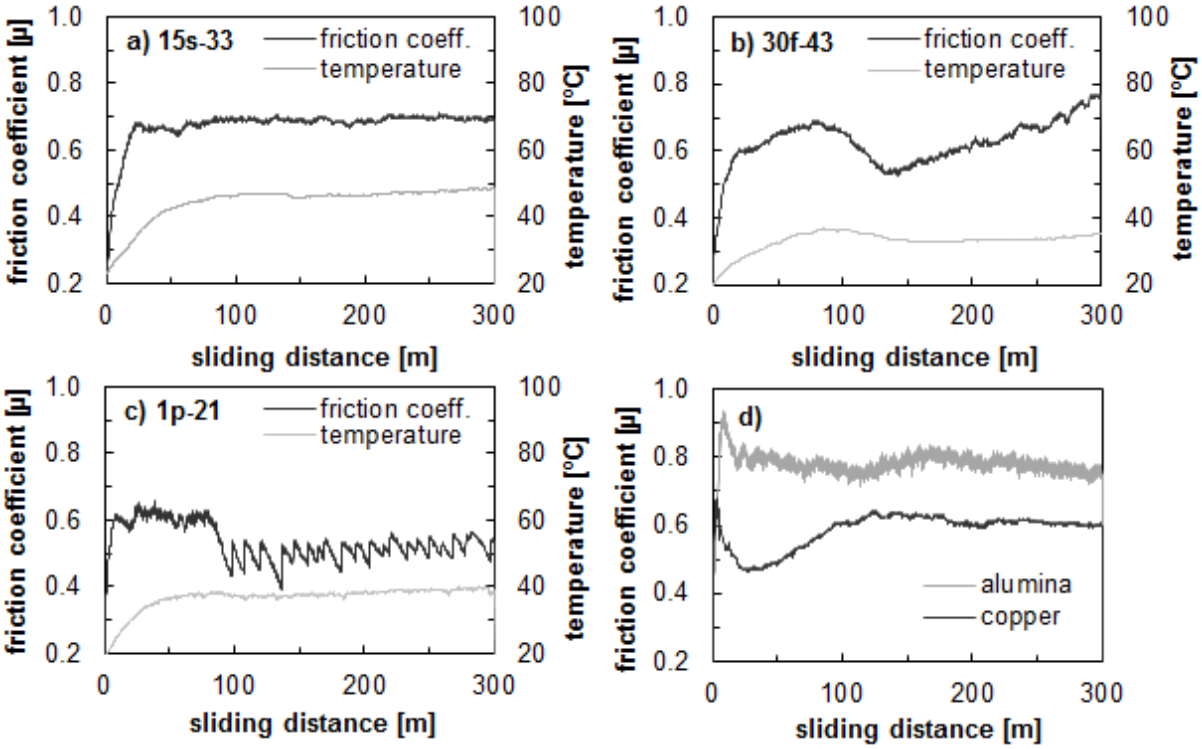

Figure 5.21: Friction coefficient and temperature as a function of sliding distance. Representative graphs of a) sample with a steady state plateau, b) 30f samples, c) samples showing cyclic tribolayer behaviour, d) alumina and copper, without temperature.

Table 5.6: Friction coefficient (μ) and temperature (T) of the alumina ball during testing. Colours of the wear track and debris after testing.

sample	μ	T, °C	wear track	wear debris
Al_2O_3	0.7-0.8	35-40	white	white
Cu	0.6	30-35	black	black+copper
1p-20	0.8	49-56	green+black	green+grey
1p-26 to 45	0.6-0.7	38-52	grey+black	grey
5s-20	0.9-1.0	42-47	green	green
5s-28 to 50	0.5-0.7	38-45	grey+green+black	grey
15s-20	0.8-1.0	48-51	grey	green+grey
15s-33 to 51	0.6-0.7	44-50	green+black	grey
30f-20 to 55	0.6-0.8	32-39	grey+white	green+grey

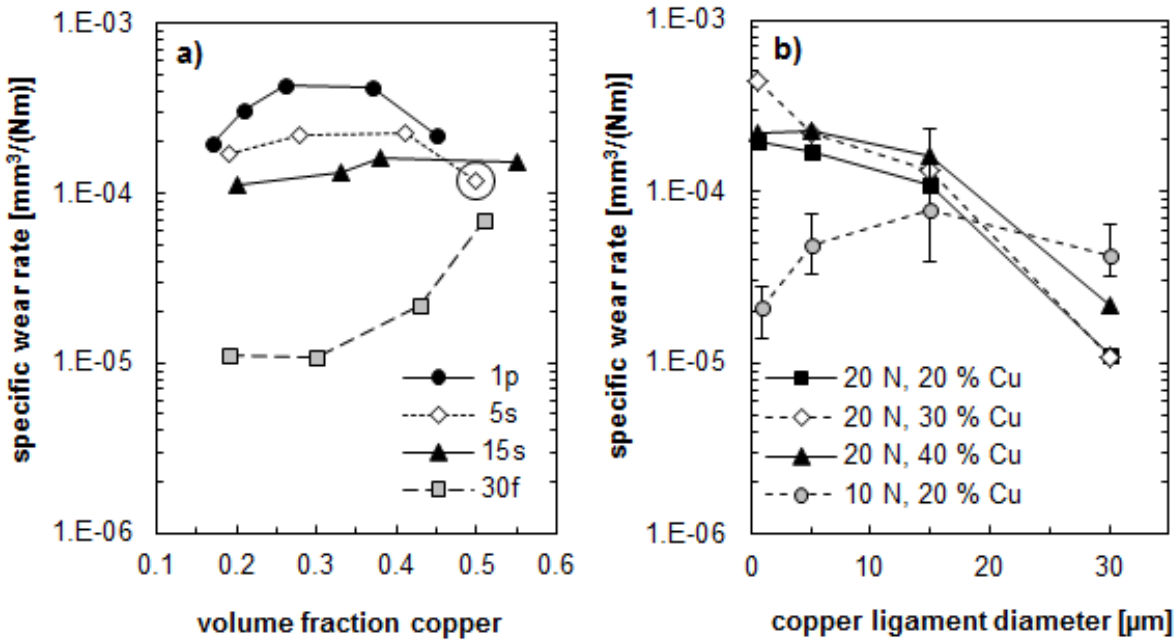

Figure 5.22: Specific wear rate as a function of a) volume fraction Cu (legend showing sacrificial preform used), b) Cu ligament diameter (legend showing contact load and volume percent copper). The encircled data point marks the only sample where cyclic tribolayer behaviour occurred in all three tests.

copper content from 19 to 51 vol.%. With increasing copper content from 19 to 28 vol.% wear rate of the 5s samples increased slightly from 1.7 to 2.2×10^{-4} mm^3/Nm, then stayed constant up to a copper content of 41 vol.%. With a further increase to 50 vol.%, the wear rate decreased to 1.2×10^{-4} mm^3/Nm. The 1p sample behaved similarly. Firstly there was an increase of wear rate from 2.0 to 4.4×10^{-4} mm^3/Nm for increasing copper content from 17 to 26 vol.%, then a plateau until 37 vol.% Cu. With a further increase to 45 vol.%, the wear rate decreased to 2.2×10^{-4} mm^3/Nm.

Figure 5.22 b) demonstrates the role of the copper ligament diameter. For the tests under a 20 N load, the wear rate decreased significantly an order of magnitude from 1.1×10^{-4} mm^3/Nm down to 1.2×10^{-5} mm^3/Nm with increasing copper ligament diameter from 1 to 30 μm. The results were quite different for the samples with 20 vol.% Cu tested under a 10 N load. Increasing the copper ligament diameter from 1 to 15 μm increased the wear rate from 2.1 to 7.8×10^{-5} mm^3/Nm. Upon a further increase in copper ligament diameter to 30 μm, the wear rate decreased from 7.8 down to 4.3×10^{-5} mm^3/Nm. In general the samples tested at the lower load had a lower specific wear rate, except for the 30f-20 sample in which the specific wear rate was higher at the lower load.

Wear mechanisms

Three dimensional images of the wear tracks generated from the white light microscopy are shown in figure 5.23. A representative selection of the wear tracks examined in the SEM are shown in figures 5.24, 5.25 and 5.26. From these images the following wear mechanisms were identified: The copper samples showed adhesive wear with extensive plastic deformation, evidenced by smearing at the edge of the wear track (figures 5.23 a) and 5.24 a)). Alumina has undergone abrasive wear (figures 5.23 b) and 5.24 b)) shown by the mixture of smooth and rough areas without any smearing. The smooth areas are due to the polishing effect at the start of the wear test. The damaged layer formed during this polishing stage is fatigued with further sliding distance. Microcracks formed (similar to figure 5.26 b), lowest image) and parts of the damaged layer spalled, revealing angular alumina grains on the fracture surface.

The wear tracks of all partially sintered and starch based samples (apart from 5s-20 and 15s-20) looked similar, shown representatively in figure 5.23 d) to f), i), j) and figure 5.25 b). The dark, smooth areas in the SEM image are a crushed mixture of alumina, copper and copper oxide. The smearing of this layer indicates adhesive wear. This damaged layer also spalled. The surface revealed below shows very fine spherical particles characteristic of oxidative wear [95]. Samples 5s-20 and 15s-20 underwent abrasive wear, as depicted by the wear tracks of 15s-20 in figure 5.23 g) and 5s-20 in figure 5.25 a), where a uniform roughness without any smearing is shown. Most 30f composites underwent a mixture of abrasive and oxidative wear (figures 5.23 j), k) and 5.26 a)). The wear tracks of the 30f samples all looked similar to figure 5.26 a) except 30f-55, in which smeared regions indicate adhesive wear (figures 5.23 l) and 5.26 b)).

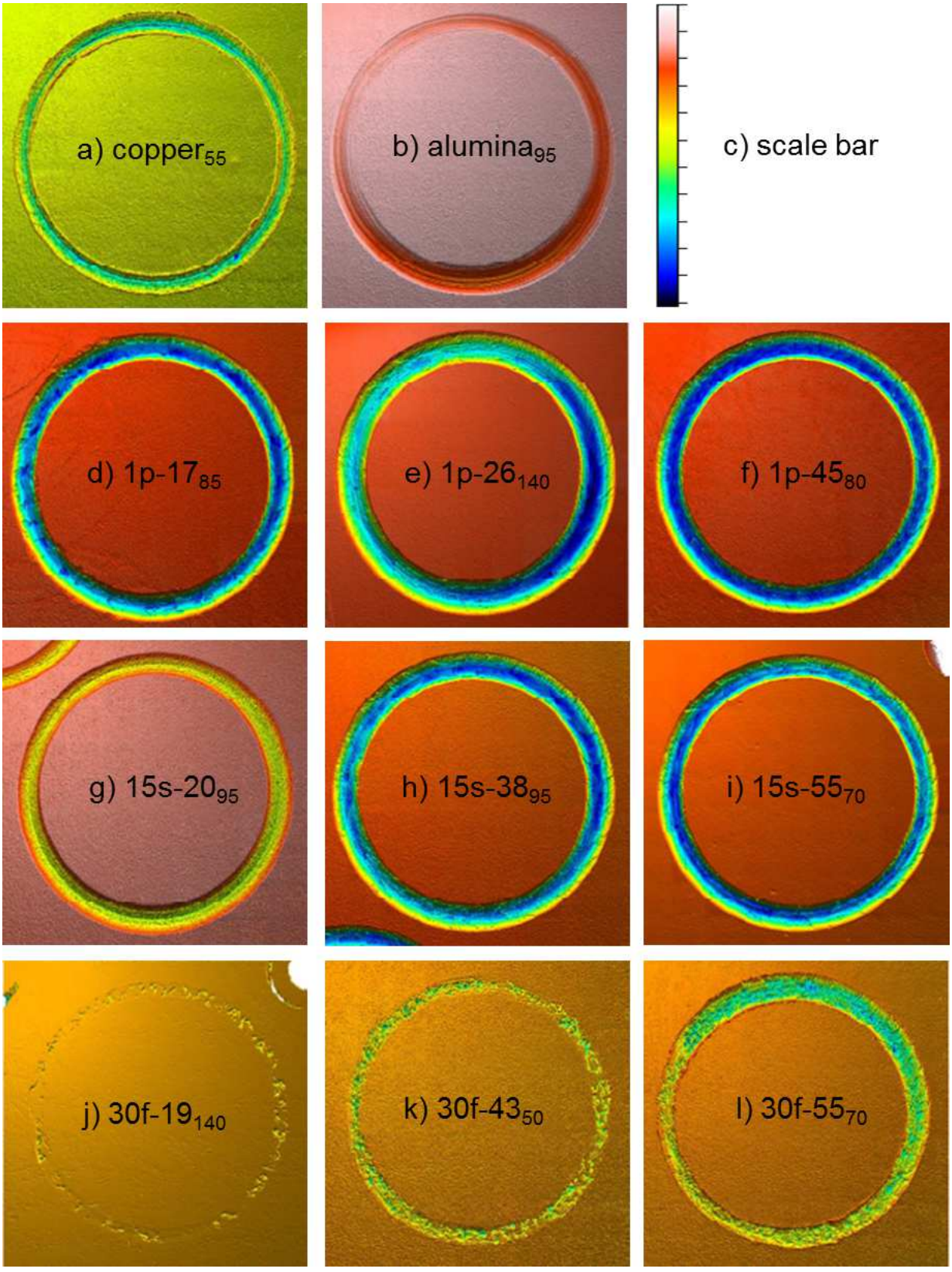

Figure 5.23: Three dimensional images of wear tracks under a 20 N load, direction of wear clockwise. Generated from white light microscope profilometry. The colour scale bar used to illustrate the depth is shown in c). Beside each letters is the sample name with the number in subscript representing the maximum on the scale bar in μm.

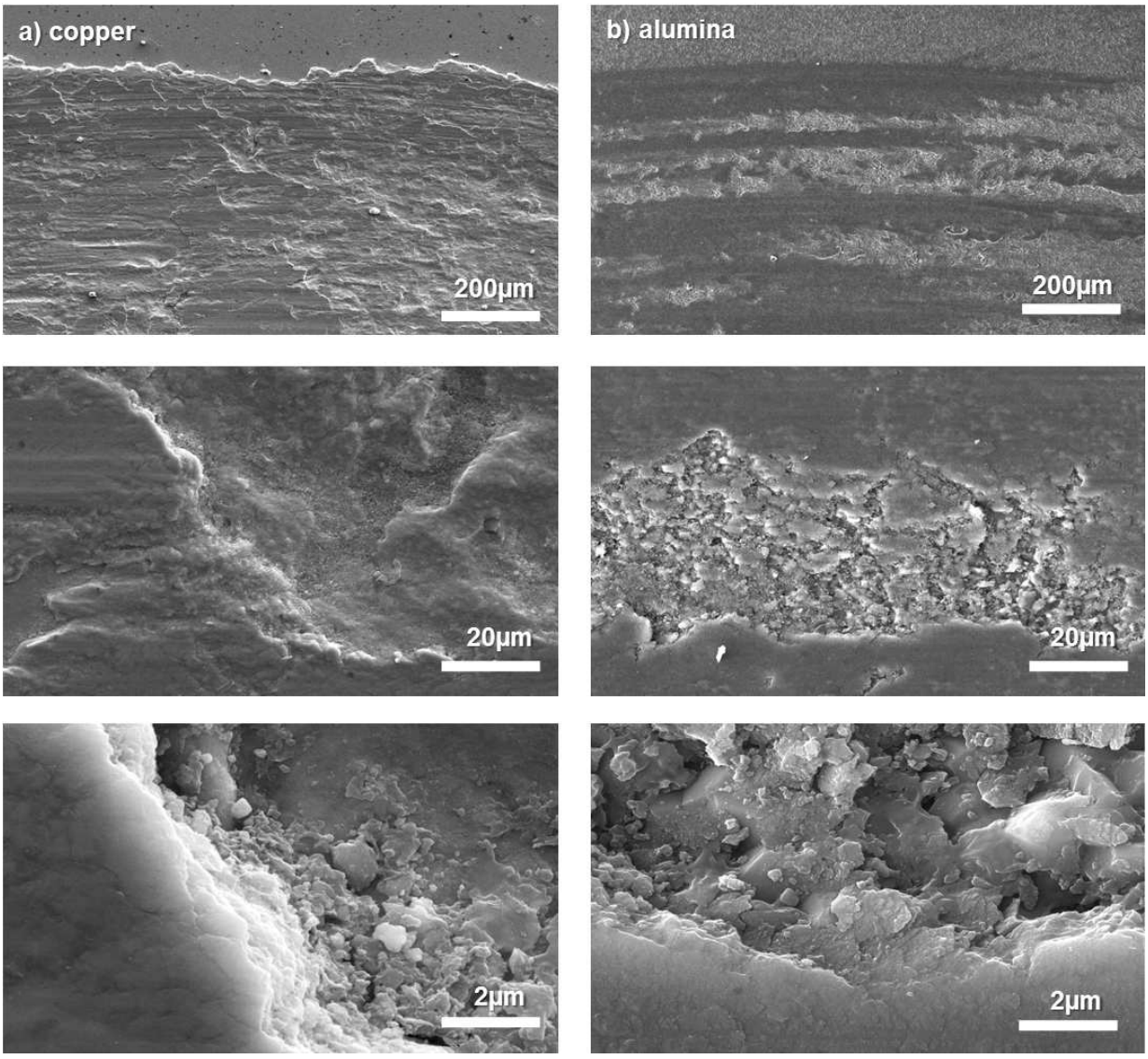

Figure 5.24: SEM images of wear tracks under a 20 N load, direction of wear from left to right: a) copper, b) alumina.

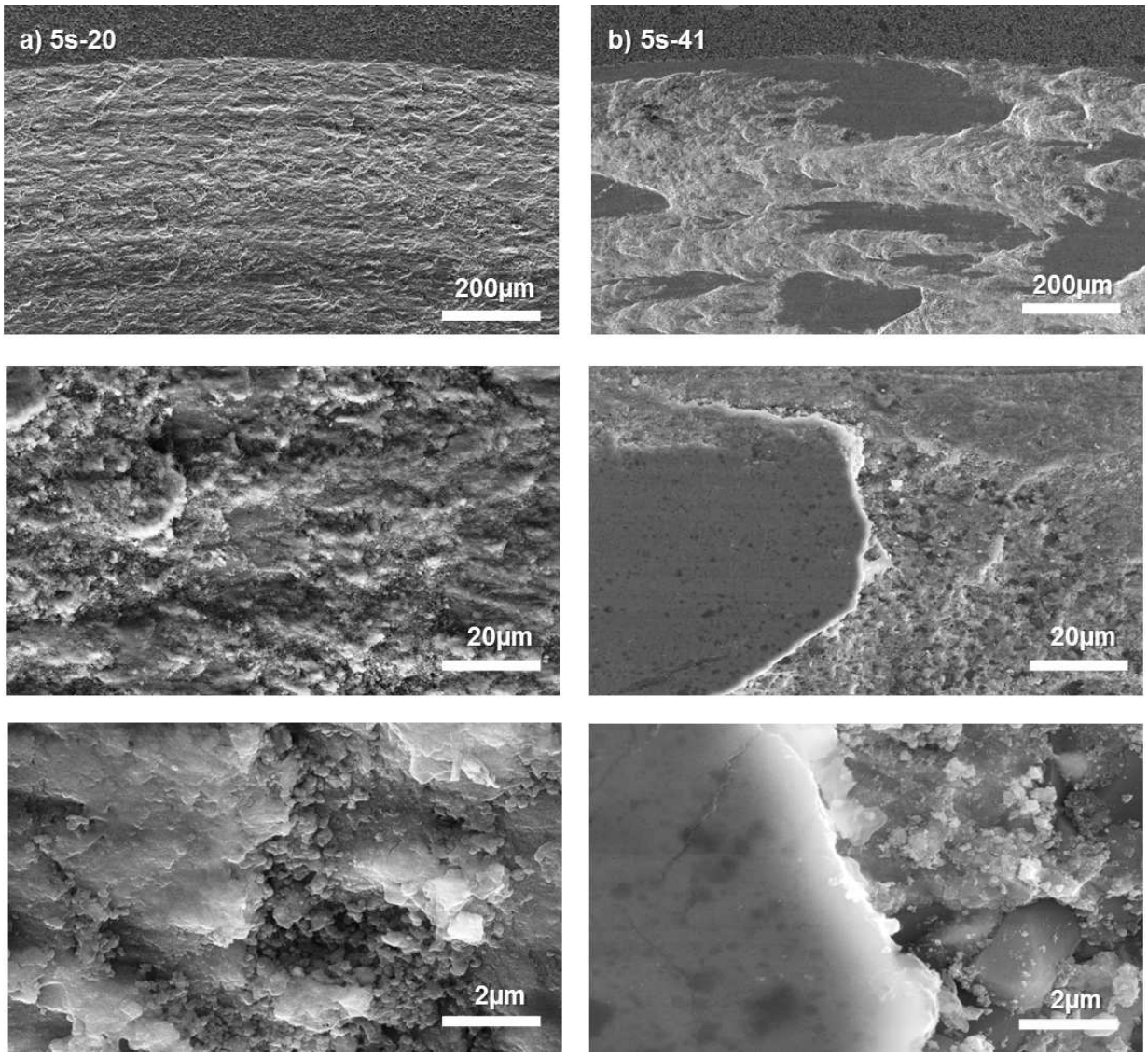

Figure 5.25: SEM images of wear tracks under a 20 N load, direction of wear from left to right, 5s samples with: a) 20 vol.% Cu and b) 41 vol.% Cu.

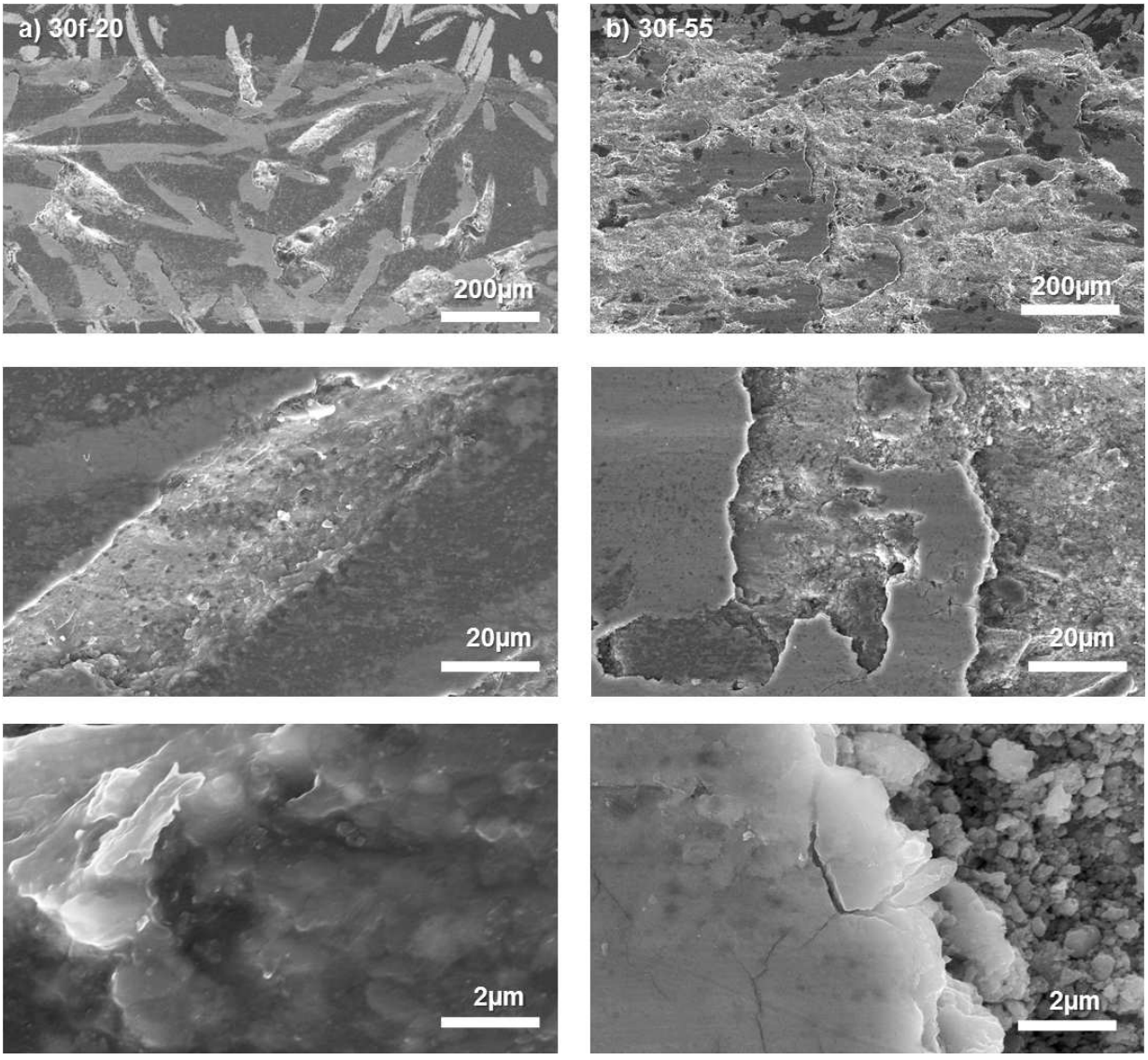

Figure 5.26: SEM images of wear tracks under a 20 N load, direction of wear from left to right, 30f samples with: a) 20 vol.% Cu and b) 55 vol.% Cu.

6 Discussion

6.1 Microstructure and composition

6.1.1 Porous alumina preforms

The resulting pore sizes of the porous ceramic preforms (table 5.1) were equal to the dimensions of the sacrificial preforms used. Shrinkage during drying and sintering, thus, did not lead to a decrease in the pore size. The significance of the open and closed porosity (table 5.2) is that open porosity is able to be infiltrated with copper, whereas closed porosity, by definition, is not. The high closed porosity in the 5s and 15s samples was due to there not being enough starch particles in the slurry for all of them to be touching. Isolated starch particles would have led to isolated, closed pores. The pore structure of the partially sintered and wool based samples was more permeable than the starch based samples, as shown by the much lower closed porosity. This was due to the pore windows of the 5s and 15s samples being approximately 20 % of the size of the pores. Although the pore window size of the wool based samples was also relatively small (4.7 μm), the high permeability was given by the long, continuous fibres of almost constant diameter.

Sample 30f-50 had relatively high amount of closed porosity of 8 %, compared to the other 30f samples, with 0 to 1 %. Now, the residual porosity of the composite must be equal to or higher than the closed porosity. However, since the 30f-50 composites did not have such a high residual porosity, the samples had not infiltrated with water for long enough, meaning that the value for open porosity was in fact close to the total porosity.

The total porosities were in general within 3 % of the target porosity, with the exceptions of 1p-30 with 6 % more and 5s-30, 15s-50 and 30f-20, all with 4 % more open porosity than the target. The wool felt used to produce the 30f samples did not have an entirely constant volumetric density, explaining the variation in the 30f samples.

The starch slurries must not have been entirely homogeneous despite careful mixing and stabilising practices, as well as a high solid content. Since starch has a density lower than alumina (1.50 compared to 3.96) the starch was prone to float to the top of the slurry when standing even for short periods of time. This may have been the cause of the variation in density of the 5s and 15s samples.

There were two different ovens used for the partial sintering of the 1p samples. It was assumed that the temperature displayed was the same in both, since the same type of thermocouple was used and the placement within the furnace the same. However, there must have been enough variation in the temperature to cause up to 6 % variation in the density (from the sintering curve in figure 3.4 equivalent to 40 to 70 °C). Either that, or the sintering behaviour of the plates for infiltration (approximately 60 x 60 x 4 mm^3) was different to that of the small cylindrical samples used to make the sintering curve (diameter 20 mm, thickness 2 mm). But since not all 1p samples had a higher porosity than expected, the first reason is more plausible.

6.1.2 Composites

When comparing table 5.2 and table 5.3, it can be seen that there is an inconsistency between the porous ceramics and the composites. The copper content of the composites should coincide with the open porosities of the respective porous ceramic preforms, and the residual porosity of the composite with the close porosity of the ceramic preform. There are a few reasons for this. Firstly, since the the porous ceramics were not infiltrated with water for long enough, this gave a higher value for closed porosity than was actually the case. Secondly, the density of the porous ceramics was measured on whole plates, whereas the density of the composites mostly on smaller samples such as bending bars. The plates often had a more dense layer on the surface, where the porosity was more likely to be closed. After infiltration, this layer was ground away since it was generally not fully infiltrated. This explains why the porosity of the composites was often less than expected from the calculated closed porosity of the porous ceramic preforms. There was also a variation in porosity from sample to sample, and even within the one sample. Moreover, the density was not measured for every single sample, therefore, some statistical deviations may have been missed.

Inside some of the copper spheres in the 5s and 15s samples was a cluster of alumina, also seen in figure 5.1. This has also been observed by others [28]. This was due to the shrinkage of starch particles during the drying of the green body. The starch adhered to the alumina powder around it, and upon shrinking during drying and pyrolisation pulled some alumina particles into the centre of the resulting pore. These particles then sintered together during the pyrolisation and sintering steps to form an agglomerate. This phenomenon could have also reduced the permeability of the 5s and 15s samples, since the loose alumina clusters may have blocked a pore window during infiltration, as found by Mattern [28].

6.2 Mechanical properties

6.2.1 Young's modulus

In figure 6.1, the experimental and FEM results are compared with the Voigt and Reuss bounds of the rule of mixtures (RoM) and the Hashin-Shtrikman (HS) bounds. The decrease in Young's modulus (E) with increasing copper content is consistent with predictions from RoM and the HS bounds (figure 6.1). The FEM values lie along the upper HS bound. The RoM boundaries represent the maximum and minimum energetically possible composite E values. The HS bounds represent the maximum and minimum values of E for isotropic composites [60], based on a structure of a matrix with isolated inclusions (figure 2.5 b)). The upper boundary is when the stiffer phase is the matrix (CMC), the lower bound when the less stiff phase is the matrix (MMC). Since alumina is continuous in the composites, one would expect the values of Young's modulus to lie along the upper HS bound. Assuming a strong interface, the continuous alumina network would exercise constraint upon the copper network such that a situation of constant strain would be expected. Indeed, the FEM values of E do lie on the upper HS bound. In the finite element model, the interface is assumed to be perfect and there are no processing defects or residual porosity. In this idealised case, the FEM values of E fit the HS model.

The experimental values, however, are lower. Most data points lie between the lower HS bound and the Reuss bound. This is most likely due to residual porosity, processing defects and a weak interface between the copper and alumina. The value of one data point below the Reuss bound is not a physical impossibility, but rather reflects the fact that residual porosity had not been included in the calculation of the RoM boundaries. The samples of the data point had an average porosity around 5 %. If the Reuss bound is recalculated for a three phase composite with 5 % porosity, the bound shifts downwards such that this data point is above the bound.

Since the 1p, 5s and 15s samples are macroscopically isotropic, the data points should fit within the HS bounds, however, this is only the case for three of them. This is, again, due to residual porosity not being taken into account in the calculation of the bounds. Moon et al. [54] found E of alumina-aluminium interpenetrating composites with an Al content between 5 and 95 vol.% to lie within the HS bounds. This system has a stronger interface than alumina-copper.

One system with a weak interface is alumina-Ni_3Al. Skirl et al. [53] found E with varying Ni_3Al content to be below that even of the lower rule of mixtures [53]. This was attributed to microcracking between the Ni_3Al and Al_2O_3. Clearly the strength of

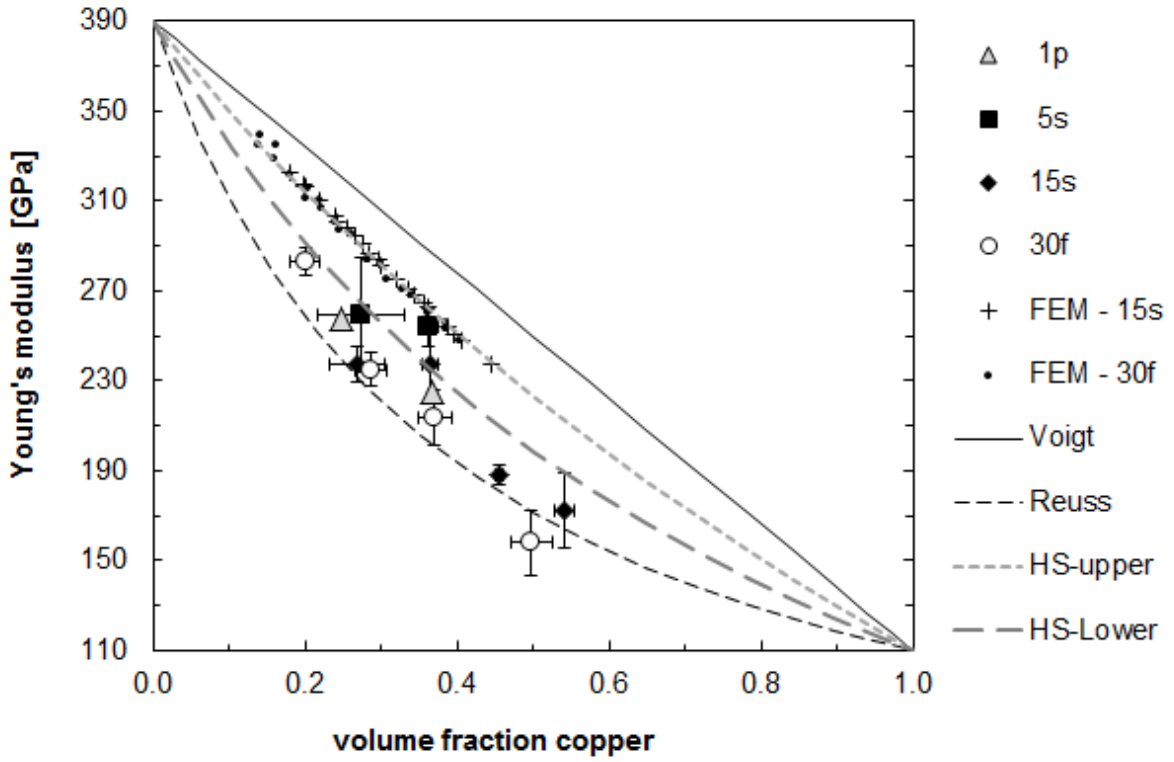

Figure 6.1: Experimental and FEM values of Young's modulus of different alumina-copper composites compared with the Voigt and Reuss bounds of the rule of mixtures (RoM) and the upper and lower Hashin-Shtrikman (HS) bounds.

the interface between the two phases has a significant influence on the composite E, with low interface strengths reducing E.

In the samples with more scatter, in particular 5s-22, E was generally higher for higher copper contents, opposite to the general trend. This was because lower copper contents were due to residual porosity (E=0) and not alumina (E=390 GPa) replacing copper (E=110 GPa). Infiltration was incomplete for the samples with a lower copper content with residual porosity lowering E significantly.

Considering the data points around 38 vol.% Cu (figure 6.1, E appears to decrease with increasing copper ligament diameter from 5 to 15 to 30 μm. Analytical and numerical models do not predict a change in E with metal ligament diameter. It may be that the interface strength decreases with increasing copper ligament diameter. This was found by Knechtel et al. [1] when varying metal ligament diameter in alumina-aluminium and alumina-copper composites, abeit for a different range (0.08 to 0.75 μm). The value of E for a copper ligament diameter of 1 μm does not follow the above trend, but lies between that of the 15 and 30 μm data points. The partially sintered alumina network, however, is weaker than that of the fully sintered networks of the other composites, therefore a lower E would be expected.

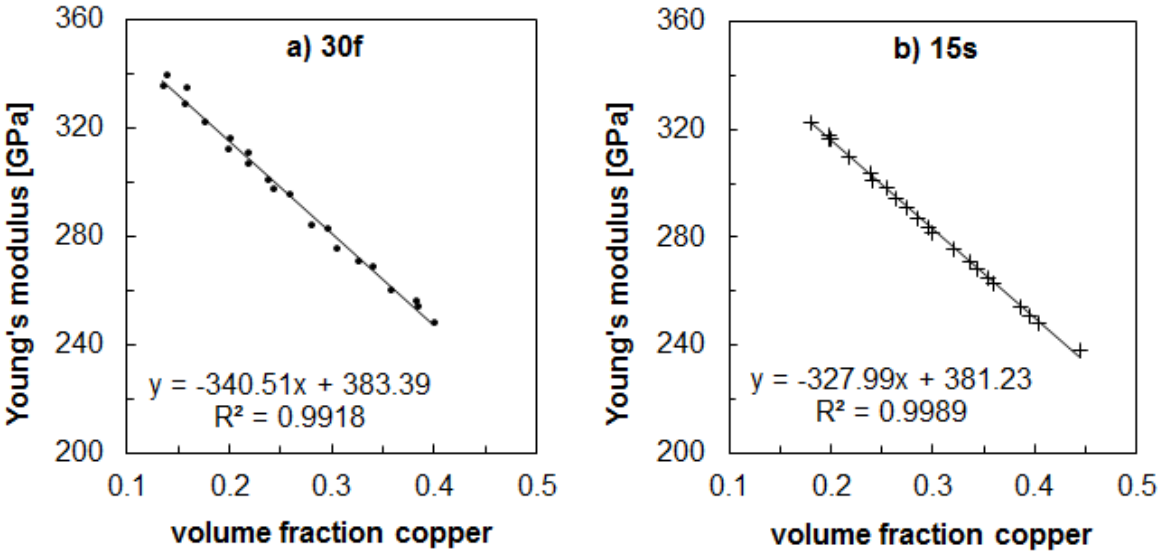

Figure 6.2: FEM values of Young's modulus of a) 30f and b) 15s with a linear fit to display the amount of scatter in the data.

Brezny et al. [27] found E of porous ceramics to be independent of pore size when the shape of the porosity stayed the same. Moon et al. [54] and Mattern [28] found E of alumina-aluminium composites to be independent of metal ligament diameter and shape. A further study would, therefore, need to be conducted in order to confirm the effect of metal ligament diameter on E in alumina-copper composites. For example, composites where only the metal ligament diameter is varied and not the metal ligament shape or metal content could be tested. Some possibilities include partially sintering different alumina grain sizes, or using different types of starches or different sizes of polymer spheres as sacrificial preforms.

In figure 6.2, the scatter in the values of E from the FEM simulation is shown. The amount of scatter in the 30f sample is higher than the 15s sample, and the amount of scatter in 30f decreases with increasing copper content. The structure of 30f is more coarse and is rather anisotropic, compared to the isotropic structure of 15s. This makes the structure less homogeneous, hence the increased scatter in the E values. The more copper in the 30f samples, the more homogeneous the structure and the less scatter in the E values.

6.2.2 Hardness

In figure 6.3, the measured hardness is compared to the Voigt and Reuss bounds of the rule of mixtures. It is debated whether the RoM can be applied to non-elastic properties [118]. However, in a paper discussing this very issue, it was found that FEM and experimental values fit within these bounds [119]. The experimental values of hardness fit within the rule of mixtures. For lower copper contents the values are in the middle of the bounds, and for higher copper contents the values approach the lower bound.

The decrease in hardness with increasing copper content (figure 5.5) is as expected, since copper is soft (HV = 0.49 GPa) and ductile, whereas alumina is hard (HV = 13.39 GPa) and brittle. At higher copper contents, the alumina forms a relatively weak network. As a result, sliding of alumina grains is able to take place under the indenter and plastic flow of the metal phase occurs [6]. As the copper content decreases, the alumina network becomes stronger, hindering plastic deformation in the copper. This leads to the rise of hydrostatic stresses below the indenter, which significantly increases the resistance of material to indenter penetration. In figure 5.5 it can be seen that the strength of the alumina network is higher at copper contents below 30 vol.%, evidenced by the sharp increase in hardness. Above 30 vol.% copper, the decrease in hardness is less pronounced. This would suggest that there is a percolation threshold around this copper content, above which sliding of alumina grains and, thus, plastic flow of copper is possible.

The partially sintered (1p) composites have lower hardness values than the others due to the relatively weak bonding between alumina grains: there are only small points of contact between individual alumina grains in 1p samples as opposed to fully sintered alumina grains surrounding a porous network due to the sacrificial preform in the 5s, 15s and 30f samples. The maximum hardness values are observed in the 15s-20 5s-20 materials, despite containing a distinctive amount of residual porosity (8-10 %). The high alumina content appears to have a dominant effect on the hardness, and not the residual porosity.

The coarser alumina network of the 15s composites is presumably stronger than that of the finer 5s composites, leading to the somewhat higher hardness values observed. But the difference between these two curves is minimal. According to this argument, the 30f samples should be the hardest, but this is not the case. It is not clear whether this was only due to error in measuring the size of the indentation due to spalling around the indentations, or some other reason. A minimal amount of copper-filled cracks (most likely shrinkage cracks) was observed in SEM images of polished surfaces. The cracks

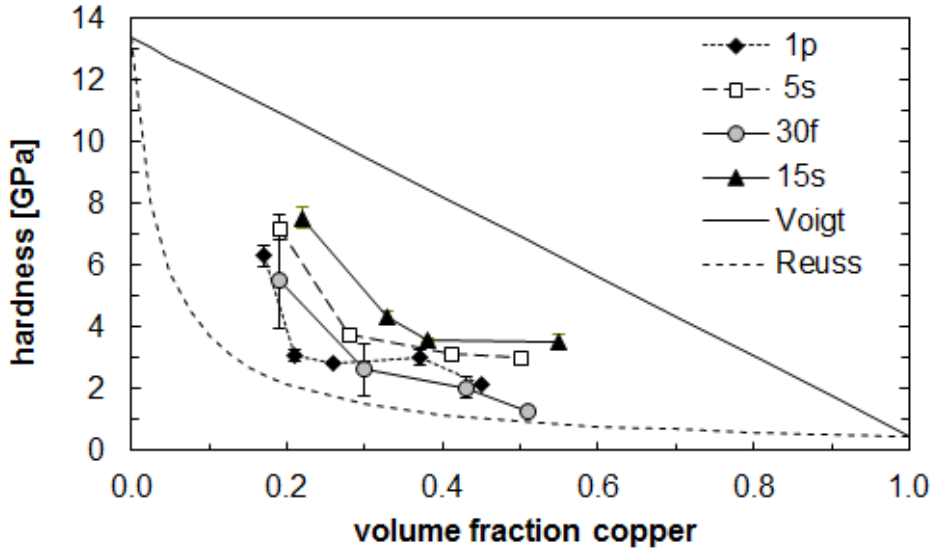

Figure 6.3: Vickers hardness as a function of copper content, compared with the Voigt and Reuss bounds of the rule of mixtures.

could weaken the ceramic network, but must be near the Vickers indentation to have an effect on the hardness value. Retesting the hardness of the 30f samples with a lower load to avoid cracking and spalling would have meant that the indentation was no longer representative of the sample, with either a dominance of copper or alumina making the results inaccurate. Alternatively, if the 30f samples had the highest concentration of microcracking between copper and alumina, under the indenter the copper would first plastically flow to fill the microcracks before hydrostatic stress could build up. Hence, there would be less resistance to the indenter initially, allowing a larger indentation and a lower hardness value.

6.2.3 Fractography and bending strength

Fractography

The fracture causing flaws shown in figure 5.8 were formed during the processing of the composites. The large, spherical copper regions (figure 5.8a)) originated from large pores in the ceramic preform. Any air bubbles trapped in the slurry must have remained after drying and sintering and then have been filled with copper during infiltration. A longer evacuation of the slurry was adopted to prevent this sort of defect. Areas of residual porosity (figure 5.8 b)) came either from the porosity in that region being closed, or the copper infiltration time not being long enough. The regions of residual porosity act as large failure inducing flaws, since the region of porous alumina has a much lower strength than the copper reinforced alumina. The infiltration time was increased to minimise this problem.

Abnormally large alumina grains (figure 5.8c)) may have been due to local impurities in the slurry. The reason is not clear, however, the slurries were milled and sieved in order to destroy any stubborn agglomerates and remove solid impurities. The carbon flakes found within the composite structure (figure 5.8d)) were the most unexpected fracture causing defect. Since they were found within the volume (on the fracture surface) and not just on the surface (at the edge of fracture surface), they could not have been due to impurities introduced during the machining of the composites. It is suspected that the pyrolisation of the sacrificial preform was incomplete. But the carbon flakes were actually much larger than the pores formed from the sacrificial preform, so it is uncertain if this was really the cause. Nevertheless, after this was found, the pyrolisation stage was increased from 2 to 12 hours in order to avoid residual carbon in the composite.

In order to eliminate machining defects as seen in figure 5.8 e), subsequent cutting and grinding was conducted with finer blades and grinding wheels, and the initial polishing stages carried out for longer. The large structural defect seen in figure 5.8 f) was only observed once. It is clearly not an air bubble and looks like it may have been formed in the green body, possible due to have being disturbed during the drying stage. Extra care was then taken not to disturb the green bodies during drying.

In the 30f samples, no obvious fracture causing defects were found (figure 5.9). The copper ligaments were so coarse compared to the size of the bending bars that this is not surprising. The interfaces between copper and alumina along the surface under tension were most likely where fracture began. Nevertheless, there are some interesting features revealing more details about the microstructure than had been observed in the SEM images of polished surfaces. The pull-out of fibres up to several millimetres (figure 5.9 a)) shows there is a weak interface strength between the copper and alumina. The scaled surface of the wool did not have the anticipated effect of enhancing the interface strength mentioned in (section 3.1). The dimples along the surface of the copper fibre (figure 5.9 b)) are due to the poor wetting of copper on alumina. The higher thermal expansion coefficient of copper, combined with the weak interface strength, allowed the copper to partially pull away from the alumina during cooling after infiltration.

The flakes of copper (figure 5.9 c)) are shrinkage cracks, formed during drying or sintering, filled with copper during infiltration. Care was taken to avoid shrinkage cracks, however this was not fully eliminated in the 30f samples. The high ductility of the pure copper is seen in the extensive plastic deformation visible in figure 5.9 c). The copper ligaments have stretched and necked considerably before fracture. Even the slip planes of dislocation movement are clear to see at the tips of the fractured copper fibres.

Bending strength and Weibull modulus

Due to the difficulty in sample preparation, the number of test samples was limited to a maximum of 10 specimens per composition. The ASTM standard [120] recommends at least 10 samples for the calculation of an average value and at least 30 samples for the calculation of the Weibull modulus. It was, however, found that a qualitative assessment of the effect of copper content could be elucidated with fewer measurements [53]. The bending strength of the composites generally increased with increasing copper content, consistent with other works exploring the variation of bending strength with metal content in interpenetrating composites [6, 32, 53]. The bending strength of 5s-44 being lower than 5s-38 may have been within statistical deviation, given the size of the error bars. But in the 15s samples, the samples with 47 vol.% Cu had a much lower bending strength than the samples with 40 vol.% Cu, and both of these sample sets had more than 10 samples, enough to be statistically significant. In the samples with the higher copper content, the fracture causing defect was typically a region of residual porosity. The amount of residual porosity (4.5 %) was higher than in 15s-40 (0.5 %). So although the copper content was higher, the presence of residual porosity had a stronger detrimental effect. The region of porosity acted as a large, fracture causing defect, thus lowering the strength.

The values of bending strength in this work were rather low. The bending strength of a dense alumina (grain size 4 μm) was found by others to be 370 $\pm$ 50 MPa [32]. Introducing porosity, or a second phase, essentially introduces more and larger fracture causing flaws: the pores or the phase interfaces. The bending strength of porous alumina of 25 and 35 vol.% porosity was found by Prielipp et al. to be [32] 140 $\pm$ 10 and 70 $\pm$ 10 MPa, respectively. Bending strength decreases with increasing porosity, however, in this work was found to increase with increasing copper content. At some point, the copper compensates for the detrimental effect of the porosity. The 15s-25 sample had a bending strength of 140 MPa - the same as the porous alumina with a porosity of 25 %. Here, the copper has had no beneficial effect. In the sample with 38 to 40 vol.% Cu, the bending strength had increased significantly to 250 to 300 MPa, a significant improvement on the strength of the porous alumina with 35 % porosity, 70 MPa. For an alumina-aluminium composite it was found that the infiltrated pores no longer act as fracture-causing defects, but rather as crack bridging elements [121], whereby the bending strength was found to be independent of the metal ligament diameter.

Prielipp et al. [32] found the bending strength of alumina-aluminium composites with 10 to 40 vol.% Al and 0.08 to 0.75μm Al ligament diameter to be approximately 700 to 800 GPa: much higher than the values measured for alumina-copper in this work, however the metallic network in this work was much coarser: 5 to 30 μm metal

ligament diameter. In another paper [121] the bending strengths of alumina-aluminium composites with 15 to 35 vol.% and 80 to 500 μm Al ligament diameter were found to be approximately 300 to 450 GPa. Although that study had a coarser metallic network than this one, the bending strength values were still higher. Alumina-aluminium composites, however, have a much stronger interface than alumina-copper composites. Therefore, it is clear that interface strength also has a strong influence on the bending strength.

Relatively few experimental studies of the bending strength of alumina-copper composites have been presented in the literature. Travitzky et al. [7] found the bending strength of an alumina-copper composite with 15 vol.% Cu and 1 μm Cu ligaments to be 355 ± 20 MPa - significantly higher than the bending strength measured for lower copper contents in this work (90 to 210 MPa for 19 to 25 vol.% Cu). The copper network was finer that that tested in this work (5 to 30 μm). A coarser structure would be expected to have a lower bending strength, due to the presence of larger fracture causing defects.

The Weibull moduli of the 15s-40 and 15s-47 samples were 9.4 and 4.0, respectively. The first value is comparable to that of monolithic ceramics and that of alumina-Ni_3Al composites [53]. The presence of residual porosity had a detrimental effect not only on the bending strength, but also caused a higher scatter in the data (lower Weibull modulus), reducing the reliability of the samples. These Weibull moduli are low compared to alumina-aluminium composites, where values of up to 23.9 have been reported [53]. The higher interface strength of the alumina-aluminium system clearly has a beneficial effect on the Weibull modulus. It must be mentioned, however, that for all of these values, only 10 samples were used to calculate the Weibull modulus, contrary to the ASTM recommendation of at least 30 samples [120].

The processing of the composites was improved in an attempt to eliminate or minimise the typical fracture causing defects found. It would be expected that the values of bending strength and Weibull modulus would improve significantly, however after these changes the bending strength was not re-tested. Due to the destructive nature of the test and the large number of samples required, other characterisation methods were preferred for the improved composites.

6.2.4 Fracture toughness

Single edge V-notched beam (SEVNB)

a) Crack paths and fracture surfaces: The crack paths and fracture surfaces (figures 5.10 and 5.11) reveal information about the interface strength between alumina and copper, the strength of the alumina network, and the extent of plastic deformation before fracture in the different composites. The interface strength appears to be strongest in the 1p-25 sample (images a) and b)). There is limited delamination between alumina and copper in comparison to the other samples. In image b) it can be seen that the crack travels through an alumina grain when it could have travelled along an interface. Since the crack follows the path of least resistance, the interface must have been stronger than the alumina grain at this point. The fine copper ligaments do not tolerate as much plastic deformation as the other composites with coarser ligaments before fracturing. Since the alumina was only partially sintered with small points of contact between individual grains, the alumina network is less contiguous and thus weaker than in the other, fully sintered, composites.

The starch based samples (5s and 15s) both showed similar behaviour, with the small points of contact between copper spheres bridging the crack. The crack grows preferentially through the alumina network and along the alumina-copper interface. The copper bridges have tolerated more plastic deformation before fracture than in the 1p-25 sample. The alumina grains are faceted since they were fully sintered whereas in 1p-25 they were rounded since only partially sintered. The alumina network of the 5s and 15s samples is thus stronger than the 1p samples.

The wool based sample (30f) appears to have the weakest interface between alumina and copper. There is extensive delamination between the two phases, allowing the copper fibres to pull out and stretch significantly. These ductile bridges have tolerated the most plastic deformation before fracturing, with the largest crack opening achieved before the ligament fractured. The alumina grains are highly faceted since they were fully sintered. Thus the alumina network of the 30f samples was also stronger than the 1p samples.

b) R-curves: In the R-curves obtained from the SEVNB method, the only sample where a plateau was reached was 5s-26 (figure 5.12). In most samples no plateau in the R-curve was achieved, meaning that the crack length was too short for a constant number of copper ligaments to be bridging the crack during crack growth. It was not expected that the curves of 15s-39 and 5s-26 would follow such a similar path, since they have such a different copper content and ligament diameter, both of which should cause the R-curve of 5s-26 to have a much lower plateau. At a crack length of 2.5 mm the curves deviated from each other. 5s-26 reached a plateau, due to an equilibrium number of

copper ligaments bridging the crack. 15s-39 increased further, since the number of copper ligaments bridging the crack continued to increase. Moreover, at this point, well over 10 % of the total crack length was bridged (1.5 mm of 2.5 mm), rendering the calculation of K inaccurate. According to Zok and Hom [122], the equations used to calculate K are only valid for small-scale crack bridging. Large-scale crack bridging, that is, where the bridged zone of the crack approaches the total crack length, causes K to be overestimated. The curve of 15s-35 started lower than 15s-39, but rose more steeply to approach the other curves. Extrapolating the curve, it would appear to rise to a higher plateau, had the sample not broken prematurely. 5s-37 started well above the other curves and was less steep, but failed before the whole R-curve could be captured. There are too few data points to be able to meaningfully extrapolate the curve.

The R-curves of the 30f samples were higher with increasing copper content, although the curves overlap for 44 and 53 vol.% Cu. Up until a crack length of 2 mm the slopes of the curves are similar. Above this crack length, the scatter of the data makes it difficult to make any comparison, and again more than 10 % of the crack was bridged, invalidating the calculation of K. A plateau had not been reached in any of the curves, due to the weak interface and extensive plastic deformation of the ligaments allowing a wide crack opening before fracturing. Thus, further testing with CT samples was required.

Compact tension (CT)

In the 15s samples, the plateau value of K increased for increasing copper contents (figure 5.13 a)), as expected, since copper is much tougher than alumina (K_{IC} 70 to 80 [123] compared to 3 to 5 MPa$\sqrt{\text{m}}$ [124]). The crack length where the plateau value of K was achieved also increased, since for a particular ligament diameter, increasing the copper content means that the ligaments are closer together. Each individual ligament would have the same tensile strength and critical strain, and having more of them closer together would provide more resistance to crack growth.

In the 30f samples, increased copper led to a rise in the R-curve (figure 5.13 b)). There is, however, very little difference between the curves for 39 vol.% and 48 vol.% copper. This is unexpected, since theoretically, K must increase with increasing copper content. There may be a limit of toughening achievable with this microstructure. The plateau values of K were only achieved for copper contents of 22 and 28 vol.%; for the samples with higher copper contents, no plateau in the R-curve was achieved with the CT sample geometry used. The R-curves with these samples were remeasured up to a crack length of 12 mm. Above a crack length of 2 mm, K increased linearly with crack length. This was due to large scale crack bridging. When more than 10 % of the total crack length is bridged by ductile ligaments, the values for K become increasingly inaccurate [122].

Therefore, an even larger sample geometry would have been required to determine the plateau K value for these copper contents. This was not possible with the infiltration furnace used for production.

The data points in the 30f samples are further apart than in the 15s samples because of the larger distance between copper ligaments. During testing, crack growth was not stable. Upon increasing the load, the crack would suddenly grow quickly until it reached a copper ligament and stop. As soon as the start of crack growth was observed, the load was reduced to prevent further growth. After noting the new crack length and load, the load was again increased. Further crack growth then required a higher load up until the plateau of the R-curve was achieved. After that, lower loads were required. This procedure was the same for all composites, however, in the 30f samples, the alumina regions between copper ligaments were the largest, since the crack could 'jump' further before being stopped by a copper ligament.

The effect of copper ligament diameter of samples with approximately 40 vol.% copper ($\pm$ 2 vol.%) is shown in figure 5.13 c). Considering first samples 1p, 5s and 15s, increasing copper ligament diameter caused the slope of the R-curve and the plateau value of K to increase. These curves intersect at a crack length of around 1 mm. The copper content also increased by 1 % for each increase in ligament diameter, however, this small variation alone is not likely to cause such a change in the R-curve. Indeed, within one sample the copper concentration at any one location is likely to vary more than 1 %.

For a constant copper content, over a certain crack length there are either many fine copper ligaments close together, or few coarse ligaments further apart. As the crack grows into the finer structure, copper ligaments are met sooner and more are crossed within a short crack extension. This leads to a steep initial increase in K as the number of ligaments bridging the crack increases. Since the ligaments are fine, they can only tolerate a small amount of strain before tearing, such that an equilibrium number of ligaments bridging the crack, and hence a plateau in the R-curve, is soon reached. As the crack grows into the coarser structure, it must travel further until any ligaments are reached and the number of ligaments bridging the crack will be less than in the finer structure for a given crack length. Therefore, the R-curve starts lower and has a lower initial slope. The thicker ligaments can tolerate more strain and so the crack must grow further until there are an equilibrium number of ligaments bridging the crack and a plateau in the curve achieved. The thicker ligaments can also carry a higher load, such that the plateau of the R-curve is at a higher value of K.

For a ligament diameter of 30 μm, the R-curve is much higher than the other three curves. Here the copper network consists of long fibres with a relatively constant

ligament diameter. In comparison, the copper networks of the 5s and 15s samples consist of spheres connected by small windows of 1.3 and 2.0 μm, respectively (table 5.1). Since the crack follows the path of least resistance, it is the connecting windows rather than the widest part of the spheres that bridge the crack (also seen in figure 5.10 f)) and thus determine the R-curve behaviour. This would explain the small difference in the R-curves for the lowest three copper ligament diameters (effectively 1, 1.3 and 2 μm, respectively) and the large increase for the highest copper ligament diameter (30 μm).

6.2.5 Crack opening displacement

The crack profiles were extrapolated to the critical load (figure 6.4) by assuming a linear change in crack opening for the two subcritical loads, and linearly extending this to the critical load. This approach is strictly only valid for elastically behaving materials, however, due to the continuous elastic alumina network the amount of plastic behaviour should be minimal. Moreover, the extrapolated crack opening profile fits the Irwin parabola, confirming that this approach can be used in this situation.

Increasing copper content led to an increase in the width of the crack profile and the distance at which the crack opening approached the Irwin parabola increases with increasing copper content (figure 5.14 a)). For higher copper contents, the composite is tougher and the elastic modulus lower, thus a larger crack opening can be tolerated before crack growth occurs. When the crack opening reaches the Irwin parabola, the crack is no longer bridged by ductile ligaments. As explained above, higher copper contents cause the bridged zone (x_{br}) to be longer. This is seen more clearly in figure 6.6 b): there is a linear increase in x_{br} with increasing copper content from 1.6 to 2.1 to 2.4 mm for increasing copper content from 15 to 41 to 55 vol.%.

Increasing copper ligament diameter led to an increase in the width of the crack profile and an increase in the distance from the crack tip at which the crack opening approaches the Irwin parabola. The value of x_{br} increased from 1.5 to 2.1 mm for an increase in ligament diameter from 1 to 15 μm. The bridged region is expected to be larger with increasing copper ligament diameter, since a thicker copper ligament can stretch and plastically deform more before fracturing. It is for the same reason that the crack opening is wider for a thicker copper ligament. The latter effect is less pronounced for increasing ligament diameter than increasing copper content, since increasing copper content will allow more dissipation of energy due to plastic deformation. The size of the bridged crack region is in the same order of magnitude as the thickness of the sample. Thus, there is clearly large scale crack bridging.

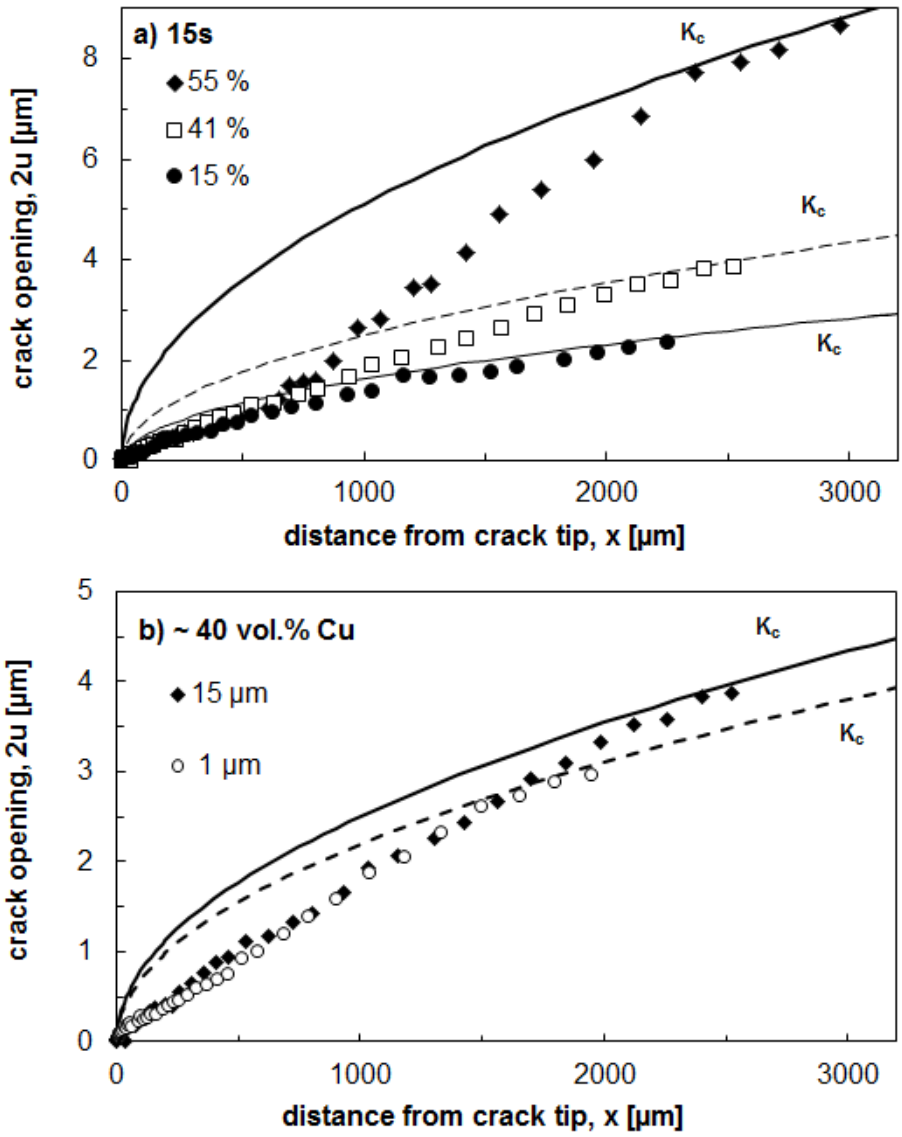

Figure 6.4: Crack profiles extrapolated to the critical load of samples with varying a) copper content (ligament diameter 15 μm) and b) copper ligament diameter (40 vol.%Cu).

In figure 6.5, the first 100 μm of each curve was fitted to the Irwin parabola in order to determine K_{IO}. In figure 6.5 d), the data points from a crack length of 24 to 60 μm were ignored in the fitting, since in this region the crack had branched into 2 to 3 cracks and was thus impossible to accurately measure the crack opening. The crack tip toughness of the 15s samples with 15, 41 and 55 vol.% Cu were calculated to be 1.8, 1.6 and 1.4 MPa$\sqrt{\text{m}}$, respectively. The crack tip toughness of 1p-38 was 2.2 MPa$\sqrt{\text{m}}$. The value seems high in comparison to the 15s samples, but will be discussed in the next paragraph.

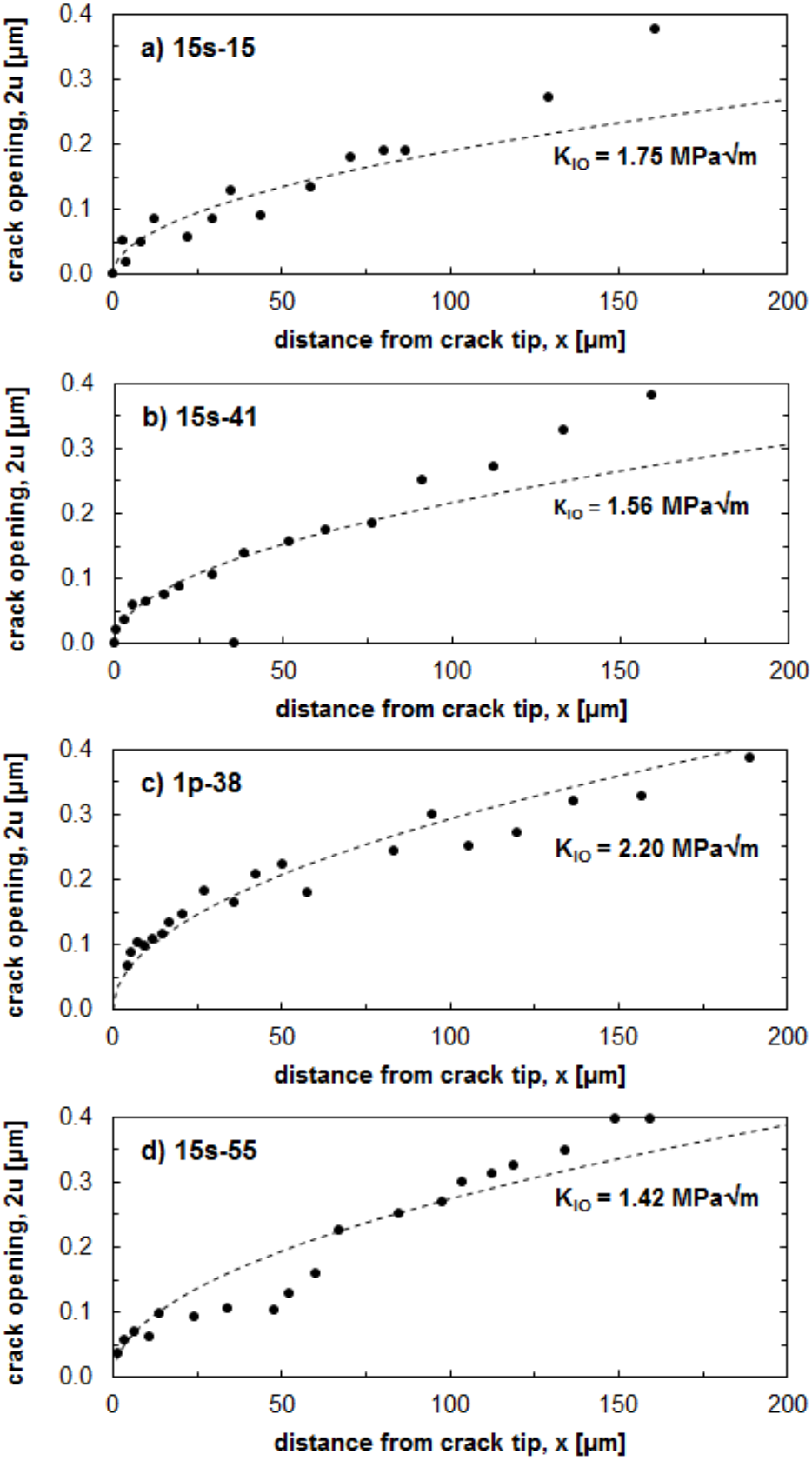

Figure 6.5: First 200 μm of the crack profiles of sample a) 15s-15, b) 15s-41, c) 1p-38 and d) 15s-55. The first 100 μm of the curve was fitted to the Irwin parabola to determine the crack tip toughness.

Ostrowski and Rödel [125] found the crack tip toughness of alumina of two different starting grain sizes (0.2 and 1.0 μm) to be 2.0 MPa$\sqrt{\text{m}}$. The variation of K_{IO} with porosity, p, was found to be:

$$K_{IO}(P) = K_{IO,100}\left(1 - \frac{P}{P_O}\right)^n \tag{6.1}$$

where $K_{IO,100}$ is the crack tip toughness of 100 % dense alumina, n = 1.35, and P_O the porosity where crack tip toughness tends to zero, for these composites assumed to be 60 %. Thus for porosities of 15, 41 and 55 %, K_{IO} values of 1.36, 0.42, 0.07 MPa$\sqrt{\text{m}}$ would be expected. The variation in K_{IO} for porous alumina with porosity and for the 15s samples with copper content are shown in figure 6.6. K_{IO} varies almost linearly with copper content: from 1.75 to 1.56 to 1.42 MPa$\sqrt{\text{m}}$ for copper contents of 15, 41 and 55 vol.%, respectively. Now, the crack tip toughness of metal-ceramic composites is based on the K_{IO} of the porous ceramic part, since at the very tip of the crack, there are no crack bridges, just some regions of copper intersecting the tip. The effect of the metal phase is, thus, much smaller than in the bridged crack region. Therefore, the decrease in K_{IO} with increasing copper content is consistent with expectation. The difference between K_{IO} for alumina and the infiltrated composite (see the distance between the two curves in figure 6.6) increases with increasing copper content. This is expected, since more copper at the tip of the crack will toughen the respective porous ceramic to a greater extent. Now, K_{IO} of 1p-38 (2.2 MPa$\sqrt{\text{m}}$) was much higher than that of 15s-41 (1.56 MPa$\sqrt{\text{m}}$), despite the somewhat lower copper content. Assuming the same copper content, at the very tip of the crack, there will be many more, finely spaced copper regions in the 1p sample, and fewer, further apart copper regions for the 15s sample. Here, the number of ligaments at the tip has a stronger influence than the diameter of the ligaments. As a result, the R-curve of the 1p sample starts at a higher value of K and a steeper initial slope, but has a lower plateau value, since at longer crack lengths the ligament diameter dominates the toughening behaviour (figure 5.13 c)). This was also explained in the section 6.2.4.

By subtracting the value of K_{IO} from the R-curves of the relevant samples, $K_\mu(\Delta c)$ could be determined. Then using equation 6.2 [67] the $R_\mu(\Delta c)$ curves (figure 6.7 were determined. This is the crack length dependent microstructural contribution to toughening.

$$R_\mu = \frac{K_\mu^2 + 2K_\mu K_{IO}}{E'} \tag{6.2}$$

The R_μ curves rise with increasing copper content. For the lower three copper contents, this increase is relatively small. When the copper content was increased from 41 to 55 vol.% there was a much higher increase in the curve. The plateau, or steady state

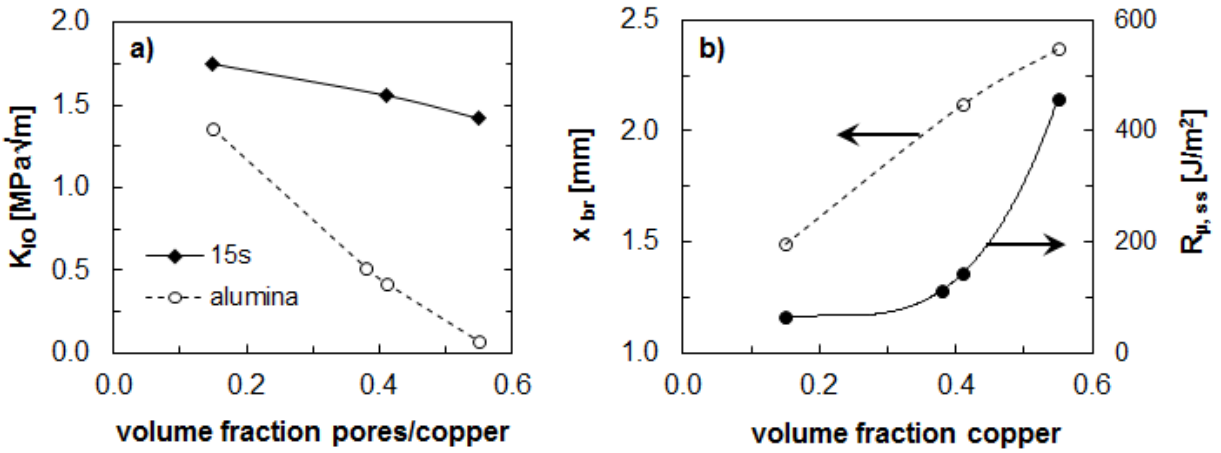

Figure 6.6: a) Variation in K_{IO} of 15s composites with copper content (experimental) and porous alumina with porosity (equation 6.1). b) Variation of bridged crack length (x_{br}) of 15s composites with copper content and $R_{\mu,ss}$ of 15s and 1p.

(ss), values of R_{μ} have been plotted against copper content in figure 6.6 b). Here the effect of copper content is shown more clearly. Increasing copper content from 15 to 38 to 41 vol.% increased $R_{\mu,ss}$ from 64 to 113 to 144 J/m^2. Increasing copper content further to 55 vol.% increased $R_{\mu,ss}$ to 459 J/m^2. Previously, it was noted that the K_{IO} value of 2.2 MPa$\sqrt{\text{m}}$ of the 1p-38 sample was rather high in comparison to the 15s samples. However, once this was subtracted from the R-curves and converted, the resulting $R_{\mu,ss}$ value is consistent with the 15s samples. The data point fits on the curve of the variation of $R_{\mu,ss}$ with copper content. It appears that somewhere between 41 and 55 vol.% copper is a threshold value where the composite changes from CMC behaviour to MMC behaviour. Below the threshold value, the toughness is limited by the alumina network (CMC behaviour). Above the threshold value, the toughness is more influenced by the copper network (MMC behaviour).

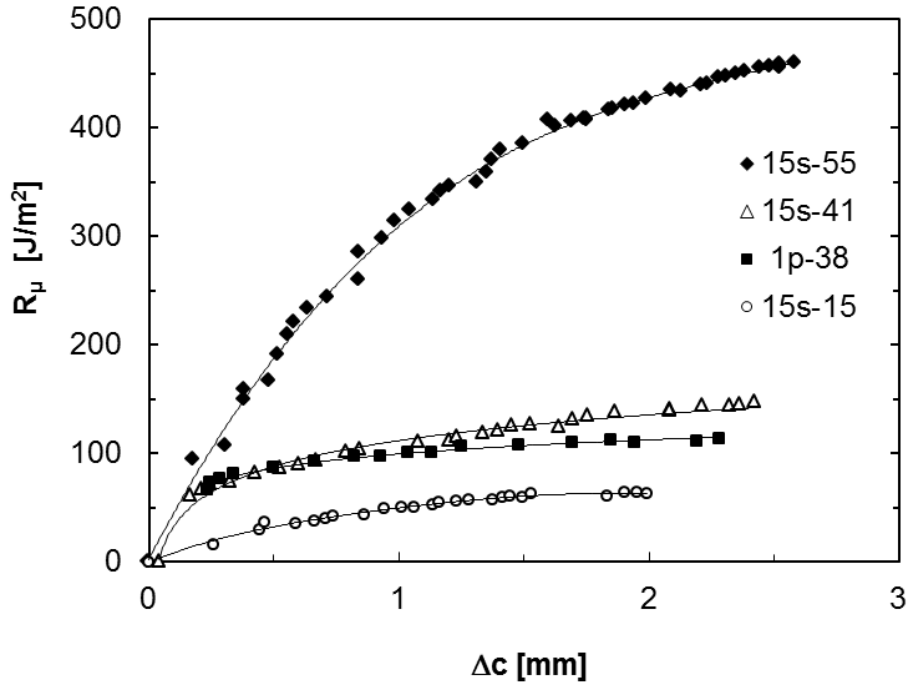

Figure 6.7: R_μ as a function of incremental crack length.

6.3 Thermal properties

6.3.1 Thermal expansion behaviour

Change in sample length and Young's modulus

After the first heating and cooling cycle, the 5s and 15s samples had become shorter, with this effect more pronounced for higher copper contents (figures 5.15 and 5.19 a)). The length of the 1p and 30f samples, however, remained constant (figure 5.19 b)). As described in section 2.1.4, there is expected to be a significant amount of residual stress in the composites after production, with tensile stress in the metal phase and compressive stress in the ceramic phase. Zhang et al. [126] also observed a reduction in length in Al-SiC particulate MMCs and attributed it to the relaxation of tensile stress in the metallic phase during the first thermal cycle. Others have also come to a similar conclusion [22,28,127]. In the dilatometry tests, cooling is much slower than the cooling process after production (3 K/min vs. 15 K/min initially), thus allowing for relaxation of stress in the metal phase via creep.

Since the 1p and 30f samples did not shrink, they must have had less residual stress after production. This may be due to the differences in microstructure. The 30f samples have a particularly weak alumina-copper interface, as seen in the fracture surfaces in figures 5.9 and 5.11. The copper ligaments are more free to move along the pore

channels, thus reducing the build-up of residual stress. The 1p samples have a stronger alumina-copper interface than the 30f samples, as seen in the crack path images in figure 5.10. However, the partially sintered alumina network of the 1p samples is weaker than the fully sintered alumina network of the other composites. Therefore, it cannot exercise as much constraint on the copper network. The weak bonds between individual alumina grains would potentially allow the sliding of alumina grains, as discussed in section 6.2.2, to reduce the build-up of residual tensile stress in the copper upon cooling. The 5s and 15s samples have spherical copper regions joint by small windows. The copper in these composites is more highly constrained. Even with a weak interface, the mechanical interlocking of the two phases could lead to a larger build-up of tensile stress upon cooling after production. Since residual stress is highest in the regions of lowest copper ligament diameter [52], the stress in the windows between copper spheres would be much higher than in the copper spheres themselves, leading to more plastic deformation in the window regions.

It was thought that the reduction in sample length may not only be due to relaxation of residual tensile stress, but perhaps also to a reduction in the number of microcracks. If microcracks closed during the first heating cycle did not re-open upon cooling, this could lead to a reduction in the length of the sample. It was predicted that this structural improvement would lead to an increase in Young's modulus. Consequently, E was measured before and after every heat cycle. As expected, the 15s samples had an increase in Young's modulus after the first cycle, a minimal increase in the second cycle and after that no further increase. The reason for the decrease of E in the fourth cycle of the 15s-27 sample (lowest copper content) is uncertain. Despite an 8 % decrease in length in the 5s-38 sample, it showed no increase in E in the first two cycles. In this sample, it is likely that only stress relaxation was responsible for the decrease in sample length, and not the closing of microcracks. The slight increase in the third and decrease in the fourth cycle are within the error of measurement.

Conversely, the 30f samples had a decrease in Young's modulus in the first cycle, an increase in each of the remaining cycles, such that after four cycles E was similar to the original value. This change is difficult to explain. It is possible that any microcracks that had closed during heating had simply re-opened during cooling, due to the weaker interface strength. But this does not explain the decrease in E in the first cycle. The reason for this remains unclear. E of the 1p-28 sample was constant within the error of measurement. This was to be expected, considering the constant sample length.

Explanation for the hysteresis in the strain curves using the CTE curves

The hysteresis in the strain curves can be explained similarly to the model presented by Hoffman et al. [2] (chapter 2.2), however, with some differences. The parts of the curve are numbered differently, since this observation begins at room temperature. The change in the slope of the strain curves is more clearly seen in the CTE curves in figure 5.17. This model to explain the hysteresis in the strain curve is, therefore, based on the trends seen in the CTE vs. temperature curves of the 5s and 15s samples (figure 5.17 a) and b)).

1. Upon heating, the residual tensile stress in the copper is elastically reduced to zero, then compressive stress builds up. The slope of the curve remains constant.
2. When the compressive yield stress is reached, the slope in the strain curve decreases due to plastic strain in the copper. Here the copper expands into pores and microcracks. Since the compressive stress in the copper cannot rise further, neither does the tensile stress in the alumina. The tensile stress in alumina resists further expansion, and the slope drops below that of the strain curve for pure alumina.
3. When there are no more pores or microcracks for the copper to flow into, hydrostatic compressive stress can build in the copper, more stress is thus applied to the alumina and the slope of the curve increases again.
4. During the first 50 °C of cooling, there is a sharp decrease in the slope of the curve (not mentioned in model from Hoffman et al.). The compressive stress in the copper and tensile stress in the alumina are suddenly released and the composite springs back upon initial temperature reduction.
5. Upon further cooling, after an initial minimum and increase in CTE adjusting from the spring-back, the compressive stress in the copper is elastically reduced to zero and tensile stress again builds up in the copper. Here the slope of the curve is similar to part 1.
6. When the tensile yield stress of copper is reached, the slope again decreases due to plastic flow of the copper. The stress in the copper does not increase further, however, may be relaxed by delamination from the alumina.

In the CTE vs. temperature curves (figure 5.17 a) to d)), the transition from stage 1 to stage 2 is seen at the first maximum in the curves where they then decreased. This stage was reached at the lowest temperature for the lowest copper content and at increasing temperatures for increasing copper content. The less copper is present in the composites, the more compressive stress builds up during heating due to the thermal mismatch with alumina [47,52]. Thus for the composite with the lowest copper content, the compressive yield stress was reached at the lowest temperature. This stage does not appear in the 1p and 30f samples. This is due to the weaker interface strength between copper and alumina in the 30f samples and the weak alumina network of the

1p samples reducing the constraint of the copper network. Both effects reduced the amount of constraint the alumina network could exercise on the copper network, such that the compressive yield stress of the copper was not reached.

Stage 3 began at the minimum in the 5s and 15s curves where they again increased. This stage was negligible in the 5s-38 sample, and otherwise started at higher temperatures for increasing copper contents. For a particular copper ligament diameter, a higher copper content leads to more interfaces between copper and alumina. Hence, there are more locations where microcracks (delaminated regions) could form, and therefore, possibly more microcracks. This would require a higher temperature to close all of the microcracks. In the 1p and 30f samples, this stage is only seen in 30f-53, and in this sample even more prominently than all other samples. It is presumed that this was the only sample in this group with enough copper to fill all the pores and microcracks such that hydrostatic compressive stress was able to build up.

Stages 4 and 5 are similar in all 5s and 15s samples. In the 1p and 30f samples there was no adjustment after the spring-back but rather a smooth transition. This, too, was probably due to the lower constraint of the copper network in these composites. Stage 6, where the tensile yield stress of the copper was reached, started at the highest temperature of 210 °C for 15s-27 and otherwise at 110 °C for the other 5s and 15s samples. In the 30f-31, -39 and -53 samples this stage was reached at 170, 130 and 110 °C, respectively and at 110 °C in 1p-38. The lower the copper content of the composites, the more tensile stress builds up during cooling due to the thermal mismatch with alumina [47,52]. Thus for the composite with the lowest copper content, the yield stress is reached at the highest temperature, with the temperature decreasing for increasing copper content. The fluctuations in the curve below 200 °C made it difficult to clearly identify this trend in the 15s-38 and -43 samples.

The effect of copper content and ligament diameter on the strain curves

The rise in the strain curve and maximum strain with higher copper contents (figure 5.16 a) and b)) is consistent with the rule of mixtures. The cooling curve of the samples with 27 to 31 vol.% Cu (apart from 1p-28) was very close to the strain curve of alumina. This means that the amount of copper was not sufficient to exert enough stress upon the alumina to cause it to shrink more than what it would without the presence of copper. Also, since the interface is weak, delamination of the copper from the alumina could also have caused this effect. The hysteresis in the strain curve is due to plastic strain in the copper (explained above). Plastic strain comes from there being enough build-up of thermal mismatch stress for either the compressive or tensile yield stress of copper to be

reached. The less copper there is, the more residual stress builds in the copper due to the thermal mismatch of alumina [47, 52], hence the more hysteresis in the curve.

Varying the copper ligament diameter between 5 and 30 μm had little effect on the strain for both 30 and 40 vol.% Cu. The author did not find any models predicting a change in strain or CTE for differing reinforcement sizes in composites. The sample with the smallest copper ligament diameter, 1p-38, had a higher strain than all the others with a similar copper content. The weaker alumina network of this composite exercised less constraint on the copper network (see also the section of average CTE), thus allowing a greater thermal expansion. For 40 vol% copper, the strain curve of the 30f sample is mostly below that of the 15s sample, but has a similar maximum strain. The differing structures of these sample probably led to a different stress distribution during heating, such that the 30f sample had a lower CTE at first but then higher at higher temperatures. At the highest temperature the amount of copper, and not the structure, was the determining factor, since the maximum strain was equal in both samples.

Average CTE

In figure 6.8, the average CTE a) across the entire temperature range and b) heating from room temperature to 200 °C are compared to the rule of mixtures, Kerner upper and lower bounds, and the Turner model. A CTE close to or below the lower Kerner bound is expected of ceramic matrix composites. A CTE near or above the upper Kerner bound is expected of metal matrix composites. A composite with a continuous ceramic network with isolated metal regions will clearly have a lower CTE than a composite with a continuous metallic network with isolated ceramic regions. The Turner model does not take a particular structure into account but rather assumes constant strain across a composite, consistent with an interpenetrating structure. A composite with an IPN structure would be expected to behave more like a CMC than an MMC, since the continuous ceramic network constrains the metallic network. This should also lead to constant strain across the composite. So the CTE of IPN composites would be expected to lie between the Turner and lower Kerner bounds. One weakness with the Turner and Kerner bounds is that the elastic constants used to calculate them (bulk modulus and shear modulus) are the room temperature values. At higher temperatures these values would be expected to be lower, and thus the predicted CTE values somewhat higher. The bounds, however, would still be within the RoM bounds, which are not affected by the elastic constants.

The general increase in CTE with increasing copper content is consistent with the model predictions, although the slope is higher. Across the entire temperature range, six out of ten of the data points are below any of the model predictions. This is due to

the plastic strain of copper decreasing the physical CTE at higher temperatures upon heating and at lower temperatures upon cooling (compare with figure 5.17 and the previous section on strain curves and physical CTE), thus decreasing the average CTE. Aside from the 1p samples, at lower copper contents the composites behave more like CMCs, with a transition to MMC-like behaviour at higher copper contents. Above a critical copper content, the copper network is apparently not as highly constrained by the alumina network and the composite behaves more like an MMC. This is consistent with observations discussed in sections 6.2.1 and 6.2.2. Despite a lower copper content, the 1p samples also behaved more like an MMC. The weakness of the partially sintered alumina network is less able to exercise constraint on the copper network, as discussed above. The alumina network is less continuous than in the other composites, and less continuous than the copper network, thus having a structure close to that of MMCs. As expected, none of the values were above the Wiener RoM. The CTE values of 15s-27 and 30f-31 are barely above that of pure alumina. This is due to the strong effect of plastic strain on heating: above 500 °C, the physical CTE of both samples is well below that of alumina (figure 5.17), causing the average value across the entire temperature range to be so low.

The average CTE heating from RT to 200 °C was also calculated in order to eliminate the effects of plastic strain, since in this temperature range thermal expansion is elastic. Here, all the data points are at or above the lower Kerner bound. The CTE of three of the four 30f samples lies on the lower Kerner bound, thus behaving like CMCs. Somewhere between 45 and 53 vol.% Cu is the threshold for the transition from CMC to MMC-like behaviour in the 30f samples, since the CTE of 30f-53 is above even the Wiener RoM. The CTE of all other samples indicate MMC-like behaviour. The CTE of some samples being above the Wiener RoM is not entirely unusual. Unlike the Voigt and Reuss bounds for elastic properties, the Wiener RoM bounds do not represent the energetically widest range of values for thermal properties [79]. Skirl et al. [22] found the CTE of alumina-aluminium IPN composites from 200 to 280 °C with 30 to 40 vol.% Al to be above the RoM, and for lower copper contents to be between RoM and the upper Kerner bound. Hsieh and Tuan [84] found the Turner model and the upper RoM to be the only bounds to encompass all of the data. In this work, none of the bounds are able to encompass all of the data. This is probably due to the wide range of copper contents and ligament diameters tested, in addition to the wide variation in residual porosity.

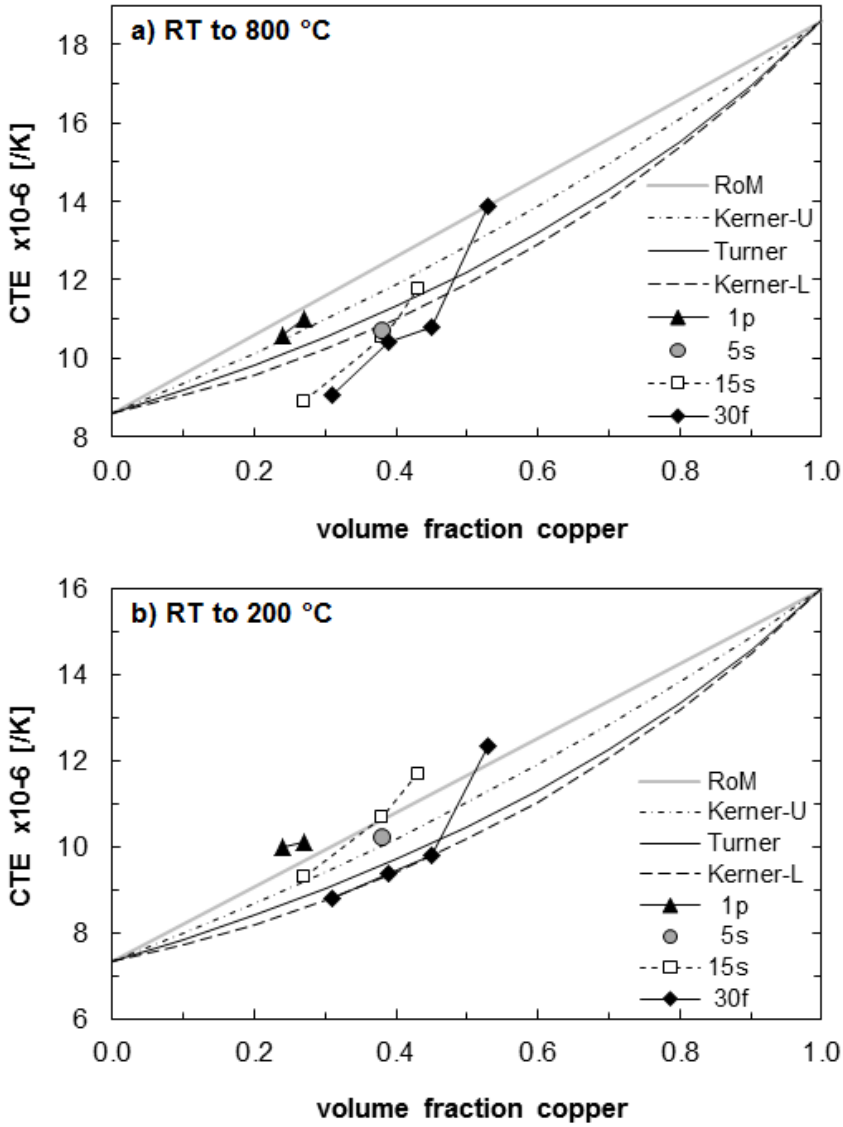

Figure 6.8: Average CTE across a temperature range of a) room temperature to 800 °C and b) room temperature to 200 °C. The bounds of the Wiener rule of mixtures (RoM), the Kerner upper (U) and lower (L) bounds and the Turner model are included.

6.3.2 Thermal conductivity

In figure 6.9, the experimental results for thermal conductivity are compared to three different models: the Wiener rule of mixtures, the Hashin-Shtrikman bounds and the Lichtenecker average (described in section 2.2.3). The increase in conductivity is consistent with model predictions. The results are well within the bounds of Wiener's RoM. This is to be expected, since the RoM represents two extreme cases, neither of which are applicable to these composites. The upper bound represents a lamellar structure with the direction of heat flow parallel to the phase boundaries. The lower boundary represents heat flow perpendicular to the phase boundaries.

The data is just bounded by the Hashin-Shtrikman bounds, within the error of measurement (±5 %). The lower bound represents a CMC and the upper bound an MMC structure. The Lichtenecker average is for a simplified cubic interpenetrating structure (explained in more detail in section 2.2.3. Most of the data points lie close to the Lichtenecker average, as expected for interpenetrating composites. The 30f samples lie on the lower Hashin-Strikman bound, indicating CMC-like behaviour. At higher copper contents, above 35 to 40 vol.%, most samples tend toward the upper HS bound, or MMC-like behaviour. This is similar to what was observed for the coefficient of thermal expansion. There appears to be a threshold value of copper content at which there is a transition from CMC to MMC-like behaviour.

Unlike CTE, this threshold is not observed in the 30f samples. However, here the maximum copper content in the 30f samples measured was 38 vol.%, whereas the transition to MMC behaviour in CTE was as a copper content above 45 vol.%. An alternative reason for the lower conductivity of the 30f samples is the presence of microcracks, also discussed in the section on thermal expansion. Any pockets of air have a very low thermal conductivity and would decrease the overall conductivity of the composites.

Given the presence of residual porosity and microcracks present in most of the composites, it is surprising that the experimental values fit the models so well. In any case, the Hashin-Shtrikman bounds gives the maximum bounds for the experimental data, and the Lichtenecker average is most suitable for predicting the thermal conductivity. The independence of thermal conductivity from copper ligament diameter in the steady-state measurements is not surprising. There are no models to predict this, and it is generally accepted that thermal properties are independent of microstructural scale [128]. The transient values appear to show a significant decrease in conductivity with increasing copper ligament diameter 5.4, however, this can be explained by the variation in copper content and residual porosity.

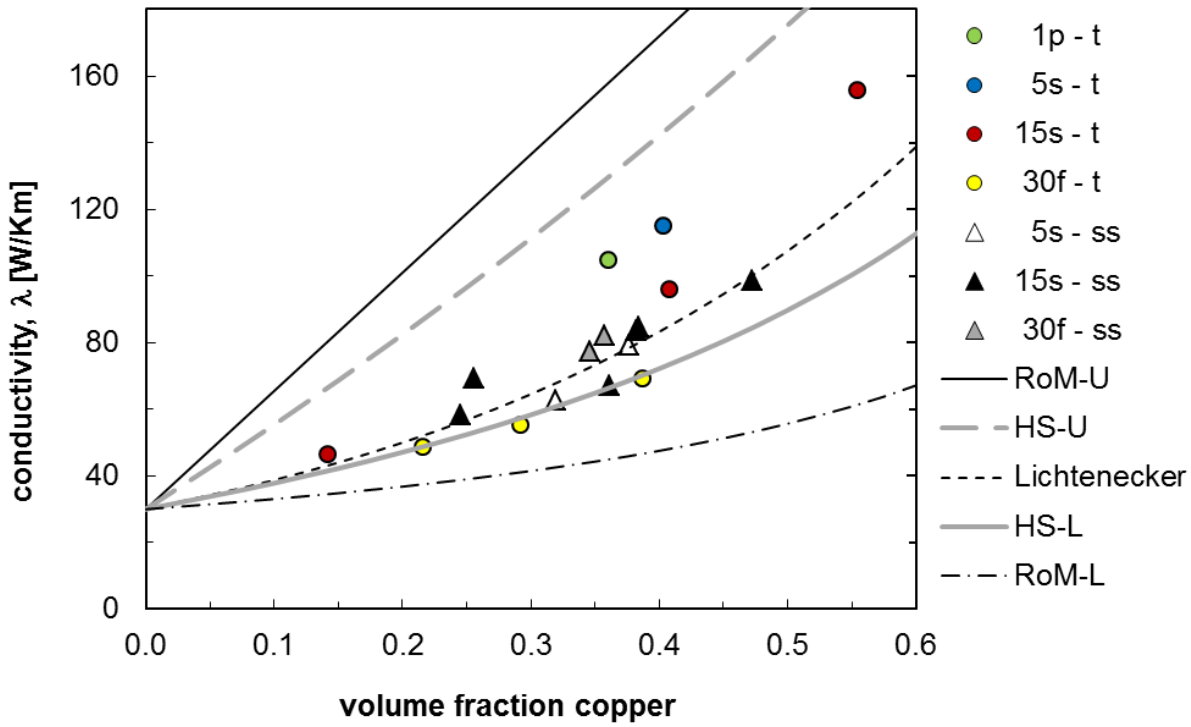

Figure 6.9: Variation of thermal conductivity with copper content measured under transient (t) and steady-state (ss) conditions. Values are compared to the upper (U) and lower (L) rule of mixtures (RoM), the upper and lower Hashin-Shtrikman (HS) bounds and the Lichtenecker average.

6.4 Wear behaviour

Friction coefficient and temperature

In some samples, the curve of the friction coefficient had a zigzag form (figure 5.21). There was no identifiable trend as to when this behaviour would occur. A probable explanation for this is as follows: the friction coefficient decreases steadily as a tribolayer forms, then a sudden increase when the tribolayer is partially or fully removed, with this sequence repeated cyclically. No explanation has been found as to why it occurred in some samples but not others, or why it occurred one out of three times for a particular sample, although all other known testing conditions were the same.

The colours of the wear track and wear debris (table 5.6) show that oxidation of the copper had occurred. Black is most likely copper oxide, green a mixture of copper hydroxide and copper carbonate due to a reaction with air and humidity (relative humidity typically 60-80 %) [129].

The temperature of the alumina pin was lowest against the 30f composites - around 10 °C lower than all other composites (table 5.6). Since the thermal conductivity was

found to be independent of copper ligament diameter (section 6.3.2), this was not due to the thermal conductivity of the composite. The heat generated in the alumina ball is due to the friction between the composite and the ball. Although the 30f samples have the coarsest structure, this clearly did not result in the highest temperature. The resulting wear track width in the 30f samples was much narrower that the others, hence a smaller area of contact with the alumina ball. This may have been the cause for the lower temperature, but this is not certain.

The samples containing 20 vol.% copper (apart from 30f-20) had the highest friction coefficient. It is likely that the high ceramic fraction dominated the friction coefficient. However, the friction coefficient was even higher than in pure alumina against alumina. This may have been due to the residual porosity and hence increased roughness of the 20 vol.% copper samples in comparison to the alumina. 30f-20 had less residual porosity, a smoother surface and thus a lower friction coefficient.

Specific wear rate and wear mechanisms

The change in wear rate with copper content varied with the type of sample. The marked decrease in specific wear rate for the last data point on the 5s curve (figure 5.22, data point encircled) can be explained. In all three wear tests for 5s-50, there was cyclic tribolayer behaviour, similar to figure 5.21 c). The tribolayer had a lubricating effect, which led to a decrease in the friction coefficient and specific wear rate.

In the 1p samples there was a similar trend, but there was a different cause. At this point it is pertinent to mention that the measured specific wear rate of copper, $4\text{x}10^{-5}$ $mm^3/(Nm)$, is lower than most of the composites. The value for densely sintered alumina (CT 3000, 0.8 μm grain size, also used for the ceramic phase in 5s and 15s samples) was $1\text{x}10^{-5}$ mm^3/Nm. Starting from the highest copper fraction for the 1p (partially sintered) samples, adding alumina initially increases the specific wear rate. The area of contact between alumina grains is quite small and thus weak [125]. The interface strength between copper and alumina is also known to be quite low [43, 90]. During wear testing, alumina grains can thus be easily pulled out and act as an abrasive. The more copper is worn away, the more easily further alumina grains break out and thus the cycle continues. The more (weakly bonded) alumina, the more 'abrasive' available, and the less copper available for it to become re-embedded. However, with further decreasing copper content, the contact area between alumina grains becomes larger and thus stronger, so grains are not as easily pulled out. Here the role of alumina as a reinforcement has the dominant effect. Another factor as to why the 1p samples have a higher specific wear rate than the other samples is the grain size of alumina (5 μm, compared to 0.8 μm in the 5s and 15s and 0.1 μm in the 30f samples). The

larger grains are more likely to contain microcracks and thus the grains fracture more easily [90, 101–103].

A decrease in wear rate for increasing metal ligament (or cell) diameter was also found in alumina-aluminium interpenetrating composites [98]. In that work, the thicker, more widely spaced alumina regions were found to provide better shielding of the aluminium. In this work, increasing copper ligament diameter coincided with a decrease in alumina grain size, but also an increase in coarseness of the alumina network. The smaller alumina grains more easily become re-embedded in the larger copper regions and, thus, do not act as an abrasive. This explanation cannot be used for the 10 N series, which has the opposite trend. It may be that wear of the composites under 10 N load was in a mild wear regime with limited alumina microfracture, particularly for the samples with the finest copper and thus alumina networks. As the copper and alumina networks increase in size, the amount of microfracture would be expected to increase [1, 103, 130], though it was not possible to measure this. The last two data points appear to follow the same trend as the 20 N series.

Although the 30f samples did not have the highest measured hardness or Young's modulus (figures 5.5 and 5.4), they clearly had the highest wear resistance. They had the smallest alumina grain size and the largest copper ligament diameter. The copper fibres were also running along the surface of the sample, leading to much larger copper regions than the other composites. The alumina grains could re-embedd in the copper rather than act as an abrasive, this decreasing wear. The small grain size would have also made the alumina network stronger, since smaller grains contain less defects. The alumina network was coarsest in the 30f samples, and due the the smaller grain size probably strongest, thus providing better shielding of the copper regions [98]. This shielding effect diminished with higher copper contents. These effects caused the lower wear rate, but further effects may have enhanced this. The lower initial wear rate would have kept the wear track narrower and shallower than the other composites. A lower contact area between the alumina ball and wear track would have led to less frictional heat being generated (as observed), thus less oxidation and adhesion of the copper phase preventing severe wear. The fracture toughness of the 30f samples was significantly higher than the other composites (section 5.2.4), and wear resistance is known to increased with increasing fracture toughness [131]. However, since only short cracks are likely in the damaged layer below the wear surface, and 30f showed high toughness for long cracks, it is not certain whether this factor contributed to the superior wear resistance of the 30f samples.

7 Conclusions

In this work, alumina-copper composites of varying copper content and copper ligament diameter were produced. The use of wool felt as a pore forming agent was new. Copper contents of between 15 and 55 vol.% and copper ligament diameters of between 1 and 30 μm were achieved. The effects of microstructure on application relevant mechanical and thermal properties, as well as wear behaviour, were investigated.

Young's modulus decreased with increasing copper content. The FEM data fit along the upper Hashin-Shtrikman bound, with experimental data bounded by the lower HS bound and Reuss bound. The lower experimental values were due to residual porosity and microcracking. The 1p and 30f samples had lower values than the 5s and 15s samples due to the weak alumina network in the 1p samples and the weak alumina-copper interface and/or microcracking in the 30f samples.

The Vickers hardness of the composites decreased with increasing copper content. Upon increasing the copper content there was initially a sharp decrease in hardness, with further increases in copper content leading to a smaller decrease in hardness. This was due to a threshold copper content, above which sliding of alumina grains is possible, with less resistance to the plastic flow of copper. Analogous to Young's modulus, and for similar reasons, the 1p and 30f samples had lower values than the 5s and 15s samples composites. In contrast, hardness was not sensitive to residual porosity.

Bending strength increased with increasing copper content. The Weibull moduli calculated were similar to that of monolithic ceramics. Typical fracture causing defects included abnormally large alumina grains, large copper regions, residual porosity, carbon flakes, as well as volume and surface defects. The fracture surface of the 30f samples did not reveal any fracture causing defects. The high ductility of the copper was evidenced in stretched and necked fractured copper fibres. Dimples along the copper fibres were seen where the copper had pulled away from the alumina. This in addition to the pull-out of copper fibres of up to several millimetres highlighted the weak interface strength between copper and alumina.

The R-curve behaviour of the composites was investigated with the SEVNB and CT sample geometries. Toughening mechanisms included ductile crack bridging, elastic crack bridging, crack deviation and crack branching. Crack path and fracture surface images showed that the alumina-copper interface strength decreased with increasing

copper ligament diameter. Increasing the copper content led to a steeper R-curve with a higher plateau K value. Increasing copper ligament diameter led to a decrease in the initial measured K, a decrease in the slope and a higher plateau value of K. A further increase in ligament diameter, coinciding with a change in the structure of the copper network to long fibres, caused a dramatic rise in the R-curve.

The crack opening and bridged crack length both increased with increasing copper content and ligament diameter. K_{IO} decreased with increasing copper content, since K_{IO} of the composite is governed by the K_{IO} of the respective porous ceramic. Decreasing the copper ligament diameter increased K_{IO} significantly, since this increased the number of ligaments intersecting the crack tip. R_{μ}, was not significantly affected by the copper ligament diameter. Increasing copper content led initially to a small increase in R_{μ}, with a further increase in copper content causing a much higher increase in R_{μ}. It was concluded that there is a threshold copper content, below which the R-curve behaviour is dominated by the alumina network and above which dominated by the copper network.

The thermal strain curves of the composites were hysteretic due to plastic strain in the copper phase. A modified version of the model from Hoffman et al. [2] was proposed to explain the shape of the strain curve. The reduction in length and increase in Young's modulus of the 5s and 15s samples after the first thermal cycle were proposed to be due to a relaxation of residual stress, as well as the closing of microcracks between the copper and alumina. This behaviour was not seen in the 1p and 30f samples, since the lower constraint of the copper network in both prevented residual stress forming. Increasing copper content increased the coefficient of thermal expansion, with the effect of copper ligament diameter not clear. Composites with lower copper contents behaved like CMCs, whereas at higher contents more like MMC, despite a continuous alumina network still being present. Thermal conductivity increased with copper content and was independent of copper ligament diameter. The Hashin-Shtrikman bounds encompassed all the experimental data, with the Lichtenecker average providing a good prediction for most of the samples. Congruent with the thermal expansion behaviour, the thermal conductivity of composites at lower copper contents was consistent with CMCs, whereas at higher contents more like MMCs.

Increasing the amount of copper decreased the wear resistance, except where cyclic tribolayer behaviour occurred or where the alumina grains were weakly bonded. Increasing the copper ligament diameter increased the wear resistance. In the 1p, 5s and 15s composites, the wear mechanism was a mixture of adhesive and oxidative. In the 30f composites, a mixture of abrasive and oxidative wear pertained. The 30f samples with up to 45 % had a superior wear resistance, with the wear factor at least an order of magnitude lower than the other composites. This was due to the coarser,

stronger alumina network more effectively shielding the copper and lower wear track temperature reducing oxidation and preventing adhesion of the copper.

Increasing copper content led to a decrease in Young's modulus, hardness and wear resistance, but an increase in bending strength, fracture toughness, coefficient of thermal expansion and thermal conductivity. At lower copper contents the composites behaved like ceramic matrix composites, whereas at higher copper contents the behaviour was more like metal matrix composites, despite the alumina network still being continuous. No definite correlation between copper ligament diameter and Young's modulus, hardness, bending strength and the thermal properties was observed. Increasing copper ligament diameter led to a significant increase in fracture toughness and wear resistance, as well as an apparent decrease in alumina-copper interface strength.

Young's modulus, bending strength and thermal conductivity were sensitive to residual porosity and microcracking, whereas hardness, fracture toughness, CTE and wear resistance were not. The less contiguous, weaker alumina network in the partially sintered led to MMC-like behaviour. The Young's modulus, fracture toughness, hardness and wear resistance were lower, whereas the CTE and thermal conductivity were higher than the other composites. The particularly weak alumina-copper interface of the wool based (30f) samples had a detrimental effect on the Young's modulus, bending strength and hardness, and decreased the CTE. However, the 30f samples had an excellent fracture toughness and wear resistance.

In light of the intended application - wear parts such as automobile brakes - the 30f composites with less than 45 vol.% copper are the most promising due to the particularly good wear resistance. Further investigations on the wear behaviour, in particular for much longer distances and in combination with the counterface brake material, would be necessary in order to confirm this potential. Alumina-copper composites also show high potential for high throughput industrial applications where rapid cooling combined with sliding motion is required. Examples include extrusion, rolling, punching or deep drawing of metals or polymers as well as jet nozzle tips for the injection or dispersion of preheated liquids and gasses. Research is currently being conducted in an EU project (Grant agreement no.: CP-FP 228869-2) on the viability of alumina-copper composites for automobile breaks and valves as well as a heat sink and wear resistent lining inside rocket thrusters.

Bibliography

[1] M. Knechtel, H. Prielipp, H. Müllejans, N. Claussen and J. Rödel. *Mechanical Properties of Al/Al_2O_3 and Cu/Al_2O_3 Composites with Interpenetrating Networks*. Scr. Metall. Mater., **31** (8), pp. 1085–1090, 1994.

[2] M. Hoffman, S. Skirl, W. Pompe and J. Rödel. *Thermal Residual Strains and Stresses in Al_2O_3/Al Composites with Interpenetrating Networks*. Acta Mater., **47** (2), pp. 565–577, 1999.

[3] P. Agrawal, K. Conlon, K. J. Bowman, C. T. Sun, F. R. Cichocki and K. P. Trumble. *Thermal residual stresses in co-continuous composites*. Acta Mater., **51** (4), pp. 1143–1156, 2003.

[4] M. Bahraini, L. Weber, J. Narciso and A. Mortensen. *Wetting in infiltration of alumina particle preforms with molten copper*. J. Mat. Sci, **40** (9-10), pp. 2487–2491, 2005.

[5] E. J. Gonzalez and K. P. Trumble. *Spontaneous Infiltration of Alumina by Copper-Oxygen Alloys*. J. Am. Ceram. Soc., **79** (1), pp. 114–120, 1996.

[6] N. Travitzki. *Microstructure and mechanical properties of alumina/copper composites fabricated by different infiltration techniques*. Mater. Lett., **36**, pp. 114–117, 1998.

[7] N. A. Travitzky and A. Shlayen. *Microstructure and mechanical properties of Al_2O_3/Cu-O composites fabricated by pressureless infiltration technique*. Mat. Sci. Eng. A, **244** (2), pp. 154–160, 1998.

[8] D. R. Gaskell. *An Introduction to Transport Phenomena in Materials Engineering*, chap. Properties of Solid Metals, pp. 607–608. Prentice Hall, 1992.

[9] K. S. W. Sing, D. H. Everett, R. A. W. Haul, L. Moscou, R. A. Pierotti, J. Rouquerol and T. Siemieniewsk. *Reporting Physisorption Data for Gas/Solid Systems with Special Reference to the Determination of Surface Area and Porosity*. Pure Appl. Chem., **57** (4), pp. 603–619, 1985.

[10] K. Schwartzwalder and A. V. Somers. *Patent US 3090034: Method of Making Porous Ceramic Articles*. 1963.

[11] A. R. Studart, U. T. Gonzenbach, E. Tervoort and L. J. Gauckler. *Processing Routes to Macroporous Ceramics: A Review*. J. Am. Ceram. Soc., **89** (6), pp. 1771–1789, 2006.

[12] P. Colombo. *Conventional and novel processing methods for cellular ceramics*. Phil. Trans. R. Soc. A, **364**, pp. 109–124, 2006.

[13] J. Saggio-Woyansky and C. E. Scott. *Processing of Porous Ceramics*. Am. Ceram. Soc. Bull., **71**, pp. 1674–1682, 1992.

[14] F. F. Lange, B. V. Velamakanni and A. G. Evans. *Method for Processing Metal-Reinforced Ceramic Composites*. J. Am. Ceram. Soc., **73** (2), pp. 388–393, 1990.

[15] D. R. Clarke. *Interpenetrating Phase Composites*. J. Am. Ceram. Soc., **75** (4), pp. 739–759, 1992.

[16] W. D. Kingery, H. K. Bowen and D. R. Uhlmann. *Introduction to Ceramics*. Wiley-Interscience, 2 ed., 1976.

[17] R. Brezny, D. J. Green and C. Q. Dam. *Evaluation of Strut Strength in Open-Cell Ceramics*. J. Am. Ceram. Soc., **72** (6), pp. 885–889, 1989.

[18] D. Brown and D. Green. *Investigation of Strut Crack Formation in Open Cell Alumina Ceramics*. J. Am. Ceram. Soc., **77** (6), pp. 1467–1472, 1994.

[19] L. J. Gibson and M. F. Ashby. *Cellular Solids - Structure and Properties*. Pergamon, 1988.

[20] K. Konopka, A. Olszowka-Myalska and M. Szafran. *Ceramic-metal composites with an interpenetrating network*. Mater. Chem. Phys., **81** (2-3), pp. 329–332, 2003.

[21] D. J. Cumberland and R. J. Crawford. *The packing of particles*. Elsevier, Amsterdam, 1 ed., 1987.

[22] S. Skirl, M. Hoffman, K. Bowman, S. Wiederhorn and J. Rödel. *Thermal expansion behavior and macrostrain of Al_2O_3/Al with interpenetrating networks*. Acta Mater., **46** (7), pp. 2493–2499, 1998.

[23] F. R. Cichocki, K. P. Trumble and J. Rödel. *Tailored Porosity Gradients via Colloidal Infiltration of Compression-Molded Sponges*. J. Am. Ceram. Soc., **81** (6), pp. 1661–64, 1998.

[24] F. Stromberger. *Herstellung von Gradientenwerkstoffen über ortsabhängige Verdichtung polymerer Vorformen*. Diplomarbeit, Technische Universität Darmstadt, 1998.

[25] A. Neubrand, T. Chung and J. Rödel. *Residual stresses in functionally graded plates*. J. Mater. Res., **17** (11), pp. 2912–2920, 2002.

[26] M. König. *Herstellung und Charakterisierung eines Kupfer-Aluminiumoxid Verbundwerkstoffs mit Durchdringsgefüge*. Diplomarbeit, Technische Universität Darmstadt, 2006.

[27] R. Brezny and D. Green. *The effect of cell size on the mechanical behavior of cellular materials*. Acta Metall. Mater., **38** (12), pp. 2517–2526, 1990.

[28] A. Mattern. *Interpenetrierende Metall-Keramik-Verbundwerkstoffe mit isotropen und anisotropen Al_2O_3-Verstärkungen*. Ph.D. thesis, Dissertation Universität Karlsruhe, 2004.

[29] N. Travitzki and N. Claussen. *Microstructure and Properties of Metal Infiltrated RBSN Composites*. J. Eur. Ceram. Soc., **9**, pp. 61–65, 1992.

[30] C. Garcia-Cordovilla, E. Louis and J. a. Narisco. *Overview No. 134 - Pressure infiltration of packed ceramic particulates by liquid metals*. Acta Mater., **47** (18), pp. 4461–4479, 1999.

[31] K. Prakasan and S. Seshan. *Electrical conductivity of squeeze cast copper*. J. Mat. Sci. Letters, **16**, pp. 1588–1589, 1997.

[32] H. Prielipp, M. Knechtel, N. Claussen, S. Streiffer, H. Müllejans, M. Rühle and J. Rödel. *Strength and fracture toughness of aluminum/alumina composites with interpenetrating*

networks. Mat. Sci. Eng. A, **197**, pp. 19–30, 1995.

[33] A. W. Adamson. *Physical Chemistry of Surfaces*, vol. 4th Ed. Wiley-Interscience, 1982.

[34] P. R. Chidambaram, G. R. Edwards and D. L. Olson. *Kinetics of Interlayer Formation on Polycrystalline α-Al_2O_3/Copper-Titanium Alloy Interface*. Metall. Mater. Trans. A, **25A**, pp. 2083–2090, 1994.

[35] P. R. Chidambaram, A. Meier and G. R. Edwards. *The nature of interfacial phenomena at copper-titanium/alumina and copper-oxygen/alumina interfaces*. Mat. Sci. Eng. A, **206**, pp. 249–258, 1996.

[36] I. A. Aksay, C. E. Hoge and J. A. Pask. *Wetting under Chemical Equilibrium and Nonequilibrium Conditions*. J. Phys. Chem., **78** (12), pp. 1178–1183, 1974.

[37] N. Eustathopoulos. *Dynamics of Wetting in Reactive Metal/Ceramic Systems*. Acta Mater., **46** (7), pp. 2319–2327, 1998.

[38] B. Derby, P. Xiao and J. Webster. *Neutron reflection studies of titanium segregation to metal-ceramic interfaces*. Physica B, **248**, pp. 304–309, 1998.

[39] B. C. Allen and W. D. Kingery. *Surface Tension and Contact Angles in Some Liquid Metal-Solid Ceramic Systems at Elevated Temperatures*. Trans. Metall. Soc. AIME, **215**, pp. 30–37, 1959.

[40] T. E. O'Brien and A. C. D. Chaklader. *Effect of oxygen on the reaction between copper and sapphire*. J. Am. Ceram. Soc., **57** (8), pp. 329–332, 1974.

[41] F. Delannaz, L. Frozen and A. Deruyttere. *The Wetting of Solids by Molten Metals and its Relation to the Preparation of Metal-Matrix Composites*. J. Mat. Sci, **22** (1), pp. 1–16, 1987.

[42] A. Meier, M. D. Baldwin, P. R. Chidambaram and G. R. Edwards. *The effect of large oxygen additions on the wettability and work of adhesion of copper-oxygen alloys on polycrystalline alumina*. Mat. Sci. Eng. A, **196**, pp. 111–117, 1995.

[43] C. Beraud, M. Courbiere, C. Esnouf, D. Juve and D. Treheux. *Study of copper-alumina bonding*. J. Mat. Sci, **24**, pp. 4545–4554, 1989.

[44] C. Seager, K. Kokini, K. Trumble and M. Krane. *The influence of $CuAlO_2$ on the strength of eutectically bonded Cu/Al_2O_3 interfaces*. Scr. Mater., **46**, pp. 395–400, 2002.

[45] N. Eustathopoulus and B. Drevet. *Interfacial Bonding, Wettability and Reactivity in Metal-Oxide Systems*. J. Physique, **4** (10), pp. 1865–1881, 1994.

[46] P. Kritsalis, L. Coudurier and N. Eustathopoulos. *Contribution To The Study Of Reactive Wetting In The CuTi/Al_2O_3 System*. J. Mat. Sci, **26** (12), pp. 3400–3408, 1991.

[47] V. D. Krstic. *On the fracture of brittle-matrix/ductile-particle composites*. Phil. Mag. A, **48** (5), pp. 695 – 708–695 – 708, 1983.

[48] T. Emmel, U. Stiefel, D. Gross and J. Rödel. *Deformation and Failure in Metallic Materials*, chap. Damage and Failure of Ceramic Metal Composites: Experimental and Numerical Investigations, pp. 203–221. Springer, 1 ed., 2003.

[49] A. D. Krawitz and T. M. Holden. *The Measurement Of Residual-Stresses Using Neutron-Diffraction*. MRS Bull., **15** (11), pp. 57–64, 1990.

[50] P. J. Withers. *Neutron Stain Measurement of Internal Strain in Metal and Ceramic Matrix Composites*. Key Eng. Mater., **108-110**, pp. 291–314, 1995.

[51] D. Mari, A. D. Krawitz, J. W. Richardson and W. Benoit. *Residual stress in WC-Co measured by neutron diffraction*. Mat. Sci. Eng. A, **209** (1-2), pp. 197–205, 1996.

[52] S. Skirl. *Mechanische Eigenschaften und Thermisches Verhalten von Al_2O_3/Al und Al_2O_3/Ni_3Al Verbundwerkstoffen mit Durchdringungsgefüge*. Fortschritt-Berichte VDI, **5** (536), pp. 1–137, 1998.

[53] S. Skirl, R. Krause, S. Wiederhorn and J. Rödel. *Processing and Mechanical Properties of Al_2O_3/Ni_3Al Composites with Interpenetrating Network Microstructure*. J. Am. Ceram. Soc., **84** (9), pp. 2034–2040, 2001.

[54] R. J. Moon, M. Tilbrook and M. Hoffman. *Al-Al_2O_3 Composites with Interpenetrating Network Structures: Composite Modulus Estimation*. J. Am. Ceram. Soc., **88** (3), pp. 666–674, 2005.

[55] J. Aboudi. *Mechanics of Composite Materials*. Elsevier Science, 1 ed., 1991.

[56] D. Gross and T. Seelig. *Bruchmechanik, mit einer Einführung in die Mikromechanik*. Springer, 3 ed., 2001.

[57] W. Voigt. *Über die Beziehung zwischen den beiden Elastizitätskonstanten isotroper Körper*. Wied. Ann., **38**, pp. 573–587, 1889.

[58] A. Reuss. *Berechnung der Fliessgrenze von Mischkristallen auf Grund der Plastizitaetsbedingung fuer Einkristalle* . Zeit. ang. Math. Mech., **9** (1), pp. 49–58, 1929.

[59] T. W. Hull, D. Clyne. *An Introduction to Composite Materials*. Cambridge University Press, Cambridge, UK, 2 ed., 1996.

[60] Z. Hashin and S. Shtrikman. *A Variational Approach to the Theory of the Elastic Behaviour of Multiphase Materials*. J. Mech. Phys. Solid, **11** (2), pp. 127–140, 1963.

[61] T. L. Anderson. *Fracture Mechanics: Fundamentals and Applications*. CRC Press, 2 ed., 1995.

[62] K. Bowman. *Mechanical Behaviour of Materials*. John Wiley & Sons, 2004.

[63] B. Lawn. *Fracture of Brittle Solids*. In E. A. Davis and I. M. Ward, eds., *Cambridge Solid State Science Series*. Cambridge University Press, 2 ed., 1993.

[64] H. Tada, P. C. Paris and G. R. Irwin. *The Stress Analysis of Cracks Handbook*. Paris Productions, Inc, St. Louis, 2 ed., 1985.

[65] A. A. Griffith. *The phenomenon of rupture and flow in solids*. Philosophical Transactions of the Royal Society, **A221**, pp. 163–98, 1920.

[66] G. R. Irwin. *Onset of Fast Crack Propagation in High Strength Steel and Aluminium Alloys*. Sagamore Research Conference Proceedings, **2**, pp. 289–305, 1956.

[67] J. Rödel. *Rißüberbrückung in keramischen Werkstoffen*. Fortschritt-Berichte VDI, **5** (331), pp. 1–127, 1993.

[68] R. Steinbrech, R. Khehans and W. Schaarwachter. *Increase Of Crack Resistance During Slow Crack-Growth In Al_2O_3 Bend Specimens*. J. Mater. Sci., **18** (1), pp. 265–270, 1983.

[69] T. Fett, D. Munz and G. Thun. *Method to Estimate Crack-Tip Toughness from Bending Tests on Prenotched Bars*. J. Am. Ceram. Soc., **83** (2), pp. 421–423, 2000.

[70] G. R. Irwin. *Handbuch der Physik*, chap. Fracture, pp. 551–594. Springer-Verlag, Berlin, 1958.

[71] A. Kounga. *Verschiebungsfelder vor und hinter der Rissspitze in verstärkten Keramiken*. Ph.D. thesis, Technische Universität Darmstadt, 2003.

[72] A. B. Kounga, T. Fett, J. Rödel and G. D. Quinn. *Crack-Tip Toughness Measurements on a Sintered Reaction-Bonded Si_3N_4*. J. Am. Ceram. Soc., **87** (8), pp. 1502–1508, 2004.

[73] E. Sommer. *Experimental determination of stress intensity factor by COD measurements*. Mech. of Fract., **7**, pp. 331–347, 1981.

[74] J. Rödel, J. F. Kelly and B. R. Lawn. *In Situ Measurements of Bridged Crack Interfaces in the Scanning Electron Microscope*. J. Am. Ceram. Soc., **73** (11), pp. 3313–3318, 1990.

[75] G. Pezzotti and O. Sbaizero. *Residual and bridging microstress fields in Al_2O_3/Al interpenetrating network composite evaluated by fluorescence spectroscopy*. Mat. Sci. Eng. A, **303**, pp. 267–272, 2001.

[76] Z. Burghard, A. Zimmermann, J. Rödel, F. Aldinger and B. R. Lawn. *Crack opening profiles of indentation cracks in normal and anomalous glasses*. Acta Mater., **52** (2), pp. 293–297, 2004.

[77] M. Hoffman, B. Fiedler, T. Emmel, H. Prielipp, N. Claussen, D. Gross and J. Rödel. *Fracture behaviour in metal fibre reinforced ceramics*. Acta Mater., **45** (9), pp. 3609–3623, 1997.

[78] O. Wiener. Abh. Math-Phys. Kl. Königl. Saechs. Ges., **32**, p. 509, 1912.

[79] D. K. Hale. *Physical-Properties of Composite-Materials*. J. Mater. Sci., **11** (11), pp. 2105–2141, 1976.

[80] E. H. Kerner. *The Elastic and Thermo-elastic Properties of Composite Media*. Proceedings of the Physical Society. Section B, **69** (8), p. 808, 1956.

[81] D. A. G. Bruggeman. *Berechnung verschiedener physikalischer Konstanten von heterogenen Substanzen. III. Die elastischen Konstanten der quasiisotropen Mischkörper aus isotropen Substanzen*. Ann. Physik, **421** (2), pp. 160–178, 1937.

[82] P. S. Turner. *Thermal-Expansion Stresses In Reinforced Plastics*. J. Res. Natl Bureau Stand., **37** (4), pp. 239–250, 1946.

[83] D. Balch, A. Mortensen, S. Suresh, Y. Shen, T. Fitzgerald and V. Michaud. *Thermal expansion of metals reinforced with ceramic particles and microcellular foams*. Metall. Mater. Trans. A, **27** (11), pp. 3700–3717, 1996.

[84] C. Hsieh and W. Tuan. *Thermal expansion behavior of a model ceramic-metal composite*. Mat. Sci. Eng. A, **460-461**, pp. 453–458, 2007.

[85] ASTME1461-01. *Standard Test Method for Thermal Diffusivity of Solids by the Flash Method*.

[86] Z. Hashin and S. Shtrikman. *A variational approach to the theory of effective magnetic permiability of multiphase materials*. J. Appl. Phys., **33** (10), pp. 3125–&, 1962.

[87] K. Lichtenecker. *Der elektrische Leitungswiederstand künstlicher und natürlicher Aggregate*. Phys. Zeit., **8,9**, pp. 169–181,193–204, 1924.

[88] K. Lichtenecker. *Über die elektrische Leitfähigkeit und andere Körpereigenschaften desselben Typus bei binären Aggregaten*. Zeit. Elektrochem. ang. phys. Chem., **40**, pp. 11–14, 1934.

[89] B. Bhusan. *Modern Tribology Handbook*. CRC Press LLC, 2001.

[90] M. A. El-Hadek and S. Kaytbay. *Al_2O_3 Particle Size Effect on Reinforced Copper Alloys: An Experimental Study*. Strain, **45** (6), pp. 506–515, 2009.

[91] L. Wang, J.-L. Shi, M.-T. Lin, H.-R. Chen and D.-S. Yan. *The thermal shock behavior of alumina-copper composite*. Mater. Res. Bull., **36** (5-6), pp. 925 – 932, 2001.

[92] S. Guicciardi, C. Melandri, F. Lucchini and G. de Portu. *On data dispersion in pin-on-disk wear tests*. Wear, **252** (11-12), pp. 1001 – 1006, 2002.

[93] F. Hosking, F. Portillo, R. Wunderlin and R. Mehrabian. *Composites of aluminium-alloys - fabrication and wear behavior*. J. Mater. Sci., **17** (2), pp. 477–498, 1982.

[94] C. S. Lee, Y. H. Kim, K. S. Han and T. Lim. *Wear behaviour of aluminium matrix composite materials*. J. Mater. Sci., **27** (3), pp. 793–800, 1992.

[95] Z. F. Zhang, L. C. Zhang and Y. W. Mai. *Wear of Ceramic Particle-Reinforced Metal-Matrix Composites .1. Wear Mechanisms*. J. Mater. Sci., **30** (8), pp. 1961–1966, 1995.

[96] B. Chen, Q. Bi, J. Yang, Y. Xia and J. Hao. *Tribological properties of Cu-based composites and in situ synthesis of TiN/TiB_2*. Mat. Sci. Eng. A, **491** (1-2), pp. 315–320, 2008.

[97] M. Sternitzke, M. Knechtel, M. Hoffman, E. Broszeit and J. Rödel. *Wear Properties of Alumina/Aluminum Composites with Interpenetrating Networks*. J. Am. Ceram. Soc., **79** (1), pp. 121–128, 1996.

[98] H. Chang, J. Binner and R. Higginson. *Dry sliding wear behaviour of Al(Mg)/Al_2O_3 interpenetrating composites produced by a pressureless infiltration technique*. Wear, **268** (1-2), pp. 166 – 171, 2010.

[99] L. Ceschini, G. S. Daehn, G. L. Garagnani and C. Martini. *Friction and wear behavior of C4 Al_2O_3/Al composites under dry sliding conditions*. Wear, **216** (2), pp. 229–238, 1998.

[100] V. Imbeni, I. Hutchings and M. Breslin. *Abrasive wear behaviour of an Al_2O_3-Al co-continuous composite*. Wear, **233-235**, pp. 462–467, 1999.

[101] A. T. Alpas and J. Zhang. *Effect Of Microstructure (Particulate Size And Volume Fraction) And Counterface Material On The Sliding Wear-Resistance Of Particulate-Reinforced Aluminum-Matrix Composites*. Metall. Mater. Trans. A, **25** (5), pp. 969–983, 1994.

[102] F. E. Kennedy, A. C. Balbahadur and D. S. Lashmore. *The friction and wear of Cu-based silicon carbide particulate metal matrix composites for brake applications*. Wear, **203-204**, pp. 715 – 721, 1997. 11th International Conference on Wear of Materials.

[103] S. J. Cho, B. J. Hockey, B. R. Lawn and S. J. Bennison. *Grain-Size and R-Curve Effects in the Abrasive Wear of Alumina*. J. Am. Ceram. Soc., **72** (7), pp. 1249–1252, 1989.

[104] M. W. Rutenberg. *Handbook of Water Soluble Gums and Resins*, chap. Starch and Its Modification, pp. 22.1 – 22.83. McGraw-Hill, 1980.

[105] G. V. Franks and Y. Gan. *Charging Behavior at the Alumina-Water Interface and Implications for Ceramic Processing*. J. Am. Ceram. Soc., **90** (11), pp. 3373–3388, 2007.

[106] S. I. Bae and S. Baik. *Determination of Critical Cencentrations of Silica and/or Calcia for Abnormal Grain Growth in Alumina*. J. Am. Ceram. Soc., **76** (4), pp. 1065–67, 1993.

[107] A. Krell and P. Blank. *The Influence of shaping method on the grain size dependence of strength in dense submicrometre alumina*. J. Eur. Ceram. Soc., **16** (11), pp. 1189–1200, 1996.

[108] E. Gregorova, Z. Zivcova and W. Pabst. *Porosity and pore space characteristics of starch-processed porous ceramics*. J. Mater. Sci., **41** (18), pp. 6119–6122, 2006.

[109] W. Pabst, E. Gregorová, J. Havrda and E. Týnová. *Gelatin casting and starch consolidation of alumina ceramics*. In *Ceramic Materials and Components for Engines*. 2001.

[110] J. S. Reed. *Principles of ceramic processing*. Wiley-Interscience, 2 ed., 1995.

[111] MATLAB. vol. version 7.5 (R2007b). Natick, Massachusetts: The Mathworks Inc., 2007, 2007.

[112] G. R. Davis and J. C. Elliot. *Artefacts in X-ray microtomography of materials*. Mater. Sci. Technol., **22**, pp. 1011–1018, 2006.

[113] V. Salit. *Some contributions to the homogenization of macroscopically isotropic composites*. Ph.D. thesis, Festkörpermechanik, Technische Universität Darmstadt, 2011.

[114] ASTME1876-01. *Standard Test Method for Dynamic Young's Modulus, Shear Modulus, and Poisson's Ratio by Impulse Excitation of Vibration*.

[115] DIN51109. *Messung der Bruchzähigkeit vom scharfen Anriss in Biegeprobe: SEPB-Methode*.

[116] O. Raddatz, G. Schneider, W. Mackens, H. Voß and N. Claussen. *Bridging stresses and R-curves in ceramic/metal composites*. J. Eur. Ceram. Soc., **20**, pp. 2261–2273, 2000.

[117] ASTM-G99-05. *Standard Test Method for Wear Testing with a Pin-on-Disk Apparatus*, 2005.

[118] A. Greer. *Partially or fully devitrified alloys for mechanical properties*. Mat. Sci. Eng. A, **304-306**, pp. 68–72, 2001.

[119] H. S. Kim. *On the rule of mixtures for the hardness of particle reinforced composites*. Mat. Sci. Eng. A, **289** (1-2), pp. 30–33, 2000.

[120] ASTM-C1161-02c. *Standard test method for flexural strength of advanced ceramics at ambient temperature*, 2008.

[121] M. M. Knechtel, N. Claussen and J. Rödel. *Reliability Of Structural Ceramics*. Philosophical Transactions Of The Royal Society Of London Series A-Mathematical Physical And Engineering Sciences, **351** (1697), pp. 469–483, 1995.

[122] F. Zok and C. L. Hom. *Large scale bridging in brittle ceramic composites*. Acta metall. mater., **38** (10), pp. 1895–1904, 1990.

[123] R. L. Lehman and M. G. McLaren. *The CRC handbook of mechanical engineering*, chap. Section 12 Materials, pp. 12–1 – 12–84. CRC Press, 2 ed., 2005.

[124] L. D. Hart, ed. *Alumina Chemicals*. The American Ceramic Society, Westerville, OH, 1990.

[125] T. Ostrowski and J. Rodel. *Evolution of mechanical properties of porous alumina during free sintering and hot pressing*. J. Am. Ceram. Soc., **82** (11), pp. 3080–3086, 1999.

[126] Q. Zhang, G. Wu, L. Jiang and B. Luan. *Thermal properties of a high volume fraction SiC particle-reinforced pure aluminum composite*. Phys. Stat. Sol. (a), **202** (6), pp. 1033–1040, 2005.

[127] A. Neubrand. *Gradientenwerkstoffe mit Durchdringsgefüge: Herstellung und Verhalten in mechanischen und thermischen Belastungsfeldern*. Habilitation, Technische Universität Darmstadt, 2002.

[128] S. Schön, H. Prielipp, R. Janssen, J. Rödel and N. Claussen. *Effect of Microstructural Scale on Thermal Shock Resistance of Aluminum-Reinforced Alumina*. J. Am. Ceram. Soc., **77** (3), pp. 701–704, 1994.

[129] C. N. Masterson, W. L. Hurley. *Chemistry: Principals and Reactions*. Thomson Learning, Inc, 2004.

[130] S. Galal-Yousef, J. Rödel, E. R. Fuller, A. Zimmermann and B. S. El-Dasher. *Microcrack Evolution in Alumina Ceramics: Experiment and Simulation*. J. Am. Ceram. Soc., **88** (10), pp. 2809–2816, 2005.

[131] R. G. Bayer. *Mechanical Wear: Fundamentals and Testing*. Marcel Dekker, Inc., 2004.

Curriculum Vitae

Personal details

Jami Winzer
Franz-Kruckenberg-Straße 38
69126 Heidelberg
Born on 30.03.1981 in Sydney, Australia
Married, two children

Education

02.1993 to 11.1998	Covenant Christian School, Belrose, Australia Higher School Certificate
03.1999 to 11.2003	University of New South Wales, Kensington, Australia Bachelor of Engineering in Process Metallurgy
04.2005 to 03.2006	RWTH Aachen University, Germany Master of Science in Physical Metallurgy,

Work Experience

11.1999 to 02.2000	Capral Aluminium, Yennora, Australia Internship in process optimisation (extrusion)
11.2000 to 02.2001	Boral Bricks, Moorebank, Australia Internship in product development
07.2001 to 12.2001	Alcoa Aluminium ARP, Yennora, Australia Internship in process optimisation (rolling)
01.2002 to 06.2002	CSIRO Minerals Division, Clayton, Australia Internship in research and development
01.2004 to 03.2005	Tomago Aluminium Casting Division, Tomago, Australia Process optimisation graduate
05.2005 to 05.2006	Aachen University, Physical Chemistry, Germany Student assistant
07.2006 to 07.2011	Technische Universität Darmstadt, Materials Science, Germany Research and teaching assistant and PhD candidate

Publications

A. McKie, J. Winzer, I. Sigalas, M. Herrmann, L. Weiler, J. Rödel and N. Can. *Mechanical properties of cBN-Al composite materials*. Ceramics International, **37** (1), pp. 1–8, 2011

J. Winzer, L. Weiler, J. Pouquet and J. Rödel. *Wear behaviour of interpenetrating alumina-copper composites*. Wear, **271** (11–12), pp. 2845–2851, 2011

Conference Presentations

J. Winzer, L. Weiler, V. Salit, Z. Poniznik, J. Dusza, M. Basista, D. Gross and J. Rödel. *Production and Young's modulus of copper-alumina interpenetrating network composites*. Materials Science and Engineering, Nürnberg, September 2008

J. Winzer, L. Weiler (Sp), V. Salit, J. Dusza, D. Gross and J. Rödel. *Mechanische Eigenschaften von Kupfer-Aluminiumoxid Verbundwerkstoffen mit interpenetrierendem Netzwerk*. 16th Symposium: Verbundwerkstoffe und Werkstoffverbunde, April 2009, Bayreuth

J. Winzer, L. Weiler, V. Salit, J. Dusza, D. Gross and J. Rödel. *Mechanical and Thermal Properties of Copper-Alumina Interpenetrating Network Composites*. Materials Science and Engineering, Darmstadt, September 2010

J. Winzer, L. Weiler and J. Rödel. *Fracture toughness and thermal expansion of alumina-copper interpenetrating composites*. 35th International conference on Advanced Ceramics and Composites, Daytona, USA, January 2011

J. Winzer, L. Weiler, V. Salit, D. Gross and J. Rödel. *Wear and thermal properties of alumina-copper interpenetrating composites*. 17th Symposium: Verbundwerkstoffe und Werkstoffverbunde, Chemnitz, April 2011

édition scientifique
VVB LAUFERSWEILER VERLAG

VVB LAUFERSWEILER VERLAG
STAUFENBERGRING 15
D-35396 GIESSEN

Tel: 0641-5599888 Fax: -5599890
redaktion@doktorverlag.de
www.doktorverlag.de

ISBN: 978-3-8359-5857-9